5-2019

Morphometric analysis and application in galaxy evolution and high-redshift surveys.

Samir Kusmic
University of Louisville

Morphometric Analysis and Application in Galaxy Evolution and High-redshift Surveys

by

Samir Kusmic

Submitted in partial fulfillment of the requirements for
Graduation *summa cum laude*
University of Louisville
May, 2019

Contents

List of Figures

List of Tables

Acknowledgments

This thesis of mine is not truly mine alone. Ever since I was in school, I have gotten support from countless people: teachers, professors, friends, family, colleagues. This whole time was built on risk on how I will develop, as well as risk on what to research. Those that helped deserve to be recognized.

The first and obvious acknowledgements are for Dr. Benne Holwerda and Dr. Joanna Bridge. Dr. Holwerda was the one who just began working in the department and saw this mild, timid, shy sophomore student come up to him and ask for a research opportunity. There was obvious risk in not knowing what will happen and if I would just give up. Yet, after the first project, we got the results for how confident and accurate `Source Extractor` is. Then, after the same sophomore, then a junior, just got rejected by ever single research internship he applied for, Dr. Holwerda still took up his offer to continue researching. Dr. Bridge was the main inspiration for the second project over scale-invariant morphological analysis. She and Dr. Holwerda helped guide me even more, letting me be more free with what I am looking for and even let me report and write up my research in an article. They both saw an undergraduate student with passion for astronomy, and they helped guide me through and through with what they know, up and even past this very moment as this thesis is written.

There are also professors who I did not research under, yet helped me through the few years. Dr. David Brown was my undergraduate advisor, and he helped answer all my questions on how I should approach my physics degree and whether what I planned was a good idea or not. Additionally, he is one of the nicest people I have met and I hope to be like him one day. Dr. Gerard Williger was my astrophysics professor, and he did the micro-management of

advising a little more thoroughly for the world of astrophysics academia. He told me what falters we have and how I should complete certain things by myself, yet had total confidence and faith in me that I will succeed after his lectures. Dr. John Kielkopf and Dr. Lutz Haberzettl, along with Dr. Williger, showed me and helped me with the world of science outreach. I may have just been introduced to this outreach, but now I feel that it is something I also enjoy and want to do. All of them helped me grow as a student to where I am now.

My colleagues were also there to help and inspire me. Nicholas Duong and Brianna Mills were fellow astrophysics students who graduated before me. Nick was probably the first friendly face in college for me, introducing and helping me through the courses and being an SPS officer. Bri was the one who let me ask and helped me to be a model astro student, and nearly everything I do now was inspired by what she did. Both of them are my friends and both of them are inspirations that helped me stay on track. There are still more, though. Brandi Tungett is a colleague whose tangy humor and honesty let me be more open. Henry Brun is a colleague who was nearly always open to socialize and talk with. My astro cohort; Rebecca Steele, Thomas Rosbottom, Dustin Morkwed, Vicki Knoer, and January Cumbea; have all shared the same passion and I will always enjoy the highs and lows of PHYS 307 and 590. Last, but not least, my final friend and my significant other during the time of this writing, Phoenix Washington, has been there for me and has believed in me, even when I had my fatalistic moments. I do not know how long we will stay together, but I do hope the best and want you to be happy, Phoenix. I wish I was as effective of an antidepressant as you are to me. All of you, I shall try to remember for my life.

Yet, even before college, I was a confused, shy, and depressed child and teenager. Mr. Perry, my theatre arts teacher, helped me break my shell and be more open to the world. Mrs. Aldridge and Mrs. Garrett taught me math and physics, respectively, and helped awaken my desire in astrophysics, even though I was more of a clown at that point. But there was even before then.

That is where my family had to step in. Torn, broken, and sulken, my parents, Zilha and Semijad Kusmic, decided to stay together and have me. I was the first, and they likely did not know what they were doing, but their unending love and belief in me has helped me mold into a good student and dedicated worker, even through their doubts. Sead Kusmic was my first brother who has been the longest friend I have ever had. We both share and thoroughly discuss our desires to each other. Finally, Edis Kusmic, you may be just a 9 year-old, yet you showed love and acceptance of me. And as far as I can see it, I agree with mama: you are turning into me. All four of you have been there and helped me through my worst times, whether advice or comfort. Thank you, and I want you all to know I love you, no matter what. And I am sorry for being the worst child.

"Arm in arm, we'll win the fight, It's always been our dream!" – Jason Paige

1 Introduction

Any and all observational astronomy outside of our Solar System is only done with light analysis, whether images or spectra, and galaxies are no exception. Although extremely distant, research into the numerous galaxies continues with great popularity. The importance in this research is that it has other consequences rather than pure astronomical wonder. Galaxy research is complimentary with cosmological research, where both look into current cosmological questions such as dark energy and dark matter distribution. As well, understanding the formation of galaxies and their evolution through time lets us see some extremes of matter interaction, primarily with gravity and its mysteries.

However, behind all that, proper image analysis of such objects is possibly the most important. It is the start of any observational research, which would help conclude hypotheses and theories formulated. For this thesis, I will present my research projects and results about morphological analyses of these galaxies, as well as how it has worked when applied. I will introduce some background information necessary to understanding where my research can head. Then I will go through the projects, where I will talk about important localized knowledge and the methodology and results. Finally, I will introduce some future work that can be done to further our analytical techniques.

1.1 Defining Galaxies and Evolution Research

Galaxies are some of the most incredible and beautiful things we can see, but we do not know really anything about them. Since the "Great Debate," no

one was capable of pursuing research into galaxy evolution until Edwin Hubble created a process of galaxy morphology. His technique, although historically significant, is impractical in further research for for understanding the evolution of galaxies over time.

To understand the field we have to understand some notable instances into my research. To begin would be to note Hubble's research. He has created two important implications in his research: the idea that galaxies would look different and therefore have different properties and likely evolutions, and the radial velocity discovery that set the basis for cosmology. At first, Hubble created a taxonomic approach to the research, where he grouped galaxies based on important features: does it have a spiral or does it look like an ellipsoid? If one of those are a yes, the galaxy is a spiral or elliptical galaxy respectively. If both are no, it is an irregular galaxy. The conditions are exclusive, so both cannot be yes. From this, Hubble assumed that elliptical galaxies would eventually evolve to spirals. Although proven false, the convention of saying early-type and late-type galaxies to refer to elliptical and spiral galaxies, respectively, stuck [Ryden and Peterson, 2011]. His other work saw breakthrough in astrophysics as he saw the relationship between the radial velocity of a galaxy and its distance. His empirical equation

$$v_r = dH_0 \tag{1}$$

is known as Hubble's Law and is the foundation of cosmology, where H_0 is Hubble's constant.

The present issue with Hubble's morphological categorization is twofold: it cannot be easily represented in mathematical evaluations to show what the galaxy is, and it is biased in how an observer would determine what classi-

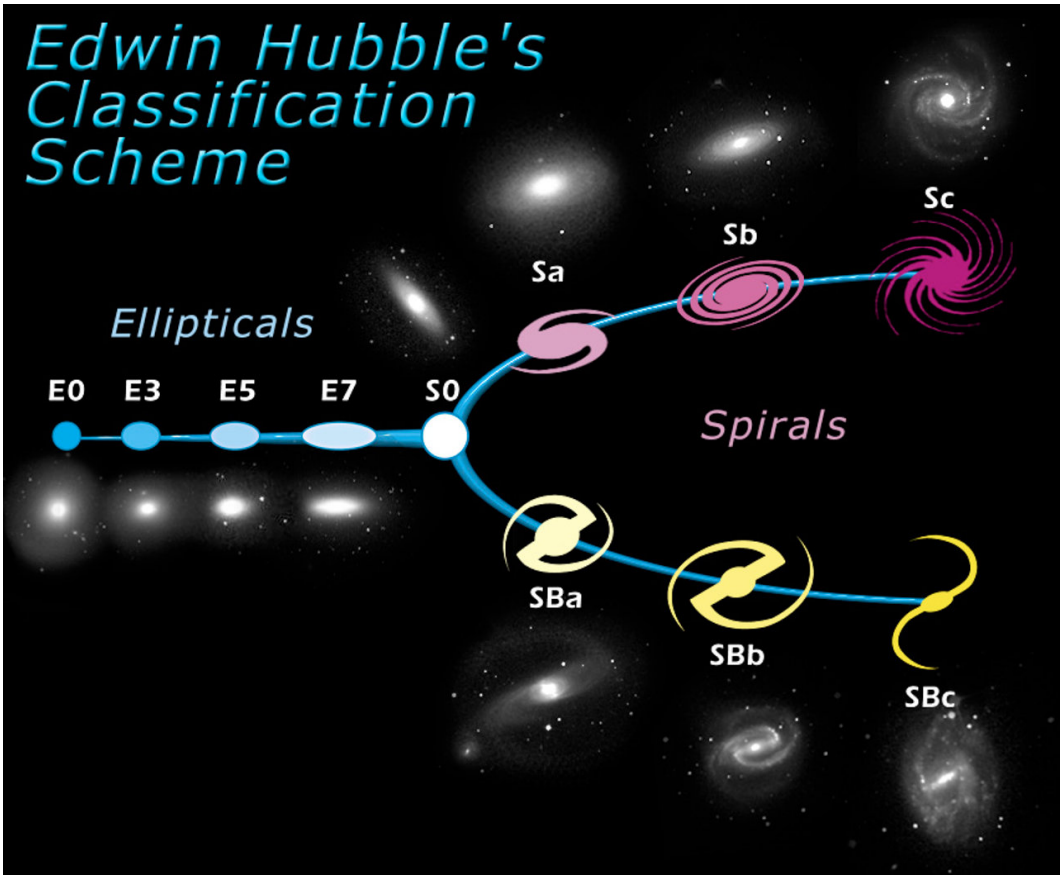

Figure 1 Hubble's famous fork diagram, showing his thought process in his evolution hypothesis. Image provided by ESA/NASA.

fies as a particular morphology. Although this makes classifications on galactic structures easy at the time, observations are difficult without a unified consensus when comparing a galaxy's morphology and its other physical properties, such as its half-light radius.

1.2 Furthering Morphology

For my case, we focus on morphology research and evolution research. Following Hubble's classifications, people followed suit with similar taxonomic approaches: such as ring and bar structure focus [Elmegreen, 1998]. This does not resolve the issue prior with Hubble types; however, some numeric parameters came out from this: inclination and ellipticity are popular examples. From this, the beginning of quantitative morphology approached with the Sèrsic profile n. For a galaxy's light profile, the intensity I from a certain radius R from the center, which has intensity I_0, has such a relationship:

$$I = I_0 e^{-k(\frac{R}{R_e})^{\frac{1}{n}}} \tag{2}$$

where R_e is the effective radius, the point in the radius where the light intensity is half of the center's and is the same as half-light radius, and n is the Sèrsic index [Sérsic, 1968]. From this, relationships are discovered by the two primary types: spirals and ellipticals. Ellipticals follow the profile when $n \approx 4$: a special profile is called the de Vaucouleur profile, while spirals follow when $n \approx 1$: which is called an exponential profile [Ryden and Peterson, 2011]. The interest would be the index, where it gives a number to a morphology. This method also brings issues, where the numbers are more dependent on the model used for measurements. However, being one of the first quantitative morphologies, it quickly became popular.

There has been a large quiet period between trying to find quantitative morphological parameters. Near the beginning of the 21st Century new parameters started to come out. These parameters are purely quantitative and are scale-invariant, where they are calculated purely on the pixel values of the object. These calculations are the Gini value, asymmetry value, smoothness, concentration, and moment of light calculations to name a few [Conselice, 2003]. This offers the opportunity of morphological calculations without the use of a model. This lets observers begin a completely neutral analysis. However, there are two issues. One issue would be that it is not an end-all-be-all form of morphology analysis, as they are primarily focused on light distribution and that can vary with filter and with redshift. They are good, however, when one uses them in their respective frame. The other, larger issue is how the parameters are drastically affected by resolution. Lower resolutions mean less pixels to work with in order to determine a parameter. This may be more reliable than human biases, but these parameters would have high uncertainty with higher redshift that may very likely be incorrect with future technology incoming. Because of their primary use in my research, I will mainly talk about the Gini value and asymmetry value. As well, these parameters are the most independent of each other, as some parameters show correlation with others when scaling resolution [Holwerda et al., 2014a].

1.3 Galaxy Evolution Research

Galaxy evolution research takes a large breadth of contents. For our case, the main focus would be with morphological and morphometric parameters that I have worked with.

One importance in understanding is the luminosity of the galaxies.

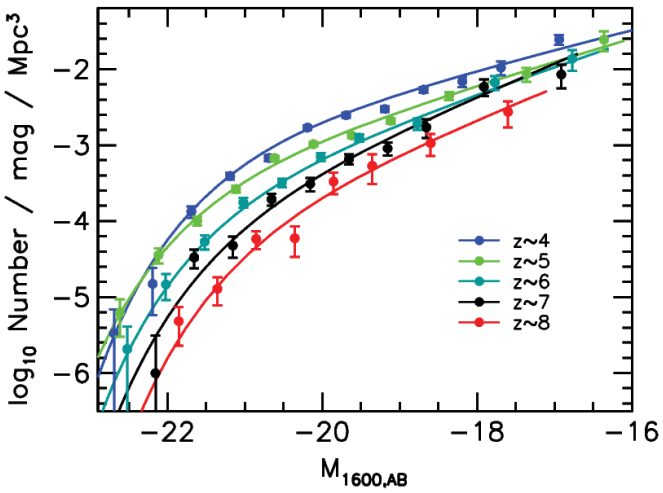

Figure 2 Luminosity function on galaxies based on redshift. Figure provided from [Bouwens et al., 2015].

An interesting observation is the population of luminous galaxies go down as redshift increases. That means galaxies have gotten brighter the farther in time we are in the Universe. This is expressed as the luminosity function (LF). This is a function of magnitude compared to number density of galaxies. Figure 2 shows the latest observational evidence for this theory. As it can be seen, the population of galaxies drop and there appears to be a magnitude cut-off per redshift and that cut-off becomes higher magnitude as redshift increases. However, this only shows statistical probability of where a galaxy should be compared to their redshift.

The other notable observation is the size differences between redshifts of galaxies. Galaxies that are more redshifted, and are therefore earlier in the time of the Universe, appear to be smaller than less redshifted galaxies. This means that the first galaxies formed were smaller, and as time went on galaxies eventually became larger. This theory has basis in Hubble's law

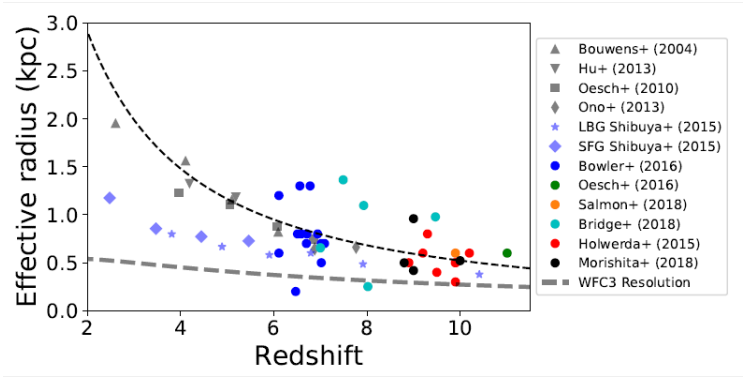

Figure 3 Redshift compared to half-light radius of galaxies between $z \sim 2 - -10$. Included are possible numerical models of this relationship. Figure provided by Dr. Benne Holwerda.

and our current understanding of the Universe through cosmology in order to properly receive a physical radius of a galaxy from angular measurements. To measure this, we typically only consider the half-light radius, equivalently called the effective radius. With approximations, we can assume baryonic mass correlates linearly with light intensity; however, it would be difficult to include dark matter halos without understanding velocity dispersion due to radii [Ryden and Peterson, 2011]. Because of that, we are limited in full description on high-redshift galaxies. However, Figure 3 gives the latest observational data into such phenomena.

1.4 Software Analysis

All of what I have talked about has an important stipulation: all contemporary research has shifted into doing computational work in some way. Because of that, our numerical analyses within our programs are important in and of themselves. That is why part of my research is looking into such software. From the scope of the research done, I talk about one particular program

called `Source Extractor` [Bertin and Arnouts, 1996].

`Source Extractor` is software that takes image data and does photometric analysis, or quantified pixel-by-pixel analysis of objects, in order to compute necessary parameters. It then generates a catalog of these objects and parameters. For my interests, it is capable of doing morphometric computations, or quantified morphology analysis, of necessary parameters such as inclination, ellipticity, position angle, and even Sèrsic index. However, there is question on the reliability of those computations, which is the motivation in my first project. That was to test the accuracy and precision of such computations, which included computed uncertainties provided by the software, and see for further application with future surveys. What we find is essentially a warning to all astronomers.

2 Source Extractor Galaxy Morphometrics

2.1 Project Introduction

A galaxy's morphology inherently holds traces of their dynamic and star-formation history. Making quantities of the morphology of galaxy or *galaxy morphometrics* has been a key sub-field for extra-galactic astronomy since the days of Edwin Hubble's tuning fork.

Morphology is also usually the first aspect considered in a new galaxy survey. With the current and coming large ground- and space-based imaging surveys (e.g. KIDS, DES, LSST, EUCLID and WFIRST), it is becoming of paramount importance to have a quick, reliable and fast tool to characterize some of the common morphometrics, because of a fear of too much data for science.

As such, one popular software astronomers turn to is `Source Extractor`. Known for being of relatively easy use and fast computations, it is the first tool used when it comes to getting data from an image.Its attractive characteristics make it seem that it is picked always, yet we do not know too thoroughly about the computations themselves.

There could be inherent inaccuracies coming from computing these parameters. For one, `Source Extractor` does not do any fitting whatsoever and heavily relies on the models pre-built within it. How truly accurate and precise are these computations? That is what we are trying to answer, by running `Source Extractor` over some fields that have already been measured using fitting, as well as getting as large of a sample size as possible.

Within this section, we test `Source Extractor` by comparing its computed catalogs to another catalog from a fitting software, `GALFIT`. Although the previous data is researched, we are approaching the survey as if it was new and untested, as future surveys will be. We will try to see how useful `Source Extractor` is with accuracy and differentiating techniques.

2.2 Survey Data

In this project, we use the CANDELS [Koekemoer et al., 2011] mosaic to be as consistent as possible with previous results we use for comparison a catalog from [van der Wel et al., 2014] with Bouwens providing a template in private communications. The images were taken by the Hubble Space Telescope (*HST*) with Wide Field Camera 3 (*WFC3*) and were of the filters F125W (J) and F160W (H) [Dressel, 2012]. The mosaics and catalogs are both freely available and pose an accessible benchmark for morphometric measurements

For the point spread function (PSF) model, we employ the circular-

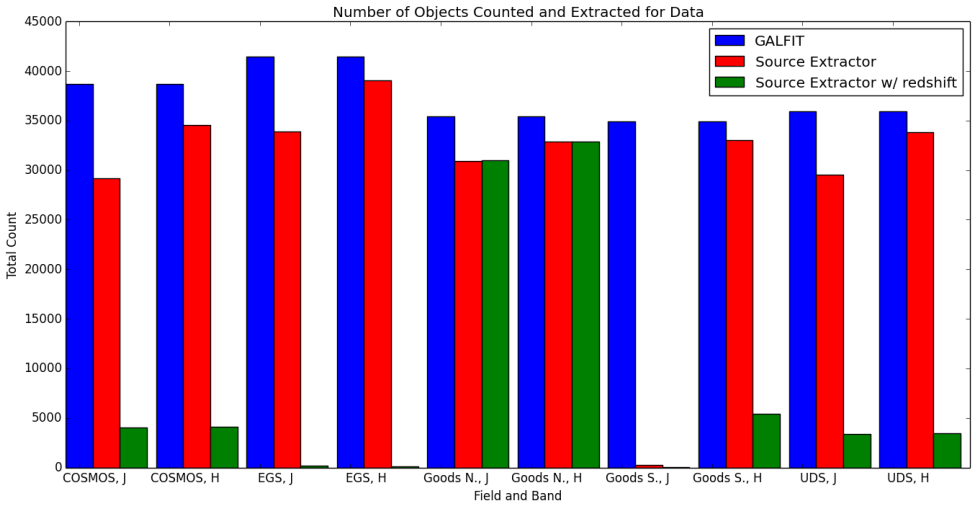

Figure 4 Total counts of the `GALFIT` catalogs and our `Source Extractor` catalogs

ized model PSF from [van der Wel et al., 2014] employed slightly different PSF models for their *GALFIT* fits but we opt for circularized model PSFs here because the orientation of the camera changes with each visit for the CANDELS mosaics. We ran `Source Extractor` on the PSF fits image to obtain a valid .cat file for PSFex to run on. Sky values were set to zero and deblending to the least aggressive level possible. The resulting F125W and F160W PSF models were then used for all subsequent `Source Extractor` runs.

The advised approach for running morphology measurements with `Source Extractor` is to first run `Source Extractor` to obtain a preliminary catalog from which one selects the stellar objects to be used by PSFex to construct a model PSF and to select those objects that are extended enough to be used in a morphological fits. In the second run, `Source Extractor` only runs on those objects in an input catalog (cross-correlation) to save time otherwise wasted on poorly resolved or uninteresting objects.

The `Source Extractor` approach is to map the data onto a model

library rather than a full fit from the user. Models are computed using a pixel grid size that depends on sampling and on the object. Image and model rasters are re-binned for very large objects Several model components currently available are included in Source Extractor:

- Background level
- Delta function (2 + 1 parameters)
- Sérsic (2 + 5 free parameters). Sérsic-like models are aliased at virtually any resolution.
- De Vaucouleurs (2 + 4 free parameters)
- Exponential (2 + 4 free parameters)

The second run uses a minimization by a LevMar implementation of the Levenberg-Marquardt algorithm [Lourakis et al., 2004], an adaptive Jacobian, with initial parameter guesses based on the "classical" `Source Extractor` measurements and bright pixels from neighbors masked automatically by `Source Extractor` in the existing code.

The `Source Extractor` implementation uses a fractional error instead of absolute ones for the bright parts of the object. The idea is that an ideal fit is unlikely given the amount of substructure typically available in galaxy images (e.g., dust lanes, star formation/HII regions, spiral structure etc etc.).

There are two key differences between the `Source Extractor` approach and existing programs such as `GALFIT` and `imfit` are: 1) the fit happens as a discrete composition of models and 2) the χ^2 is based on the fractional error, not the absolute one. This adheres to the `Source Extractor` central design philosophy tenet: speed.

Table 1 Mean ratio of $\frac{GALFIT}{SE}$ for both the spheroid model and disk model. The last column compares the two models. Threshold magnitude is applied.

H-band	Spheroid	Disk	$\frac{Disk}{Sph.}$
R_{eff}	0.5286±1.003	3.109±13.41	5.882±27.72
n	0.5993±0.7199	—	—
q	0.6±0.4595	5.203±106.7	8.672±178.0
PA	4.321±2388.0	4.672±948.4	1.081±636.4
J-band	Spheroid	Disk	$\frac{Disk}{Sph.}$
R_{eff}	1.782±1.825	3.235±13.83	1.815±7.979
n	0.9889±1.044	—	—
q	2.153±1.302	4.606±64.05	2.139±29.77
PA	4.467±3900.0	2.461±304.1	0.5509±485.8

The `Source Extractor` fits employ a couple of (tacit) assumptions or priors for the fits, e.g., only positive fluxes are allowed, but ellipticity limits for bulge components which is a little more explicit.

Instead of a double run as originally intended by the original design, we employ a single run where the positions from the van der Wel catalog are from the cross-correlated input catalog. And instead of a PSF mapping from the mosaic, we employ a PSFex model extracted from the model PSF from Bouwens et al (private communication).

2.3 Morphometric Results

The van der Wel catalog contain single Sèrsic fits to all F125W and F160W objects in the CANDELS field, we can compare the Séric index and effective radii with those obtained from the Sèrsic fits with `Source Extractor` directly. These four comparsions are made in Figure 5.

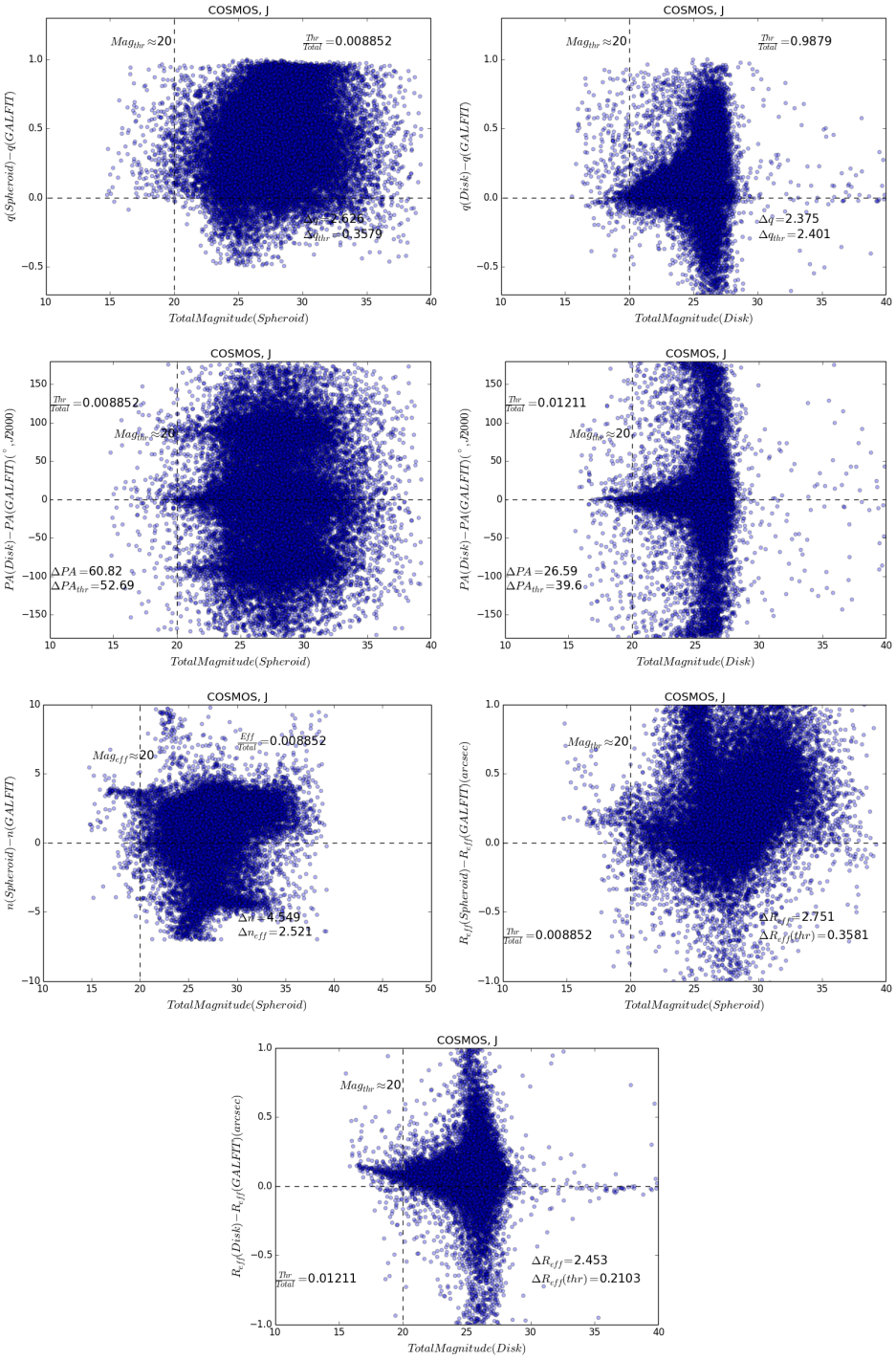

Figure 5 Differences between axis ratio, position angle, Sèrsic index, and effective radius between `GALFIT` and Source Extractor, using Total Magnitude. Spheroid model is the only one that can compare the Sèrsic index. Spheroid and disk used for effective radius comparison. COSMOS in J filter is used as an example.

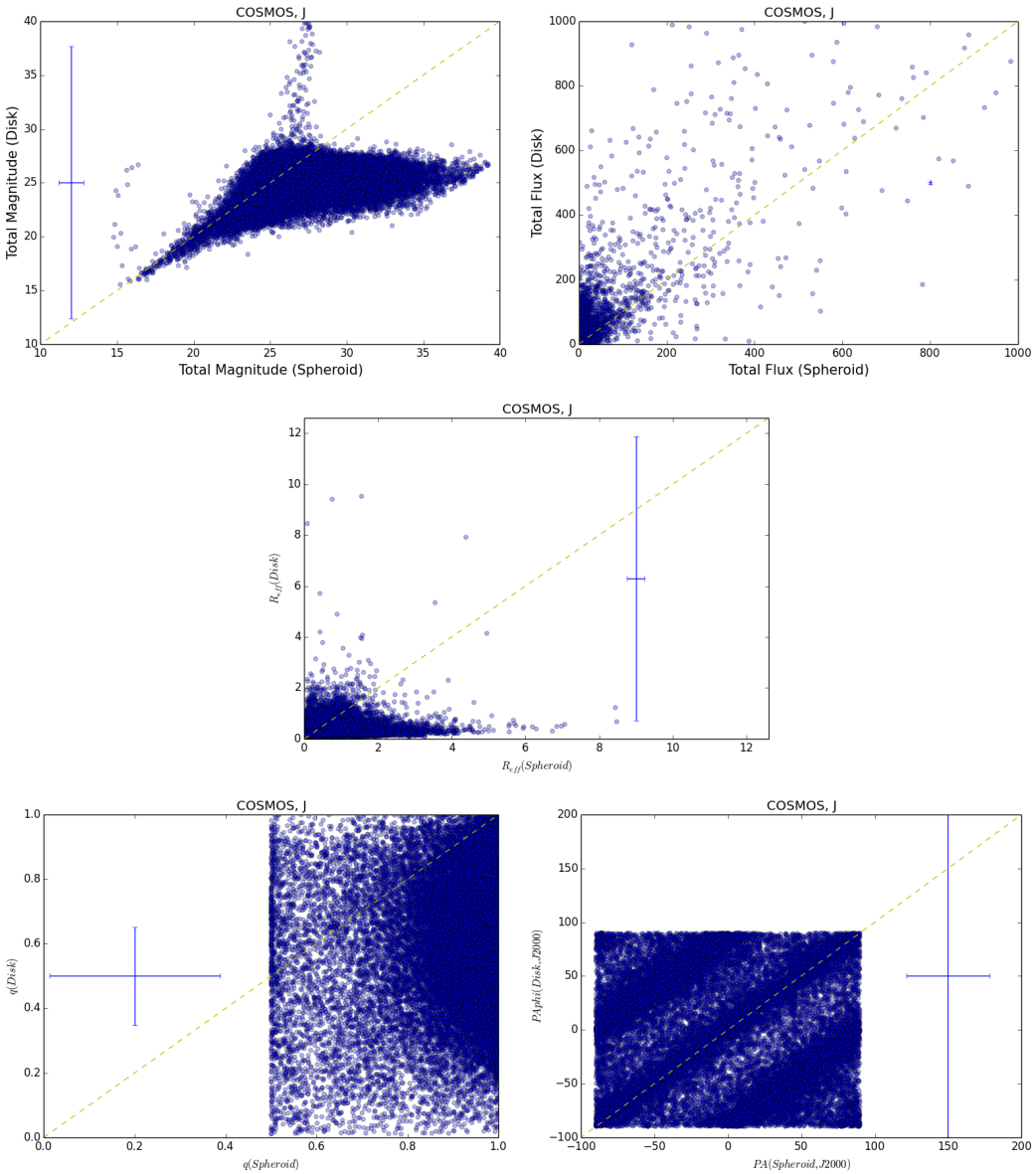

Figure 6 Comparison between the Sèrsic profile spheroid model and exponential profile disk model, comparing flux, magnitude, effective radius, axis ratio, and position angle. COSMOS in J filter is used as an example.

Table 2 Mean ratio of $\frac{GALFIT}{SE}$ for both the spheroid model and disk model. The last column compares the two models. Threshold isophotal area is applied.

H-band	Spheroid	Disk	$\frac{Disk}{Sph.}$
R_{eff}	5.746±743.6	5.124±69.2	0.8918±116.0
n	1.4±79.78	—	—
q	3.622±148.6	6.375±185.4	1.76±88.51
PA	3.874±92930.0	2.316±566.8	0.5978±14340.0

J-band	Spheroid	Disk	$\frac{Disk}{Sph.}$
R_{eff}	48.9±5381.0	4.532±62340.0	0.09268±1275.0
n	0.8911±44.78	—	—
q	3.222±111.1	5.311±177300.0	1.648±55020.0
PA	0.3704±3953.0	0.09401±219000.0	0.2538±591200.0

Related comparisons can be made for de Vaucouleur or exponential profiles by limiting the Sèrsic index in the van der Wel catalog to a value close to n=4 or n=1.

The difference between a van der Wel approach, using GALFIT, and the `Source Extractor` one may simply be a matter of information available and shot noise. Figure 5 compares the difference between the `Source Extractor` values and thee `GALFIT` ones as a function of number of object pixels.

The total amount of objects counted by `Source Extractor` is quite a bit less than that of GALFIT's, with an average $\frac{GALFIT}{SE} \approx 79.24\%$ (see **Figure 4**). Counted in total, `Source Extractor` detected 297130 sources, while there were 372882 sources in the [van der Wel et al., 2014] catalog. Goods South is catastrophically miscounted. Because of this, I recommend not using Goods South independently, because of that low count. Overall, the counts are also affected by the versions of the GOODS data of the FITS files, where

[van der Wel et al., 2014] were using version 0.5 of the files, we were using version 1.0.

We also looked into particular parameters: the effective radius and the Sèrsic index for the main comparison, as well as the axis ratio and the position angle. Seeing these properties between the `GALFIT` and Source Extractor's two models: the Sèrsic spheroid model and exponential disk model. These properties are compared between the two models and to both the total flux and total magnitude of the source. With the total flux and total magnitude, we also determined a threshold amount, where we only counted objects at or above/below it. By comparing the two models, we determined that magnitude would be the better choice, for `Source Extractor` applied a large gain to our flux count. It could be seen that in the comparison graph of flux between the two models, there is large spread with supposed little RMS error. This is likely due to this gain level, as well as general noise. The magnitude, however, shows more consistency, seeming to fit within the error bars. Using magnitude, we determined the threshold magnitude would be ≈ 20, so objects of magnitude 20 or below would be counted. With that threshold, Goods South would not count, as no object in there is at or below 20 and the catastrophic miscount discussed before. This did, however, substantially reduce the amount of objects counted in each field, varying between 0.44% and 1.21% of the total objects counted in each field per band. This, in turn, only had us count 1481 objects for the spheroid model and 1985 objects for the disk model. Compare this to 207967 sources extracted from GALFIT, these numbers are extremely low if we take into trust the accuracy proposed by [van der Wel et al., 2014].

GALFIT and `Source Extractor` do not agree with the computed values for each property. The Sèrsic index is the most varied, having an average

difference, with threshold, of $\Delta n \approx 3.16$ for all fields and bands between the spheroid model and GALFIT, showing that there is not a clear distinction of the profile of the object in question. Since this is only comparable between `GALFIT` and Source Extractor's Sèrsic spheroid model, meaning that `Source Extractor` is not fully capable to determine Sèrsic index by itself.

The effective radius is is decent. `Source Extractor` outputs the effective radius value in degrees, converted to arcseconds after computation. The mean difference came out as $\Delta R_{eff} = 2.664$" for the disk model and $\Delta R_{eff} = 1.036$" for the spheroid model. `Source Extractor` does produce the isophotal area for each object, letting us see if the elliptical area is smaller in `Source Extractor` than in GALFIT, meaning `Source Extractor` assumes the object to be smaller. However, GALFIT's isophotal area calculations are not provided. Between the spheroid model and the disk model, the disk model seems to mostly underestimated compared to the spheroid model. Keep in mind, the disk model calculated the scale length, R_h, not the effective radius. To accurately compare, we used the numeric equation $R_{eff} = 1.67835 R_h$. Still, the RMS error is greater for the disk model than the spheroid model by a substantial amount.

The axis ratio, for both models, show a bit more precision to the computation. There is still large amount of spread, though. The mean difference is $\Delta q = 2.931$ for the disk model and $\Delta q = 1.121$ for the spheroid model. This is still showing that it is quite off compared to GALFIT. Between the spheroid model and disk model is more indistinguishable. Notice that it does not go below 0.5 and above 1; however, the spread is still quite indistinguishable and forms the blob between 0.8 and 1. Although, it may say that his may say that most of these galaxies are quite circular. The error between the fields also

widely vary with either the spheroid model and disk model creating the most error in that field and band. With this discrepancy, axis ratio does not seem like it can be used with `Source Extractor` to get an accurate, precise value. However, based off of that clump, the disk model seems to be underestimated compared to the spheroid model the closer one gets to $q \leq 1$.

The position angle shows less precision. The spread is still visible, but the disk model shows the fits have more of a consistency. The mean difference was $\Delta PA = 42.05°$ for the disk model and $\Delta PA = 58.34°$ for the spheroid model. With this, disk model seems to be slightly more precise. However, looking at the comparison between the two models, there seems to be the present error of the angle either being positive or negative, and this creates the three clumping areas in the graph. Still, the disk model's large general error is still larger, as seen with its mean error bar.

For further comparison, we took the average ratio, in each filter, for each parameter, in each model: $\frac{GAL}{Sph.}$ and $\frac{GAL}{Disk}$. On top of that, we compared the two models by dividing their mean ratios: $\frac{GAL/Disk}{GAL/Sph.}$. It shows which parameter are the least useful from Source Extractor. With the effective radius, it is effectively close, being $\frac{GAL}{Sph.}_{R_{eff}} = 0.5268$ in H-band and $\frac{GAL}{Sph.}_{R_{eff}} = 1.782$ in J-band for the spheroid model, while it is $\frac{GAL}{Sph.}_{R_{eff}} = 3.109$ (H) and $\frac{GAL}{Sph.}_{R_{eff}} = 3.235$ (J) for the disk model. However, effective radius does have large error, with it being over 100% of the proposed value. The position angle has the larger multiplier of them all, being averaged at $\frac{GAL}{Sph.}_{PA} = 4.321$ (H) $\frac{GAL}{Sph.}_{PA} = 4.467$ (J) both with the spheroid model, and $\frac{GAL}{Disk}_{PA} = 4.672$ for H-band and $\frac{GAL}{Disk}_{PA} = 2.461$ for the J-band, both for the disk model. However, the errors are extreme; obviously, they are larger than than the number by almost a factor of 100000% at maximum and around a factor of 100% to 500% for the rest.

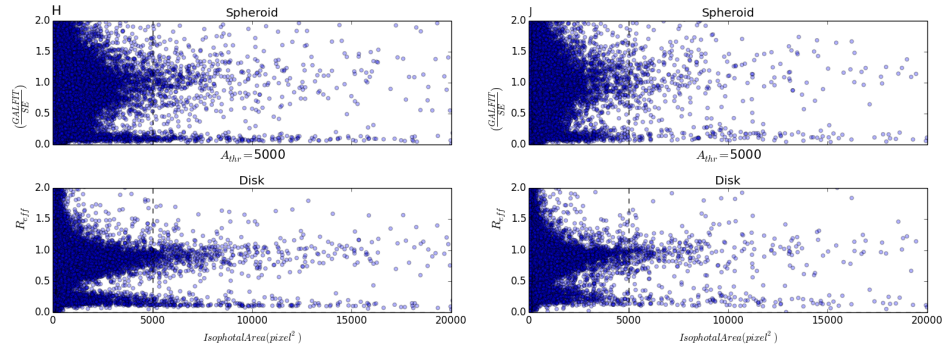

Figure 7 Comparison of Isophotal area and ratio of effective radius ($\frac{GALFIT}{SE}$) between the two models, H and J-band.

With such errors, no reliable accuracy can be assigned to position angle. The axis ratio is the smallest multiplier between the two models, being $\frac{GAL}{Sph.\,q} = 0.6(H)$ and $\frac{GAL}{Sph.\,q} = 2.153(J)$ for the spheroid model and $\frac{GAL}{Disk\,q} = 4.672(H)$ and $\frac{GAL}{Disk\,q} = 2.461(J)$ for the disk model. The disk model does, however, have extreme errors, as well. They are up to a factor of almost 2000%. The spheroid model, however, are not as extreme. They are around a factor of 83% and 60%.

However, looking at the magnitude, it would be considered biased, as it depends on the model, which utilizes the PSF that was provided. Instead, we look at an unbiased measurement provided by Source Extractor: the isophotal area. When we look at the isophotal area, we see that provided noise is noticeable if it is below the minimum of 1000 pixels^2, and for highest accuracy recommended at 5000 pixels^2. In this project, we look at the minimum isophotal threshold. Also looking at these threshold graphs, we see that there is the certain population that seem to be objects we avoid, i.e. M-dwarfs, but with the added spectroscopic redshift into the catalogs later on, the object would have to be receding and substantial enough to be counted, so they would be sorted out.

Looking at its ratios are not as accurate, however. The Sèrsic index are close between the two thresholds; it is less similar in H-band than in J-band. It makes sense, as J-band objects would appear more luminous in the data due to Malmquist bias. Axis ratio follows by, with the same trend of having more similar in J-band than in H-band. Position angle is less so, and effective radius is the least similar between the two thresholds. Both technically still have more similar objects in J-band. However, looking at the errors using isophotal area, the spread with that threshold is larger than with the magnitude threshold. Looking at the `Source Extractor` in general, it does not fit well with GALFIT's calculated parameters. One negative with the isophotal threshold is visible in Figure 7, where below the 0.5 of the effective radius ratio, that some objects that do not seem to be galaxies are getting picked up with the threshold applied. This shows that `Source Extractor` in itself cannot distinguish galaxies from other objects, and some error will pass through.

Another reason we use isophotal area threshold instead of magnitude threshold is the visible bias between the two models when it comes to determining the magnitude of an object. As seen in Figure 6, the disk model seems to cap the apparent magnitude of any measurement around 28, but the spheroid model seems to extrapolate and seemingly pick up fainter objects. Viewing this, we can say that the disk model, only picking up at a certain measurement, to be more realistic, while the spheroid model seems too optimistic in what it picks up. This does show inconsistency with magnitude, being biased based on the model used.

Although with larger error, we look forward with isophotal area threshold. We run `Source Extractor` again, this time the correlated catalog is spec-

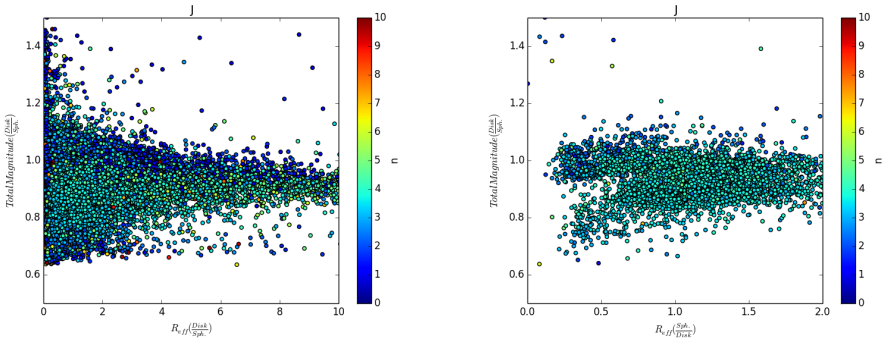

Figure 8 Ratio comparison of two `Source Extractor` models ($\frac{Disk}{Sph.}$), effective radius versus total magnitude,

troscopic redshift. The runtime this time was less, ≈ 8 hr, due to less objects specified in the spectroscopic redshift data. Looking first at the count, it is drastically lower than that between `Source Extractor` and GALFIT. There is a reason: there is not much data on the redshift of the objects we counted and extracted. However, looking at it, `Source Extractor` does seem to be able to limit the count to that of presumably any correlating catalog with its extraction run, making it efficient with the amount counted and, with proper object correlation, limit the extracted data to what we are looking at only.

Using the two models `Source Extractor` has, taking the ratios between the two models should organize the galaxies visually based on morphology, as spheroid is more attuned for ellipticals and disk model more attuned for spirals. Taking ratios of effective radius versus the total magnitude, and then colorizing the Sèrsic index, we see that there is a discernible split between the total magnitude ratio of 1. Effective radius may not be the most suitable ratio to compare; one may have better results with another ratio, say axis ratio. Also, a third parameter present should also organize it further and more clearly.

Looking at the redshift to determine evolution over time, we do seem to have similar looking results compared to other findings. Before that, biases do need to be stated. We counted more elliptical galaxies than spiral from now until $z \sim 3$. We have not gotten a large amount of spirals to say anything statistical about them. However, looking at the effective radius over time for both ellipticals and spirals, we see slight growth as time goes on, more prominent as one goes from $z \sim 3$ up until $z \sim 0.5$. From then on, it seems to start shrinking, but this is likely due to not being able to see as many things up close and getting a far fewer count rather than father away and getting a larger count. It is harder to say on spirals, as their count is far few compared to ellipticals. Still, further looking into the χ^2 of the morphologies, it seems that, in general, the fits seem to be well enough in general through redshift.

2.4 Project Discussion

Source Extractor, for all its limitations, has been the catalog software of choice for astronomical imaging surveys and the standard to which new software is compared. The introduction of morphological information (together with the option to cross-correlate using celestial rather than pixel coordinates) has once again put it at the forefront of astronomical imaging. Not bad for a 21 year old program.

The attraction of using `Source Extractor` for the next generations of imaging surveys remains its most winning aspects: stability and speed. If one can generate reasonable fits of galaxy profiles reliably and speedily, `Source Extractor` remains competitive in the coming age of imaging (e.g. LSST, EUCLID and WFIRST).

We have compared `Source Extractor` to *GALFIT* on a large public

data set here to evaluate its performance.

Source Extractor, compared to GALFIT, seems to mainly underestimate effective radius (by a large factor) and position angle, both underestimates and overestimates for the axis ratio depending on the filter used, and overestimates the Sèrsic index for the spheroid model. For using `Source Extractor` in general, we would not recommend using it by itself without following up with confirmation. One can use the mean ratios to see what one object, of magnitude 20 or below, to see what its parameters may be, then follow up with further confirmation with a different program. The primary issue would be the error, showing a large spread of possible characteristics of an object, but it can give a range.

With choosing between which model to use, the disk model seems to be the more precise choice, if not realistic, in general. After our thresholds, the disk model was the one with the least visible spread within our graphs. For certain parameters, it is harder to decide. The Sèrsic index and the axis ratio are the ones with the least spread with the isophotal area threshold, our preferred threshold.

Considering the magnitude threshold, the only remotely precise computations is axis ratio using the spheroid model. All other parameters, even the Sèrsic index, have errors above 100%. Yes, the axis ratio's errors are still large, but as a first look, which should be followed by further comparisons, it can be a viable choice. Also, considering Source Extractor's run time when the processes are run in parallel and being at maximum of 10 hours for all those parameters we had to get, it is quick and a first look that will not take too long. If using `Source Extractor` for all of them, there will be a large spread, but as a first look, especially with recently discovered objects, this can

be great to get first catalogs and first morphometric parameters.

Considering the isophotal area threshold, it is still the same as for magnitude threshold: best measurement is the axis ratio from the spheroid model. However, all the uncertainty `Source Extractor` expects is beyond that 100% presented by the magnitude threshold. Like we said before, isophotal area threshold would be our choice threshold, as it has a larger count than magnitude threshold, which is so small that it is presented data cannot be used due to biases.

2.5 Project Conclusions

In conclusion of this project, we find that `Source Extractor` can be used to quickly get first catalogs. This is mainly due to it being good in picking out objects with the correct detection threshold: 79.24% effective. Yet, it is still highly dependent on cross-correlated catalogs. This makes it useful for any pre-made detection catalog to be used for trend finding. Overall, we see `Source Extractor` as vital in understanding where objects may be in a new survey; however, we do not trust it to produce useful measurements and errors. We suggest use in order to gauge some location and amounts of galaxies, but no further.

Source Extractor mainly underestimates measurements; and the spheroid model underestimates it further, but seemingly is more realistic than the disk model. In terms of a threshold determinant, isophotal area seems most ideal as a threshold. It is large in error, but has larger count as it goes to $z \sim 3$. Although, this can be explained with our conic perception bias.

We also observe our elliptical count, with and without threshold, being too high. Likely due to Malmquist bias and cosmic variance. Considering

biases, our lacking count, although not confirm, seems to slightly compliment galaxy growth. Overall, this means that `Source Extractor` would be fine to use in terms of discovery and trend-finding; however, we suggest limiting its use further and transfer to other software.

This research has made use of the NASA/IPAC Extra-galactic Database (NED) which is operated by the Jet Propulsion Laboratory, California Institute of Technology, under contract with the National Aeronautics and Space Administration. This work is based on observations taken by the 3D-HST Treasury Program (GO 12177 and 12328) with the NASA/ESA HST, which is operated by the Association of Universities for Research in Astronomy, Inc., under NASA contract NAS5-26555. This research has made use of NASA's Astrophysics Data System. This research made use of Astropy, a community-developed core Python package for Astronomy [The Astropy Collaboration et al., 2018]. This research made use of matplotlib, a Python library for publication quality graphics [Hunter, 2007]. PyRAF is a product of the Space Telescope Science Institute, which is operated by AURA for NASA. This research made use of SciPy [Jones et al., 01].

3 Morphological Parameters of $z \sim 8$ Galaxies

3.1 Morphological Analysis Introduction

Galaxy formation and evolution can be traced through time via galaxy light profiles and morphologies. Qualitative classifications have been attempted through [Sandage, 2005], but this method is done by-eye and suffers from human biases [Elmegreen, 1998]. A definitive qualitative classification would require an infinitely well-resolved image in order to perfectly distinguish among

morphology types. Qualitative classification therefore typically falls short, especially with high-redshift galaxies, where the resolution of the images is often too low to distinguish the general galaxy profile well. This has created a push towards a quantitative classification scheme for galaxies that is as close to scale-invariant as possible. The goal is to reduce the information in an image into a few simple values without much loss of discriminatory power.

Attempts to create quantitative classifications at various resolutions have been made. One example is the Sérsic index, which traces the intensity of the light profile from the center to the fringe of a galaxy [Sérsic, 1968]. However, Sèrsic indices are only able to describe the general content of light and cannot discern internal structure on smaller scales. [Lotz et al., 2004] created a set of two parameters that focus on light distribution (Gini, concentration, and smoothness) as well as internal structure (M_{20} and asymmetry). Other studies have proposed to use concentration and smoothness measurements of galaxies in order to complement more traditional parameters [Conselice, 2003]. Unfortunately, all of these morphological parameters are optimized for $z < 3$ galaxy studies. While they constitute a promising step, little testing has been done applying these parameters to higher redshift galaxy samples.

These classifications do show large potential for high-redshift morphological classifications: they are scale invariant, they eliminate human bias, they provide a quantitative measurement that can be scaled to large samples, and they break the redshift barrier in terms of resolution and wavelength [**?**]. They can also determine if the observed morphology is due to galaxy mergers or internal star formation activity[Lotz et al., 2010, Bowler et al., 2017]. Such morphological classifications are particularly useful for lower resolution images, where hard-coded morphometric analyses such as those provided by

`Source Extractor` would be difficult to execute.

An increasing number of very bright high-redshift galaxies have been recently identified. The luminosity of these galaxies make them an excellent sample with which to study quantitative morphology at these redshifts. Seven such objects, designated as the "Super Eight" galaxies, were discovered by [Calvi et al., 2016] and [Bouwens et al., 2015], and later confirmed in Bridge et al. (*submitted*). An additional four such galaxies have been identified by [Roberts-Borsani et al., 2016a]. The Super Eight galaxies were discovered in the Brightest of Re-ionizing Galaxies (BoRG) survey [Trenti et al., 2011], while the [Roberts-Borsani et al., 2016a] sample was identified in the Cosmic Assembly Near-infrared Deep Extragalactic Legacy Survey (*CANDELS*)[Koekemoer et al., 2011, Grogin et al., 2011]. Both of these surveys used the Wide-Field Camera 3 [**?**, WFC3;]]wfc3 on the *Hubble Space Telescope* (*HST*). We use the final sample of 11 very luminous $z \sim 8$ galaxies in this work.

Confirmation of high-redshift candidate galaxies is challenging: spectroscopic confirmation is rare and observationally expensive [**?**,]Bridge et al. (*submitted*)], and [Roberts-Borsani et al., 2016a, Zitrin et al., 2015, Oesch et al., 2015, Stark et al., 2017]. Photometric redshifts require solid photometry with space-based telescopes (such as *HST* and *Spitzer*) as well as bluer band non-detections. The high-redshift frontier is now firmly at $z \sim 9-10$, which is the limit of the Lyman break technique with *HST*, with a dozen high-fidelity candidates known [Zheng et al., 2012, Coe et al., 2013, Bouwens et al., 2011b, Bouwens et al., 2011a, Bouwens et al., 2013, Ellis et al., 2013, Oesch et al., 2013, Oesch et al., 2014]. Other additional observational constraints help differentiate between high-redshift targets and contaminants such as Galactic brown dwarf stars or dusty lower-redshift dwarf galaxies [van Vledder et al., 2016, Ryan et al., 2011, Ryan et al., 2017,

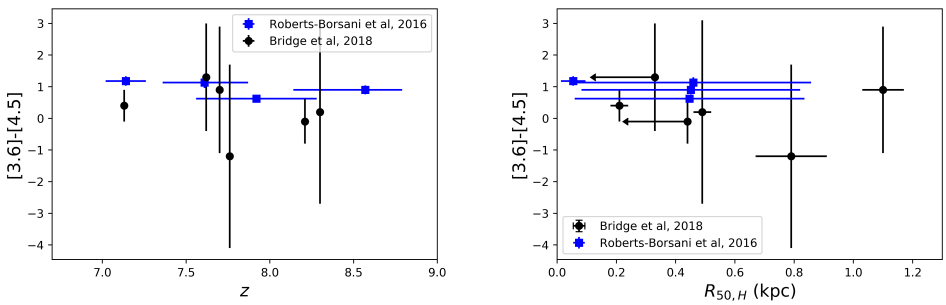

Figure 9 *Left*: IRAC color ([3.6]-[4.5]) vs. photometric redshift for the galaxies in the sample. *Right*: IRAC color vs. half-light radius in H-band. Errors represent the 1σ uncertainties; in some cases, the errors are within the marker. For both panels, the blue squares indicate the galaxies from [Roberts-Borsani et al., 2016a], while the black squares show the objects from Bridge et al. (*submitted*). Half-light radius error assumes FWHM = 2 pixels.

Holwerda et al., 2014b, Holwerda et al., 2018]. One such additional constraint is the size (effective radius) of the candidate galaxies [**?**, e.g.]]Holwerda15; this is a value of interest for galaxy formation models [Fall and Efstathiou, 1980, Mo et al., 1998], and the population's size distribution may well constrain these models from [Holwerda et al. *submitted*] and [Shibuya et al., 2015, Shibuya et al., 2018]. However, the exact size growth of galaxies still under debate [Ferguson et al., 2004, Bouwens et al., 2004, Bouwens et al., 2006, Oesch et al., 2010, Hathi et al., 2008, Ono et al., 2013, Shibuya et al., 2015].

The non-parametric galaxy morphometric parameters are therefore of interest to select high-redshift galaxies as a self-similar population, without attempting to compare the high-redshift population to the morphometric values at lower redshift, which is certain to suffer from systematics [Curtis-Lake et al., 2016].

The goal of this paper is to explore the application of two particular quantitative classifying parameters: Gini and asymmetry. We investigate how these parameters correlate with each other as well as redshift, half-light radius

in *H*-band, and the *Spitzer* IRAC color, denoted as [3.6]-[4.5]. In Section 3.2, we discuss the data acquisitions as well as our derivation of Gini and asymmetry. We explore our results in Section **??**, and discuss the implications in Section 3.4. We assume a Flat Lambda Universe with cold dark matter, where $H_0 = 70$ km s^{-1} Mpc^{-1}, $\Omega_m = 0.3$, and $\Omega_\Lambda = 0.7$.

3.2 Analysis Methodology

We obtained F125W and F160W imaging for all of the galaxies in the sample from the *Hubble* Legacy Archive[1] (HLA) and the CANDELS Multi-Cycle Treasury Program archive on MAST[2]. We extracted each object using `Source Extractor`[Bertin and Arnouts, 1996], requiring that the detection threshold for each object was greater than 1σ and that each object had a minimum of five contiguous pixels. We then determined the half-light radius and magnitude of each object using the parameters `FLUX_RADIUS` and `MAG_AUTO`, respectively. We also used the point spread function (PSF) models created for WFC3/IR for both F125W and F160W[3] in order to compare the results of the sample to measurements of the PSF only. The PSF data is in cubes, so we take the mean among all PSF images to be our model measurement for each filter.

The Gini coefficient, first used a measurement of galaxy morphology by [Lotz et al., 2004], is a measure of the concentration of the light in a galaxy. We calculated the Gini parameter by taking the image and each pixel value of the galaxy and sorting the values in increasing order, creating an array with

[1] https://hla.stsci.edu/hlaview.html

[2] https://archive.stsci.edu/prepds/candels/

[3] http://www.stsci.edu/hst/wfc3/analysis/PSF

pixel values X_i. Then, the Gini parameter can be calculated as such:

$$G = \frac{1}{|\bar{X}|n(n-1)} \sum_{i=1}^{n} (2i - n - 1)|X_i| \tag{3}$$

Here, n is the number of pixels accounted as part of the galaxy and $\bar{X}$ is the mean of the pixel values of the galaxy.

The asymmetry parameter takes into account the entire object in its image array with its pixel values X_{ij} and then we rotate the image 180°, creating a rotated image array with pixel values X_{ij}^{180}. Asymmetry is then defined as:

$$A = \sum_{i,j} \frac{|X_{ij} - X_{ij}^{180}|}{2 \sum_{i,j} |X_{ij}|} \tag{4}$$

For more details, see [Conselice, 2003].

The values of both Gini and asymmetry can range from 0 to 1. A Gini value of 0 means that the light is equally distributed among all of the pixels of the object, while a Gini value of 1 indicates that all of the light is concentrated in a single point. An asymmetry value of 0 means the galaxy is completely rotationally symmetric, while an asymmetry value of 1 means the object is completely asymmetrical in the rotational sense. [Lisker, 2008] notes that the Gini parameter value –like all morphological measures– depends on the image signal-to-noise. However, since Gini does not depend on having a precise definition of a galaxy's center, it remains one of the most robust morphometrics, preserved even in the case of gravitational lensing [Florian et al., 2015a, Florian et al., 2015b].

With the Gini, asymmetry, redshift, half-light radius, and [3.6]-[4.5] colors from [Roberts-Borsani et al., 2016b] and Bridge et al. (*submitted*) in hand, we look for correlations via both a weighted Spearman ranking and a weighted Pearson ranking. This galaxy sample consists of ten objects, as one

of the original Super Eight galaxies does not have an associated IRAC color. It should be noted that the sample is derived from two separate surveys that do have a difference in the observations technique: CANDELS was a dithered survey, while the pure parallel nature of the BoRG survey results in single, undithered pointings. However, these galaxies are identified in the same filter (F160W) with the same instrument (WFC3), and are therefore likely drawn from the same parent distribution.

In order to determine the errors for the Gini and asymmetry parameters, we need to consider two main sources of error: the shot noise, and uncertainty in the central location of the galaxy [**?**]. Because Gini is simply a measure of concentration, the exact location of the center of the galaxy does not affect the results. The error in asymmetry, however, depends on both the noise and central location error, but central location error is dominantly larger than shot noise; therefore, our approximations only considered central location error for the asymmetry.

To determine the central location error, we assumed various center locations in a range from zero to a FWHM of two pixels. These shifts in center resulted in 13 possible center locations for each object, where each image's center is shifted either vertically or horizontally. We calculated the asymmetry of each galaxy using these thirteen positions; the mean and standard deviation of these calculates give the final asymmetry value for each object.

To determine the error resulting from shot noise, we ran a simple bootstrap of 1000 instances of each pixel, drawing from a Gaussian distribution determined by the uncertainty of each pixel. The final Gini value and uncertainty for each object is then the mean and variance of the 1000 iterations.

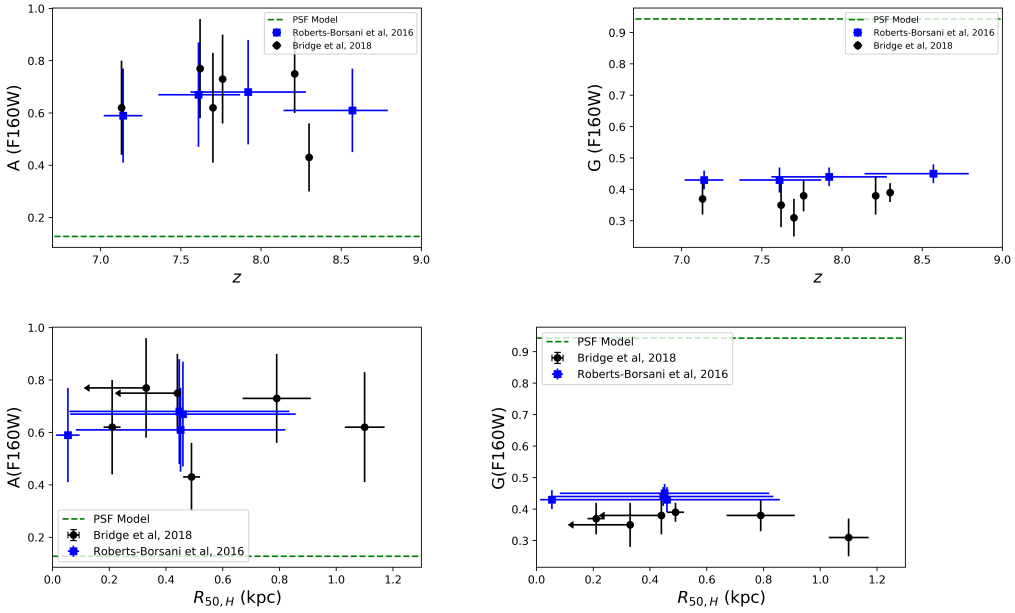

Figure 10 Gini and asymmetry values for the sample compared with redshift and half-light radius in H-band. The symbols are the same as described in Figure 9. The error bars represent 1σ uncertainties. The PSF model is shown in all panels with a green dashed line.

3.3 Morphology Results

We present the results with 1σ errors in Figures 9, 10, 11, and 12. The morphological parameters fall within a fairly limited range. The Gini values for all galaxies fall between $0.25 < G < 0.5$ in both filters.

These objects are –if indeed marginally– resolved by *HST*. Additionally, there appears to be no difference between the ranges in F160W and F125W.

In contrast, the asymmetry values span a much greater range, from $0.3 < A < 1$. Asymmetry values of 1 are practically unphysical, but the the majority of the sample ranges between $0.6 < A < 0.8$. Compared with our PSF model computations, these asymmetry values are in line with the expectations from the PSF model.

We calculate both the Spearman and Pearson ranking for the correlations between the Gini and asymmetry values and the redshift and half-light radii of the galaxies (see Figure 10). Originally, the correlations were calculated without taking the errors on the galaxy parameters into account. These correlations implied a moderate, non-linear correlation between the Gini value and asymmetry. However, disregarding the errors implies that the mean values are known infinitely well. In order to "weight" these correlations, we bootstrapped the morphological measurements 1000 times in order to generate uncertainties on the p-values of the correlations.

We find little to no correlations. The highest correlation occurs between redshift and IRAC color; however, the p value for this relationship is still $p > 0.1$, indicating low significance. This lack of correlation between the morphological parameters and *Spitzer* IRAC color or half-light radius implies independence between the morphology, size, or star formation. This independence allows using the morphologies alongside size or SFR without worrying of possible correlation affecting measurements.

3.4 Discussion of Morphological Analysis

Our analysis indicates that the morphological parameters for this sample of galaxies lie within a narrow range. This may indicate that Gini and asymmetry could be used as additional criteria for high-redshift candidacy. Due to the low-resolution of high-redshift galaxy imaging, other morphological parameters such as smoothness [Conselice, 2003] are less useful in this regard. Between the two, the better indicator of galaxy redshift is the Gini parameter, as our analysis concludes that high-redshift galaxies lie in a particularly narrow range. Given how important it is to pre-select promising candidates for *JWST* follow-

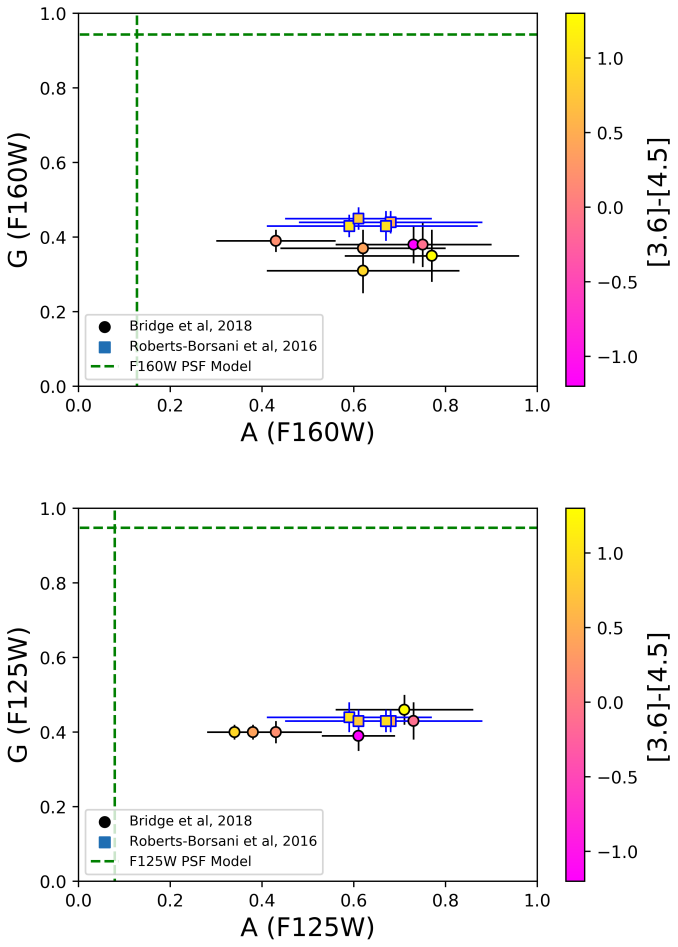

Figure 11 Comparison of Gini and asymmetry of galaxies in F160W (top) and F125W (bottom), with expected value of IRAC color as color bar. The green dotted lines show the respective PSF models.

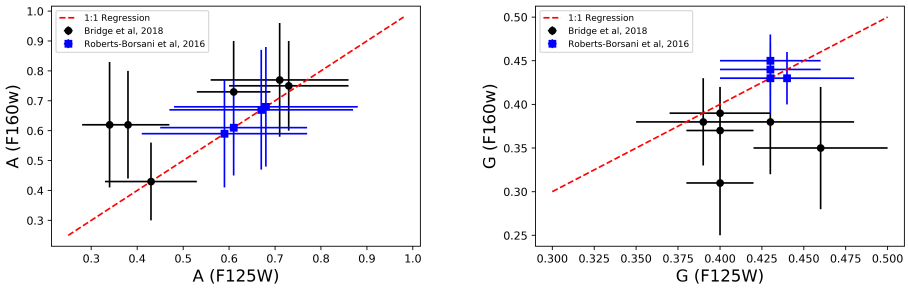

Figure 12 Comparison between the Gini and asymmetry values between the F125W and F160W images. The red dotted lines shows linear fits to the data.

Table 3.

Parameters	R(Spearman)	p(Spearman)	R(Pearson)	p(Pearson)
A and G	-0.04 ± 0.33	0.51 ± 0.29	-0.05 ± 0.33	0.49 ± 0.28
A and z	$-0.09^{+0.29}_{-0.28}$	$0.54^{+0.28}_{-0.27}$	$-0.08^{+0.29}_{-0.28}$	$0.55^{+0.28}_{-0.27}$
G and z	$0.13^{+0.26}_{-0.26}$	$0.56^{+0.27}_{-0.27}$	$0.14^{+0.23}_{-0.23}$	$0.58^{+0.26}_{-0.27}$
A and [3.6]-[4.5]	$-0.05^{+0.33}_{-0.34}$	$0.5^{+0.3}_{-0.29}$	$-0.02^{+0.36}_{-0.36}$	$0.47^{+0.3}_{-0.3}$
G and [3.6]-[4.5]	0.08 ± 0.34	0.48 ± 0.29	0.02 ± 0.34	0.49 ± 0.29
z and [3.6]-[4.5]	$-0.19^{+0.24}_{-0.25}$	$0.51^{+0.28}_{-0.28}$	$-0.1^{+0.21}_{-0.22}$	$0.6^{+0.23}_{-0.24}$
A and $R_{50,H}$	-0.02 ± 0.33	0.51 ± 0.29	-0.03 ± 0.33	0.5 ± 0.29
G and $R_{50,H}$	-0.2 ± 0.31	0.45 ± 0.3	-0.21 ± 0.31	0.45 ± 0.3

Table 4.

Parameters	R(Spearman)	p(Spearman)	R(Pearson)	p(Pearson)
A and G	-0.04 ± 0.33	0.51 ± 0.29	-0.05 ± 0.33	0.49 ± 0.28
A and z	$-0.09^{+0.25}_{-0.28}$	$0.54^{+0.27}_{-0.27}$	$-0.08^{+0.24}_{-0.28}$	$0.55^{+0.27}_{-0.27}$
G and z	$0.13^{+0.28}_{-0.26}$	$0.56^{+0.27}_{-0.27}$	$0.14^{+0.28}_{-0.23}$	$0.58^{+0.27}_{-0.27}$
A and [3.6]-[4.5]	$-0.05^{+0.32}_{-0.34}$	$0.5^{+0.28}_{-0.29}$	$-0.02^{+0.3}_{-0.36}$	$0.47^{+0.28}_{-0.3}$
G and [3.6]-[4.5]	0.08 ± 0.34	0.48 ± 0.29	0.02 ± 0.34	0.49 ± 0.29
z and [3.6]-[4.5]	$-0.19^{+0.24}_{-0.25}$	$0.51^{+0.28}_{-0.28}$	$-0.1^{+0.21}_{-0.22}$	$0.6^{+0.23}_{-0.24}$
A and $R_{50,H}$	-0.02 ± 0.33	0.51 ± 0.29	-0.03 ± 0.33	0.5 ± 0.29
G and $R_{50,H}$	-0.2 ± 0.31	0.45 ± 0.3	-0.21 ± 0.31	0.45 ± 0.3

up, this additional set of morphometric criteria may help vet ongoing target catalog generation.

There is also a considerable difference for the scale-invariant morphologies between the two filters. The data presented in the Appendix in Section 6 as well as the morphological measurements shown in Figure 12 indicates that there is little to no difference between F125W and F160W in their Gini and asymmetry measurements. A direct comparison found a mean offset in Gini and asymmetry of 0.02 and 0.07, respectively. However, as seen in Figure **??**, particular objects fall far from the regression line in both cases. Supe8-2, 3, and 4 have high Gini offset, and Super8-2 and 3 have high asymmetry offsets. This can be attributed by the different PSFs between F125W and F160W, as well as the rest-frame UV coverage being of higher energy in F125W and thus ....

Additionally, the limited morphological range could be an indicator of

galaxy formation and evolution processes at this redshift. High-redshift asymmetry could be due to an external interaction (galaxy merger) or an internal process (high star formation rate) [Bouwens et al., 2015]. [Lotz et al., 2010] simulated minor mergers between pairs of galaxies of differing mass ratios and determined the resulting scale-invariant morphologies. Comparing our results to those simulations, the galaxies in this sample show high asymmetry but moderate Gini values, similar to the simulated galaxies that are going through the beginning phases of minor mergers.

There exist some caveats to this comparison, however. For one, [Lotz et al., 2010] simulated images with far greater resolution than our sample. It is possible the simulations allowed for much more discernible internal structures than in the high-redshift sample. On top of that, the environment of the two galaxies samples are completely different, as the high-redshift galaxies exist in the era of Re-ionization, with higher neutral hydrogen levels than present, while the simulated galaxies are around $z \sim 3$. From that knowledge, the only thing that would be similar between both times may be gravitational interactions. As such, it is high possibility from our results that $z \sim 8$ is dominated by mergers.

[Curtis-Lake et al., 2016] distinguish between "smooth" and "disturbed" galaxies using asymmetry, calibrating their measurements using a suite of simulated images with Sérsic profiles. They find no strong evolution in the fraction of disturbed galaxies from $z \sim 6$ to $z \sim 4$ and that the main driver of greater asymmetry is offset star-formation clumps in the galaxies. Directly comparing our asymmetry values to their artificial catalog, with a caution against comparing across data-sets and analysis techniques, shows that all our Super Eights are in the "disturbed" range of the [Curtis-Lake et al., 2016] simulated

galaxies. For comparison, so is the F160W PSF image (green dashed line in Figure 11).

The exact nature of high-redshift morphology remains debated. [Bowler et al., 2018] discuss a sample of $z \sim 7$ bright galaxies observed with *HST* and find that a substantial number have either star-forming clumps or close companions. They argue that the clumps/close companions are indeed at the same redshift and discuss evidence for clumpy disks [**?**, see]for discussions on clumpy galaxies at other redshifts]Wuyts12, Jiang13, Kartaltepe14, Goa15. Given that these are rest-frame ultraviolet images, both clump and close (merging) companions remain equally good explanations for their bright morphologies, as long as accidental superposition can be ruled out.

3.5 Morphological Analysis Conclusion

We have presented new results on scale-invariant morphological measurements of high-redshift galaxies. The Gini values of these galaxies span a limited range between $0.18 \leq G \leq 0.3$, while the range in asymmetry values is large, with values in the range $0.3 \leq A \leq 1$. Since the redshifts and magnitudes of the [Roberts-Borsani et al., 2016a] and Bridge et al. (*submitted*) are similar, we can be fairly certain they are drawn from the same galaxy population.

The fact that there are limited correlations between the morphological parameters and IRAC color leads to a more interesting insight. Considering the fact that star formation was likely occurring rapidly during Re-ionization and likely due to mergers, Gini values stay within a small range nonetheless. As seen between the morphological parameters, both IRAC color and half-light radius are not correlated, with low rankings and low confidence in the measurements. This points to these parameters being mostly independent

of the other selection criteria considered to confirm high-redshift candidate galaxies (*Spitzer* color and effective radius).

This allows for further application of morphometrics in terms of high-redshift catalog vetting. Further testing using, possibly using simulation, is needed to determine this; however, our sample of confirmed high-redshift galaxies seem to indicate that certain morphometric values may help discriminate between high- and low-redshift galaxy populations.

4 Application into *James Webb* Observations Using JAGUAR

4.1 Introduction to Application

My previous research shows that scale-invariant morphologies have a possible use in high-redshift observation, where it can be used to vet candidates and/or further our understanding of the hypotheses and theories of the population during Re-ionization. Established in the prior work, we suspect that star formation is the dominant determinant in the morphology in Re-ionizing galaxies, using implications from our results compared to [Lotz et al., 2010] and discussed in [Bouwens et al., 2015]. Although not probing into the true quantity describing the formation rate such as intensity or magnitude, this distribution could be used to help determine these galaxies as high redhsift. As such, candidacy by Gini and asymmetry seem like an obvious choice in order to further determine if an object truly is high-redshift.

However, this all follows upon one single experiment done on a small sample ($n = 10$). How would this result in other observations, instruments, and telescopes? What implications does it have to our galaxy models and theories? Can something empirical be created with pixel distribution? These

large, overarching questions need to be answered in order to.

Direct comparison with more observations is difficult, as all possible archival data is used for high-redshift. Additionally, no other instrument has been used for such a survey at this time. As such, in order to test and attempt to answer the questions I posed, we have to look at a mock catalog called the JADES Extragalactic Ultra-deep Artificial Realization (JAGUAR): images and data created from a self-created, analytical model in order to predict what and how often certain galaxies will be observed with *JWST*, especially with upcoming JADES (*JWST* Advanced Deep Extragalactic Survey) [Williams et al., 2018]. Their model creates a population distribution for both quiescent and star-forming galaxies, creating functions with ranges from $0.2 \leq z \leq 4$ and $4 \leq z \leq 15$. Population and light distribution would follow a normal for each galaxy in this mock catalog.

With JAGUAR, this final analysis will use all algorithms and equations from the scale-invariant morphology measurements and apply it to the mock catalog. There are not filter transformations between *HST* and *JWST* at this time; however, we will have to use the two closest filters to F125W and F160W on WFC3 provided by NIRCam: F115W and F200W [4]. With the images provided, we will do the analysis and look at relationships of the objects and the data, and we will test to see if any correlation exists. One assumption was made: JAGUAR has different models for quiescent and star-forming galaxies, and se suspect the galaxies during Re-ionization to be primarily, if not all, star-forming. We only considered the star-forming catalog and picked out the galaxies where $z \sim 8$. Our standard cosmology is the same: a ΛCDM model where $h = 0.7H$, $\Omega_m = 0.3$, and $\Omega_\Lambda = 0.7$.

[4] https://jwst-docs.stsci.edu/display/JTI/Near+Infrared+Camera

4.2 JAGUAR Analysis Methods

Much of the methodology is the same as the section on high-redshift scale-invariant morphology analysis. The only difference is our inference into what sources could be high-redshift and ultra-luminous. For JAGUAR, two FITS table was created that refers to each object as either quiescent or star-forming. Our base assumption is that $z \sim 8$ ultra-luminous galaxies are star-forming; therefore, we picked out galaxies from the star-forming catalog whose redshift was in the range $7.5 < z < 8.5$ for both filters. Our created catalog had redshift, effective circular radius, and UV magnitude.

After creating a catalog of our redshift range, we then ran `Source Extractor` on our two images. This created two separate sample sizes for each filter: $n_{F115W} = 9$ and $n_{F200W} = 234$. We looked into the photometry of our model objects, with only using MAG_AUTO. In doing so, we also create our segmentation map for each object; that way, we isolate the pixels of each object and put them in cutouts without background interference. The segmentation map was used for the same reason as before. With the cutouts, we use the same definitions for Gini G and asymmetry A for our pixel values X_{ij}, provided as a reminder:

$$G = \frac{1}{|\bar{X}|n(n-1)} \sum_{i=1}^{n} (2(i) - n - 1)|X_i| \tag{5}$$

$$A = \sum_{i,j} \frac{|X_{ij} - X_{ij}^{180}|}{2\sum_{i,j} |X_{ij}|} \tag{6}$$

With our morphological results alongside our redshift and effective radius (which is similar to half-light radius, from [Williams et al., 2018]. Thus, both are denoted the same: R_{50}). With it, we did the Spearman and Pearson rankings for both the F115W sample and F200W sample, with the latter likely presenting our lower error threshold. They are to test whether a correlation

exists and whether it is linear, respectively. As a reminder, these are models based off of our theories, so these results will not necessarily reflect the physical Universe, but used to compare concretely our two morphological results between the two projects.

4.3 JAGUAR Results

Our results are presented with 1σ errors. Additionally, with our large sample size in F200W, the graphs will only present the F115W sample; however, F200W ranking tests will be provided. The tables have tested, with weights, any correlation between parameters in both F115W (Table 5) and F200W (Table 6).

The range of the morphologies do not span similarly to the observed *HST* sample. The Gini values appear to show that the models are more concentrated, where $0.7 < G < 0.85$ gives that quantitative description. At this wavelength, this may be due to poor performance of HST (effective diameter of 2.4 meters) and diffraction limited performance of JWST. The more juxtaposed result comes from the asymmetry, as $A \sim 0.8$ for the F115W objects and $0.7 < A < 0.8$ for F200W objects.

Comparisons to the redshift and effective radius do not contrast as much. Similar results were produced compared to the *HST* observations. Further comparisons, however, can be drawn be the actual rankings.

Especially with the larger sample size within F200W, we are more certain that no correlations exist. All possible ranges for the rankings have a possibility of a ranking of 0 for each pair with lower p-values that before. However, our p-values are still large and they still limit on our conclusion whether or not we can even say that there is no correlation.

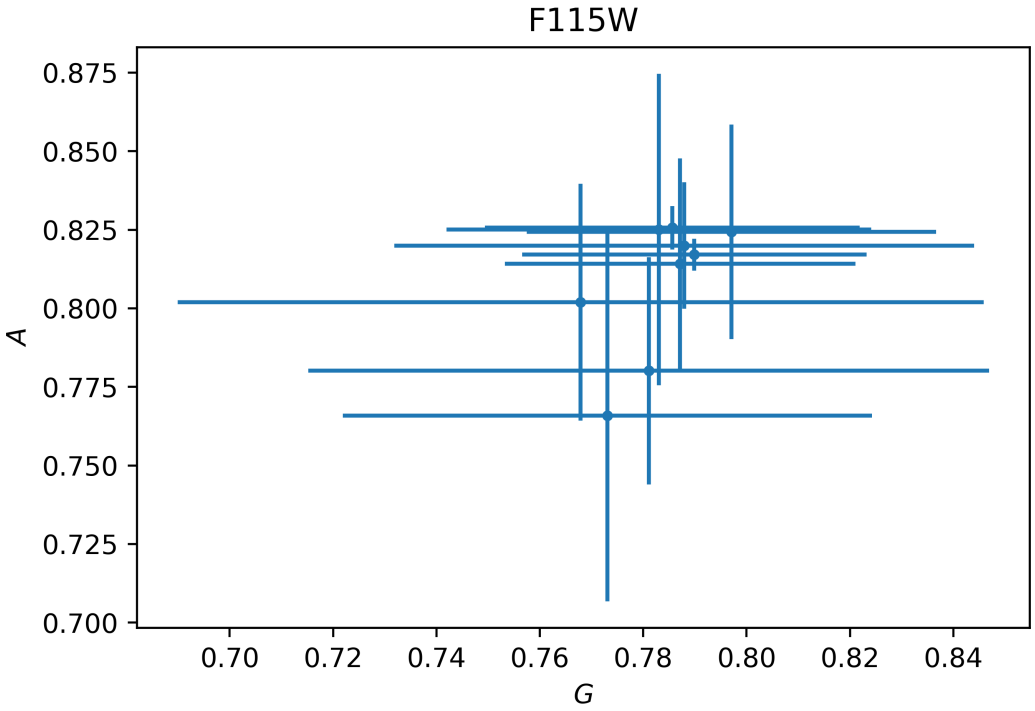

Figure 13 Gini and asymmetry measurements of the F115W sample, with 1σ errors.

Table 5.

Parameters	R(Spearman)	p(Spearman)	R(Pearson)	p(Pearson)
A and G	0.01 ± 0.35	0.52 ± 0.3	0.01 ± 0.34	0.51 ± 0.28
A and z	0.0 ± 0.38	0.48 ± 0.3	0.0 ± 0.37	0.48 ± 0.29
G and z	-0.04 ± 0.35	0.5 ± 0.29	-0.05 ± 0.35	0.49 ± 0.28
A and R_{50}	0.01 ± 0.36	0.5 ± 0.29	0.01 ± 0.36	0.5 ± 0.29
G and R_{50}	-0.01 ± 0.35	0.51 ± 0.3	0.0 ± 0.37	0.49 ± 0.29

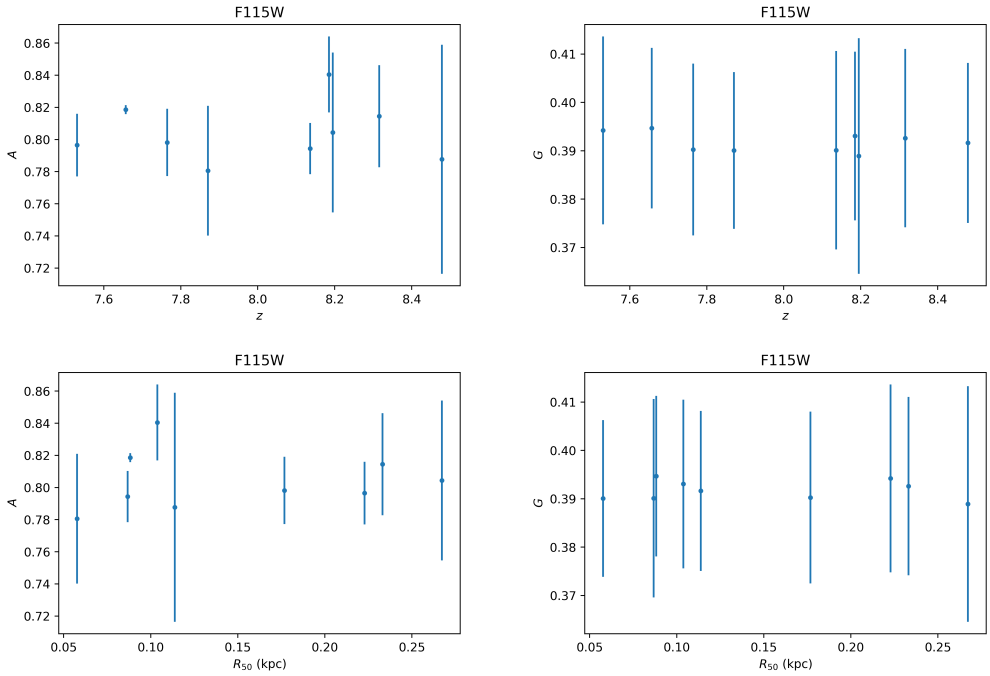

Figure 14 Comparing modelled redshifts with asymmetry(top left) and Gini (top right), as well as comparing moddelled effective radius with asymmetry (bottom left) and Gini (bottom right).

Table 6.

Parameters	R(Spearman)	p(Spearman)	R(Pearson)	p(Pearson)
A and G	0.02 ± 0.06	0.51 ± 0.29	0.01 ± 0.07	0.49 ± 0.3
A and z	0.0 ± 0.06	0.52 ± 0.3	0.0 ± 0.06	0.52 ± 0.3
G and z	-0.0 ± 0.06	0.49 ± 0.28	-0.0 ± 0.06	0.53 ± 0.27
A and R_{50}	0.0 ± 0.06	0.51 ± 0.29	0.01 ± 0.07	0.51 ± 0.29
G and R_{50}	0.01 ± 0.06	0.51 ± 0.29	0.01 ± 0.06	0.54 ± 0.27

4.4 JAGUAR Discussion

Much of this discussion follows up on the research presented in the last section, Section 3 and its discussion in 3.4. JAGUAR brings a gauge to our results from the BoRG and CANDELS surveys, since these galaxies are built to have a specific light distribution, masses, and star formation rates (SFR). Also discussed in [Williams et al., 2018] is the probability that certain masses and SFRs based on redshift. As such, our observational results can have some bearing on the validity of the approach for these mock catalogs. This allows insight on possibility of physical appearance and future implications for such morphological measurements.

The ranges in which the morphological parameters present the first contrast. The Ginis in our models are more concentrated than what was observed, yet the asymmetries are far more concentrated around 0.8, while observations are more scattered. The models' light distributions are based off of a Gaussian PSF, with usually high inclinations or eccentricity. From this, we know that an uneven distribution seems to persist in our observations, with a range of eccentricities for each galaxy.

However, the Gini-asymmetry pairs within the galaxy models' measurements from JAGUAR still do not lie within the ranges given for mergers in [Lotz et al., 2010]. Considering that these galaxies are classified as star-forming, we predict that these galaxies are dominated by their high SFRs. The placement within the SFR parameter space are not completely similar to the Lotz et al (low redshift) model, as it could be located within different locations, based on the larger asymmetry range of the observation. Additionally, SFR might have indications through Gini [Bouwens et al., 2015]. Such an indicator might show that SFR is lower in observations than in model.

Candidacy vetting was another big issue presented. Essentially, although our values do not lie within the JAGUAR mock galaxy models' ranges, they are quite close, with Gini being only 0.1 different between the ranges maximums. Our previous proposal put much emphasis in Gini as a good indicator in F125W and F160W of whether the galaxy could be $z \sim 8$, where asymmetry can be used to vet out stellar interlopers. Both observation and model have clumped Gini values, yet it is more clumped within the model. This may be a conflict with theory and the physical world, yet why does it clump at 0.4 for the models, and our observations are more diffused? Between the expected instruments, both have roughly the same effective resolution [5], and redder filters have more diffuse PSF functions [Dressel, 2012].

One final point presented that was not able to be tested prior is whether a Gini or asymmetry function can be made based off of a galaxies physical parameters. With the larger sample size presented by the F200W sample, we cannot fully conclude it. Although our values lie practically with no correlations, our high p-values hinder our confidence in our results. Initial findings with unweighted rankings proved to say that what this leads to now is a possible null result, however. All four weighted rankings show zero correlation. In a more empirical look, repetition in results may hold true; however, reducing errors would also be necessary to say for certainty.

5 Future Research and Studies

From what one can tell, I have done much work when it comes to how a galaxy can be analyzed via morphology and morphometrics. It was done using

[5] https://jwst-docs.stsci.edu/display/JTI/Near+Infrared+Camera

relatively new, untested Gini and asymmetry, which are even more new on the application of high-redshift galaxies. To be more thorough with these results, the sample size would have to increase. This means more high-redshift, ultra-luminous galaxies need to be confirmed to be tested on. This would be more doable when *Spitzer* continues operation, since its photometric measurements help us confirm high-redshift candidates to a 3σ certainty and possibly higher.

Light distribution and morphometrics are important in understanding properties of a galaxy. These properties tell us what is going on and make us estimate on what is happening or how it got there. For the analyses that I did, I would want to expand to more sub-discipline areas other than creating certainty with a larger sample test. One interest in this research is to look towards high-energy astrophysics in order to understand the light distributions there. The general assumption with high-energy is that an extreme, relativistic event is happening, such as a super-massive black hole or a neutron star as examples. Applying morphometric analysis in gamma-ray and X-ray bandwidths can help test that.

As such, for my personal future, my ultimate goal would be pursuit into astronomy and astrophysics; I want to do research in it. So far, my interests are with galaxies and their evolution, but there also exists an similarly strong interest in cosmology alongside interests in all other sub-disciplines. However, the impact from this research will be longstanding with me; I cannot overlook the practicality of scale-invariant morphologies with such surveys. However, my insight would be to wait for *JWST* to finally launch. That way, we can truly test between observations, as well as use the practically lower errors that the model measurements indicate for higher accuracy.

6 Appendix

6.1 Part A: `Source Extractor` and `GALFIT` Comparisons

Part A: The graphs below, up until *Part B*, are all scatter and line graphs representing the data received from the research over `Source Extractor` and its accuracy and precision. Each graph is split between the two filters: J, or F125W and H, or F160W. This is further split into the five fields: COSMOS, EGS, UDS, GOODS-N, and GOODS-S. The graphs show the relationships between two of the following parameters: position angle (PA), Sèrsic index (n), effective radius (R_{eff}), total flux, total magnitude, axis ratio (q), and redshift (z). An additional difference comes from `Source Extractor` and its two galaxy built-in models: the disk and exponential model. The multiple red dots with error lines are average y-values within their certain x-values. The single error line is the average error of every point in their respective graphs. Much of the graphs look at the parameter value and the difference value of parameters in both models. Some graphs contain a $1:1$ regression line, presented in yellow. **Reminder:** `Source Extractor` measurements were performed by us and the `GALFIT` measurements were done by [van der Wel et al., 2014].

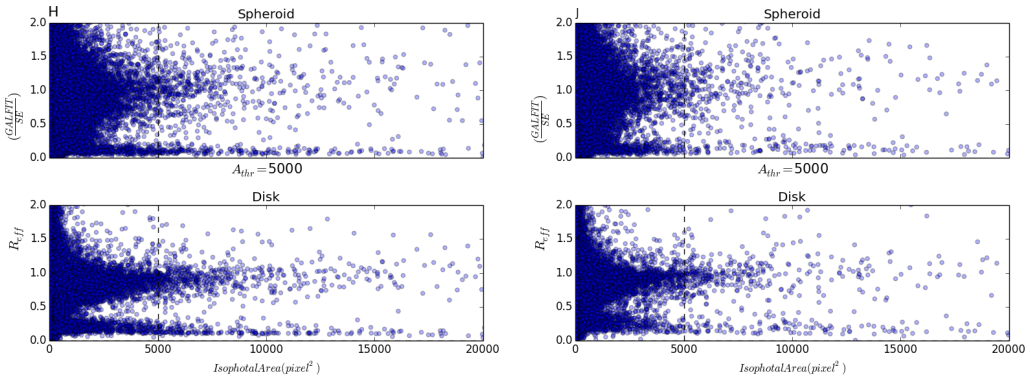

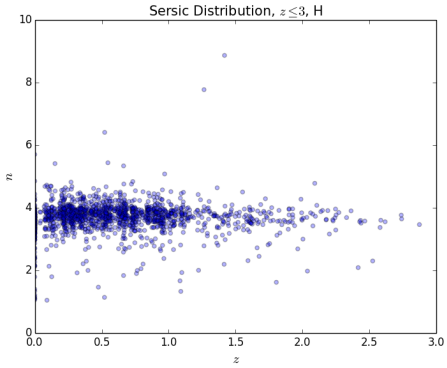
Sersic Distribution, $z \leq 3$, H
n
z

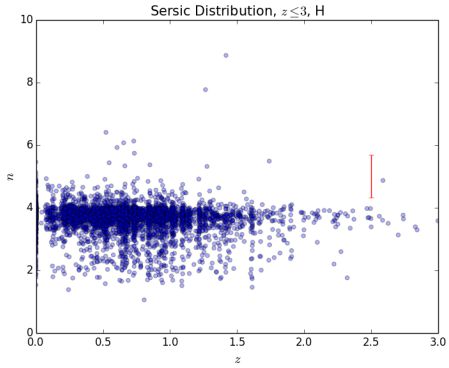
Sersic Distribution, $z \leq 3$, H
n
z

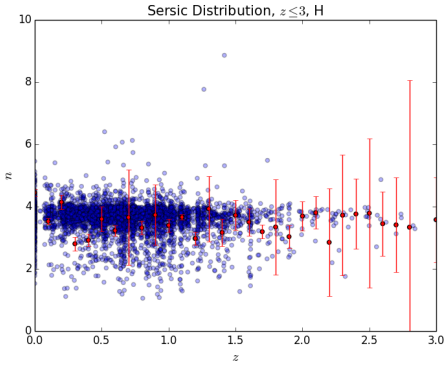
Sersic Distribution, $z \leq 3$, H
n
z

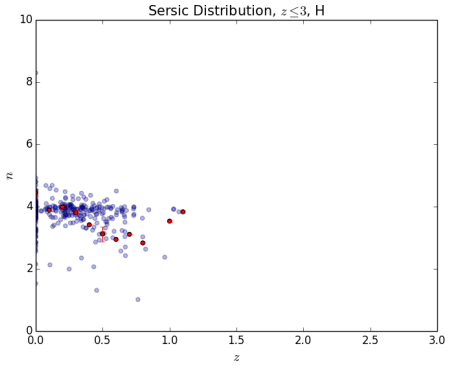
Sersic Distribution, $z \leq 3$, H
n
z

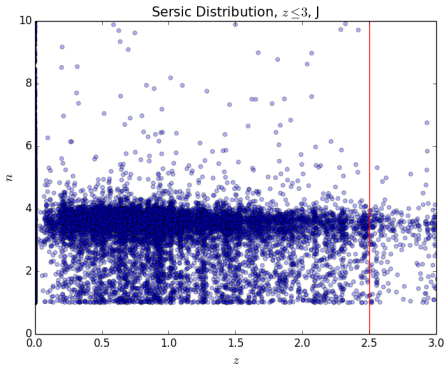
Sersic Distribution, $z \leq 3$, J
n
z

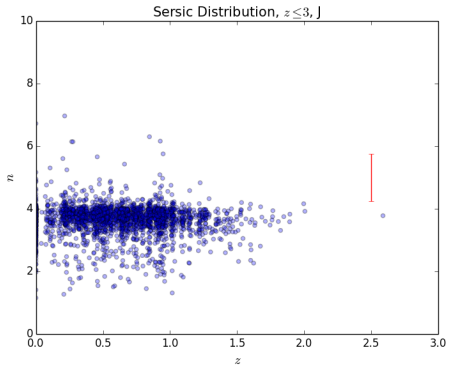
Sersic Distribution, $z \leq 3$, J
n
z

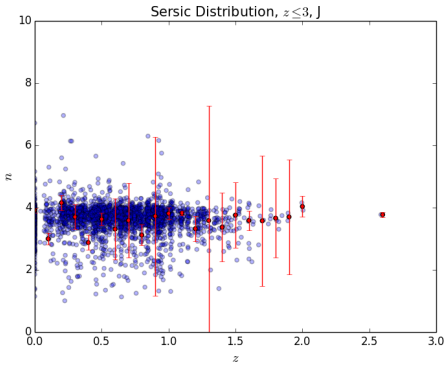
Sersic Distribution, $z \leq 3$, J
n
z

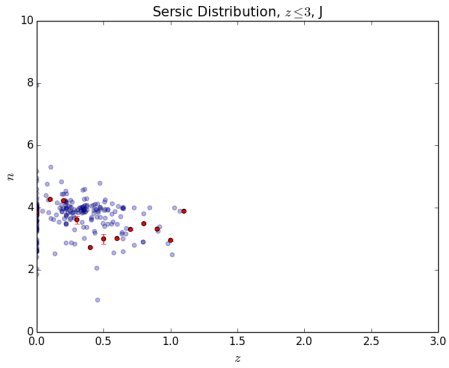
Sersic Distribution, $z \leq 3$, J
n
z

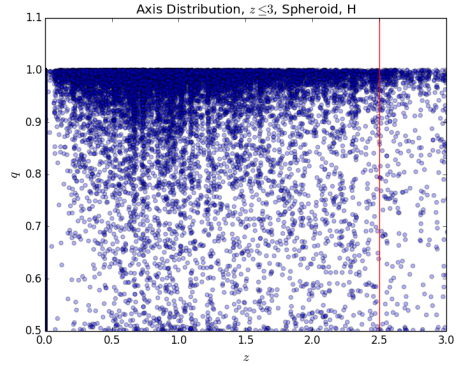
Axis Distribution, $z \leq 3$, Spheroid, H
q
z

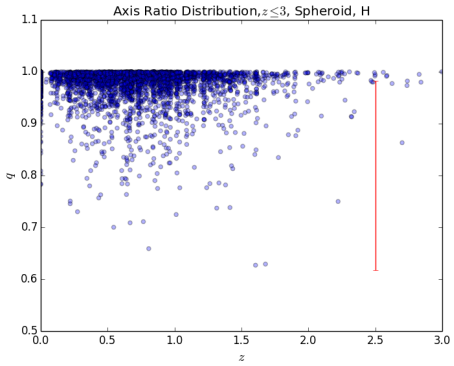
Axis Ratio Distribution, $z \leq 3$, Spheroid, H
q
z

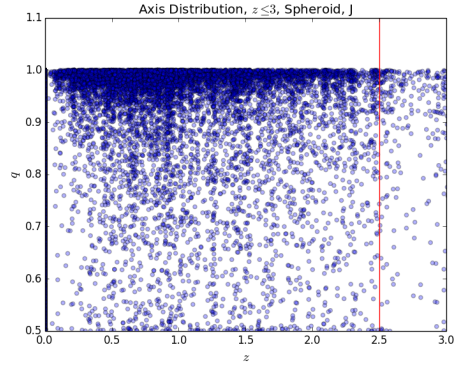
Axis Distribution, $z \leq 3$, Spheroid, J
q
z

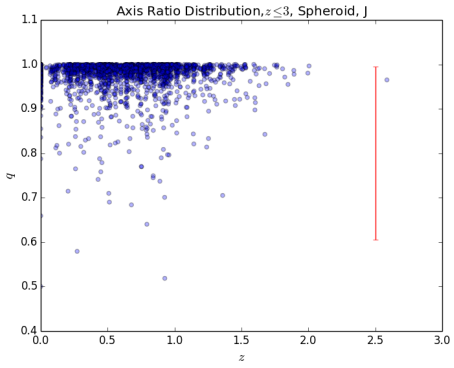
Axis Ratio Distribution, $z \leq 3$, Spheroid, J
q
z

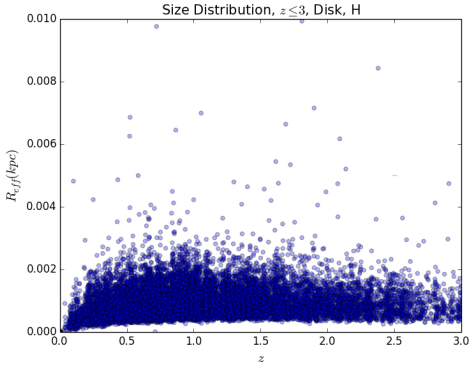
Size Distribution, $z \leq 3$, Disk, H
$R_{eff}(kpc)$
z

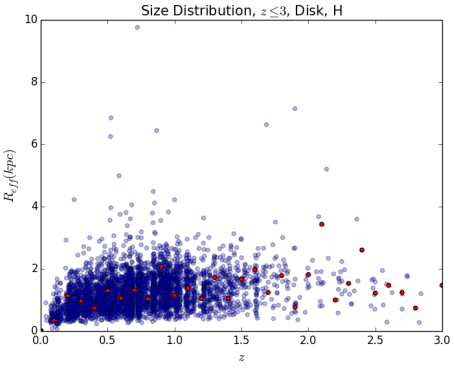
Size Distribution, $z \leq 3$, Disk, H
$R_{eff}(kpc)$
z

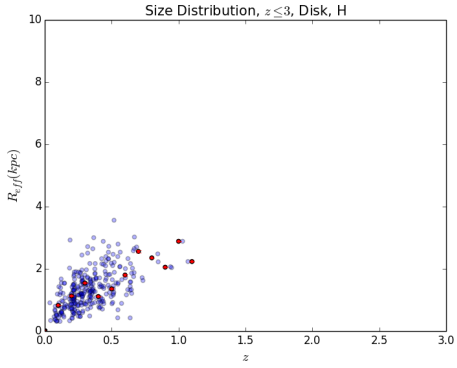
Size Distribution, $z \leq 3$, Disk, H
$R_{eff}(kpc)$
z

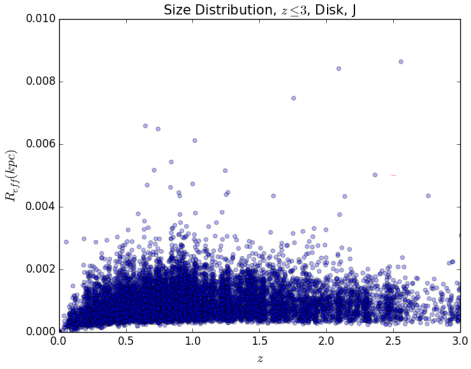
Size Distribution, $z \leq 3$, Disk, J
$R_{eff}(kpc)$
z

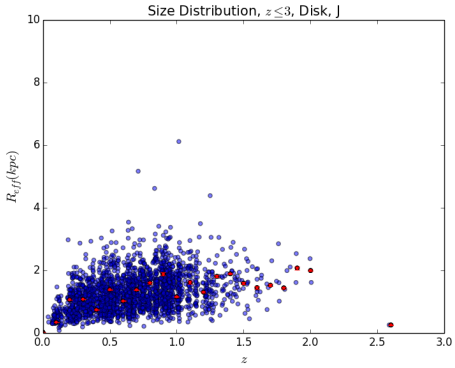
Size Distribution, $z \leq 3$, Disk, J
$R_{eff}(kpc)$
z

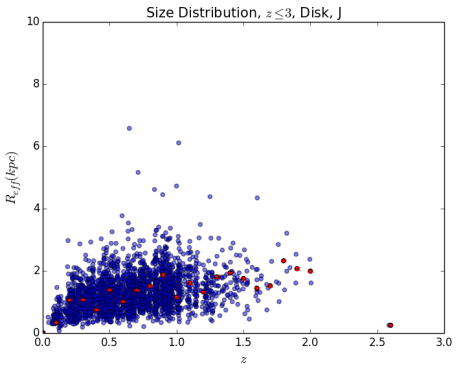
Size Distribution, $z \leq 3$, Disk, J
$R_{eff}(kpc)$
z

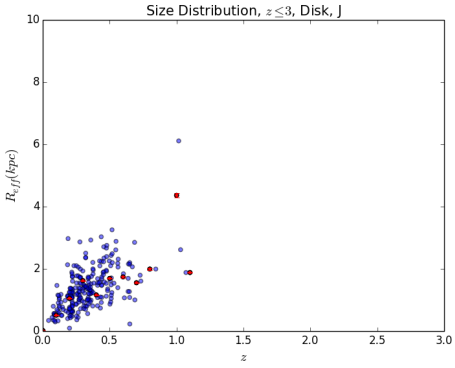
Size Distribution, $z \leq 3$, Disk, J
$R_{eff}(kpc)$
z

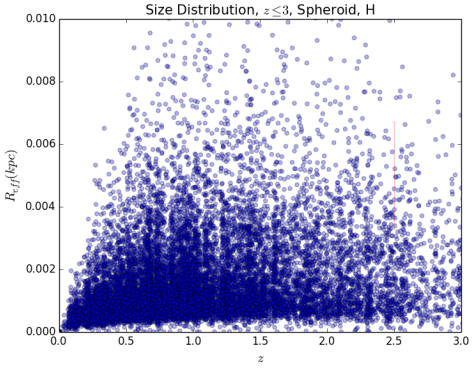
Size Distribution, $z \leq 3$, Spheroid, H
$R_{eff}(kpc)$
z

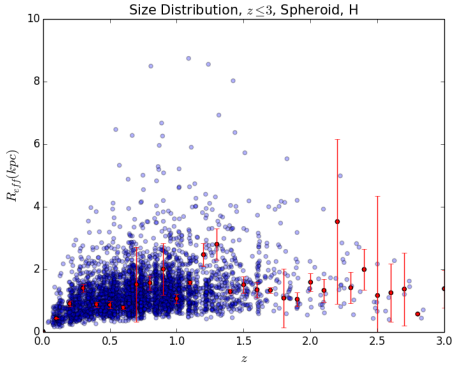
Size Distribution, $z \leq 3$, Spheroid, H
$R_{eff}(kpc)$
z

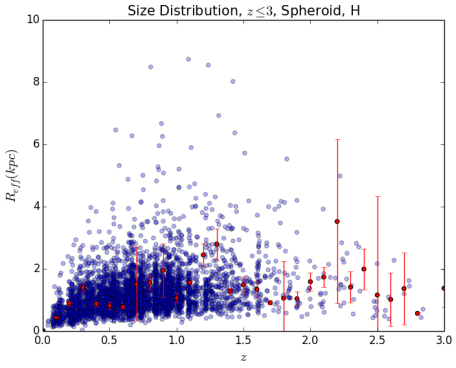
Size Distribution, $z \leq 3$, Spheroid, H
$R_{eff}(kpc)$
z

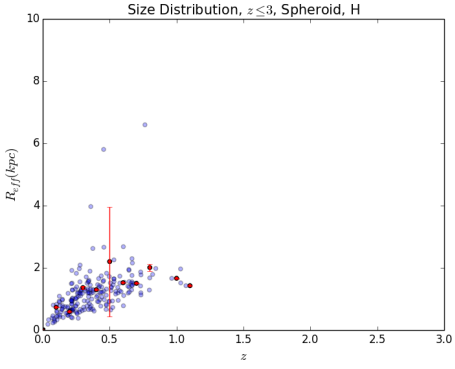
Size Distribution, $z \leq 3$, Spheroid, H
$R_{eff}(kpc)$
z

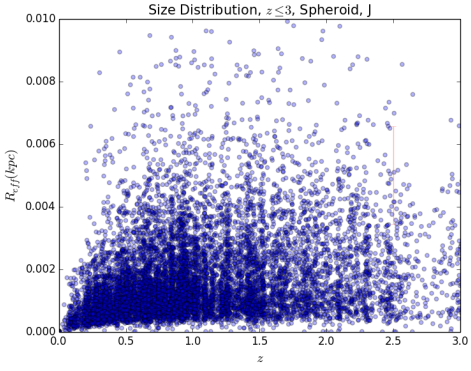
Size Distribution, $z \leq 3$, Spheroid, J
$R_{eff}(kpc)$
z

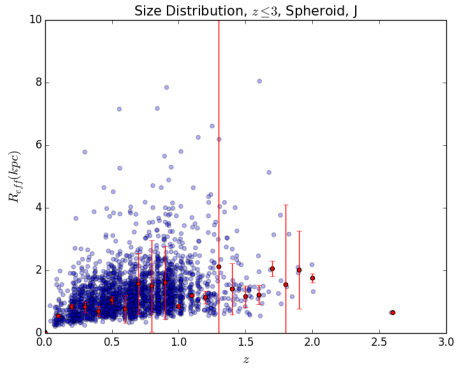
Size Distribution, $z \leq 3$, Spheroid, J
$R_{eff}(kpc)$
z

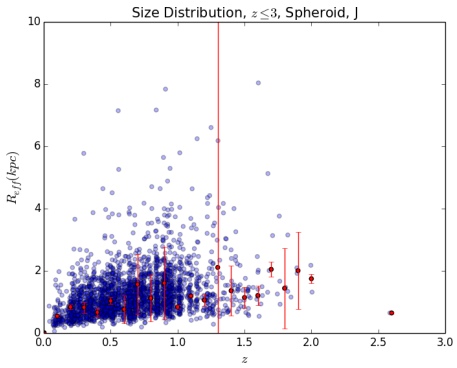
Size Distribution, $z \leq 3$, Spheroid, J
$R_{eff}(kpc)$
z

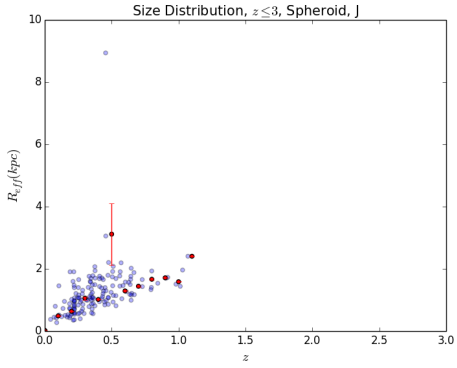
Size Distribution, $z \leq 3$, Spheroid, J
$R_{eff}(kpc)$
z

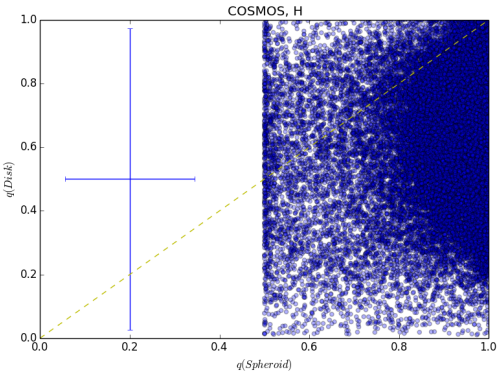
COSMOS, H
$q(Disk)$
$q(Spheroid)$

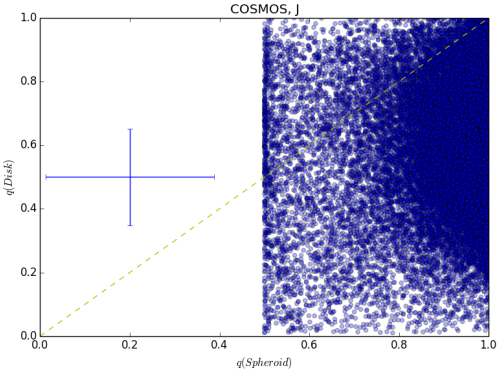
COSMOS, J
$q(Disk)$
$q(Spheroid)$

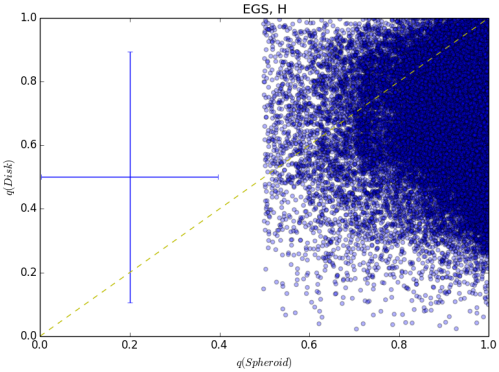
EGS, H
$q(Disk)$
$q(Spheroid)$

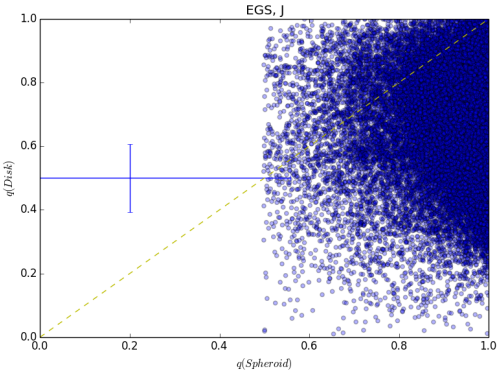
EGS, J
$q(Disk)$
$q(Spheroid)$

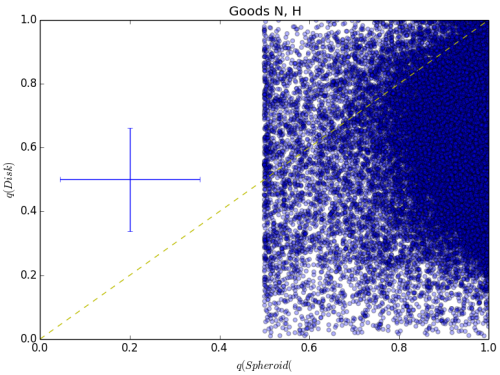
Goods N, H
q(Disk)
q(Spheroid(

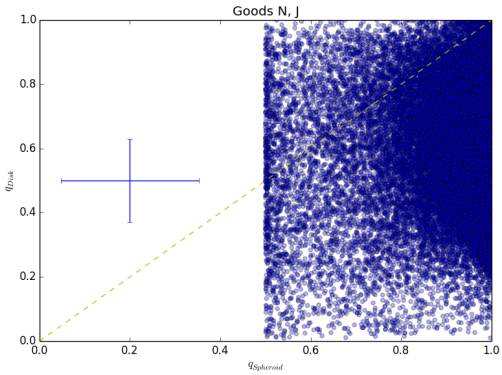
Goods N, J
q_{Disk}
$q_{Spheroid}$

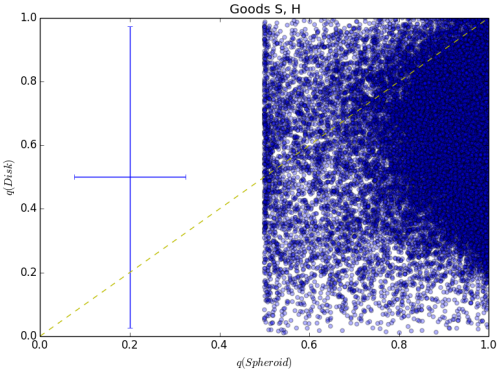
Goods S, H
q(Disk)
q(Spheroid)

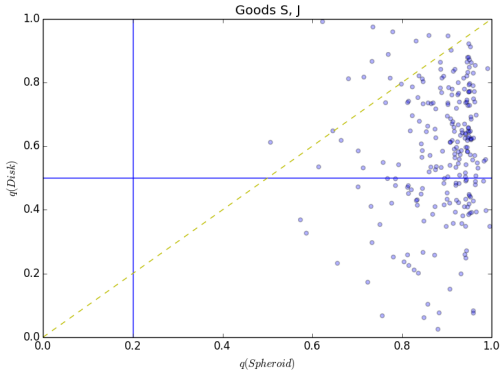
Goods S, J
q(Disk)
q(Spheroid)

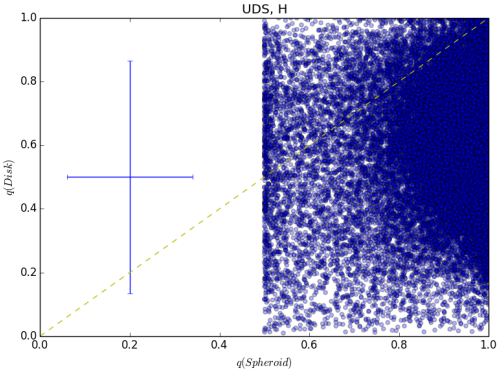
UDS, H
q(Disk)
q(Spheroid)

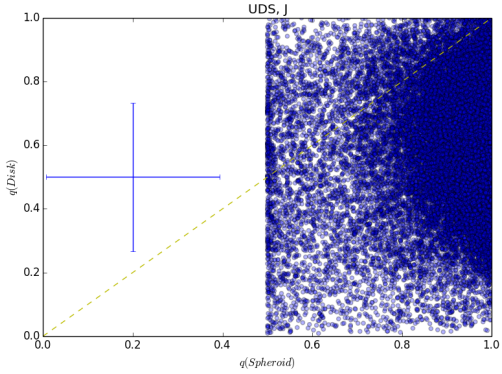
UDS, J
q(Disk)
q(Spheroid)

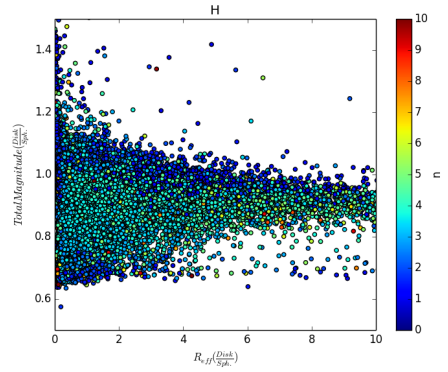
H
n

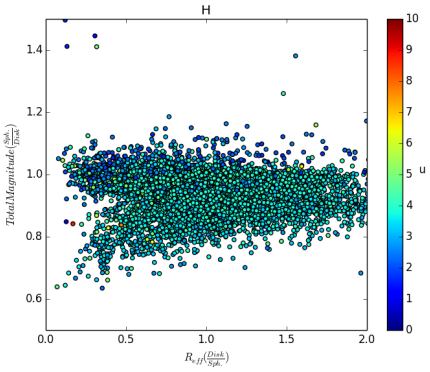
H
n

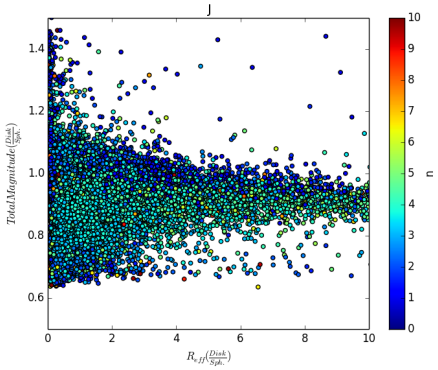
J
$Total Magnitude(\frac{Disk}{Sph.})$
$R_{eff}(\frac{Disk}{Sph.})$
n

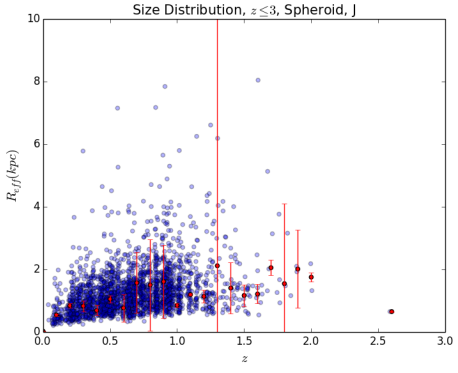
Size Distribution, $z \leq 3$, Spheroid, J
$R_{eff}(kpc)$
z

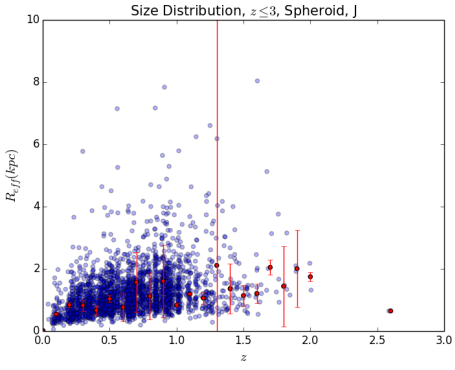
Size Distribution, $z \leq 3$, Spheroid, J
$R_{eff}(kpc)$
z

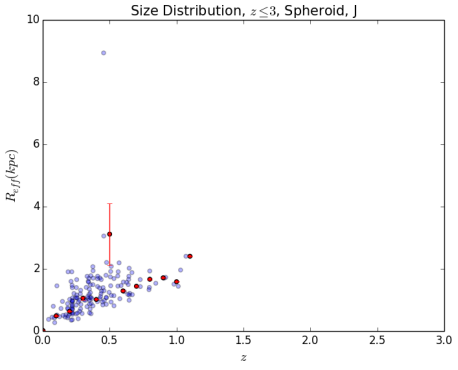
Size Distribution, $z \leq 3$, Spheroid, J
$R_{eff}(kpc)$
z

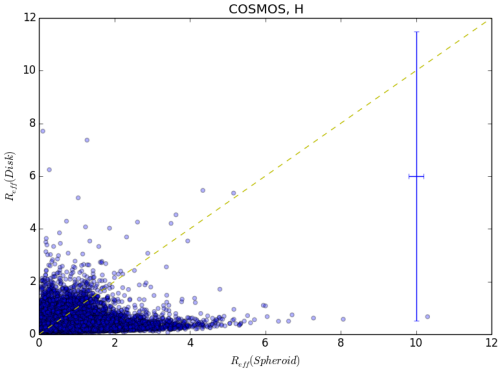
COSMOS, H
$R_{eff}(Disk)$
$R_{eff}(Spheroid)$

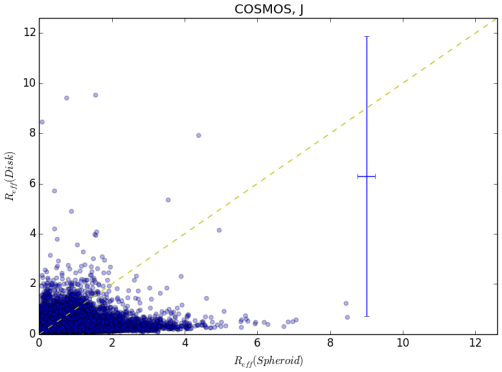
COSMOS, J
$R_{eff}(Disk)$
$R_{eff}(Spheroid)$

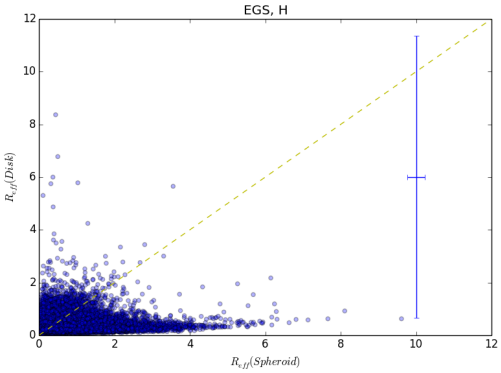
EGS, H
$R_{eff}(Disk)$
$R_{eff}(Spheroid)$

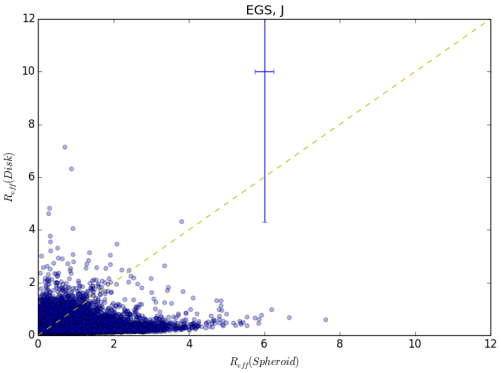
EGS, J
$R_{eff}(Disk)$
$R_{eff}(Spheroid)$

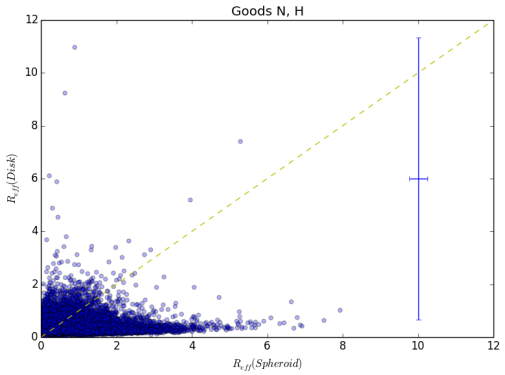
Goods N, H
$R_{eff}(Disk)$
$R_{eff}(Spheroid)$

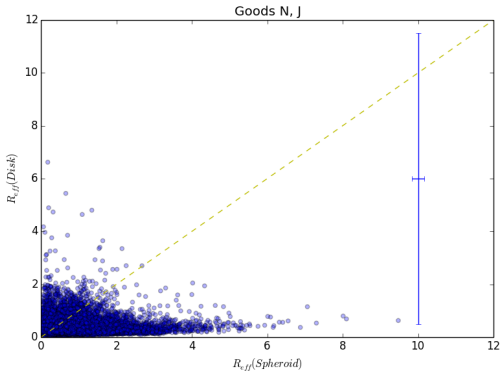
Goods N, J
$R_{eff}(Disk)$
$R_{eff}(Spheroid)$

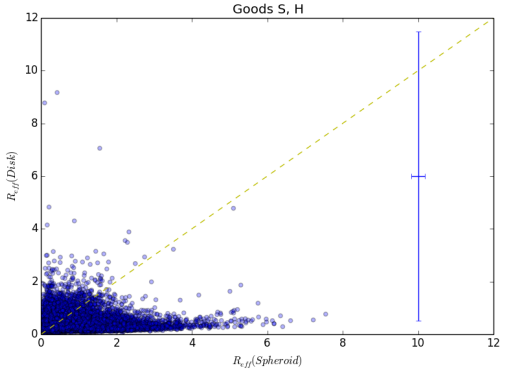
Goods S, H
$R_{eff}(Disk)$
$R_{eff}(Spheroid)$

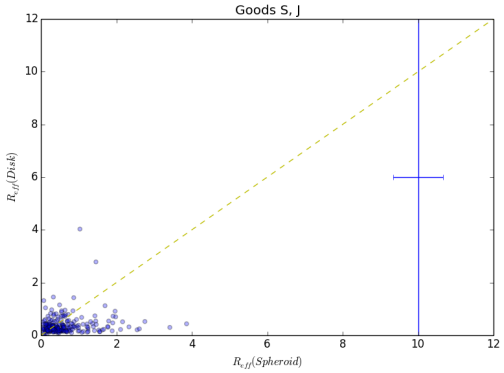
Goods S, J
$R_{eff}(Disk)$
$R_{eff}(Spheroid)$

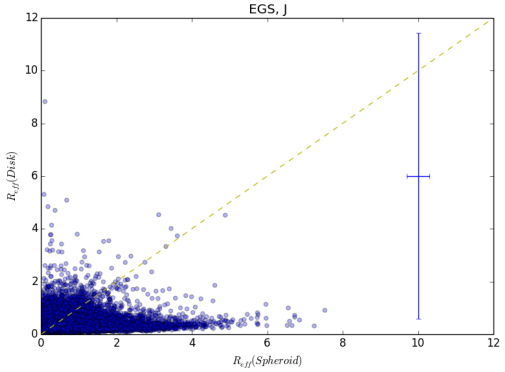
EGS, J
$R_{eff}(Disk)$
$R_{eff}(Spheroid)$

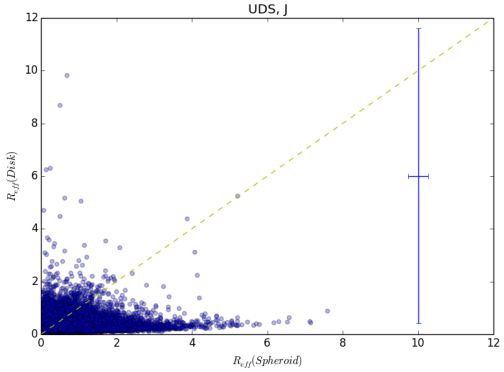
UDS, J
$R_{eff}(Disk)$
$R_{eff}(Spheroid)$

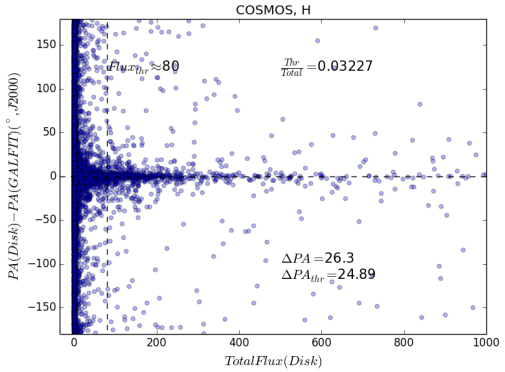
COSMOS, H
$Flux_{thr} \approx 80$
$\frac{Thr}{Total} = 0.03227$
$\Delta PA = 26.3$
$\Delta PA_{thr} = 24.89$
$PA(Disk) - PA(GALFIT)(^\circ, J2000)$
$TotalFlux(Disk)$

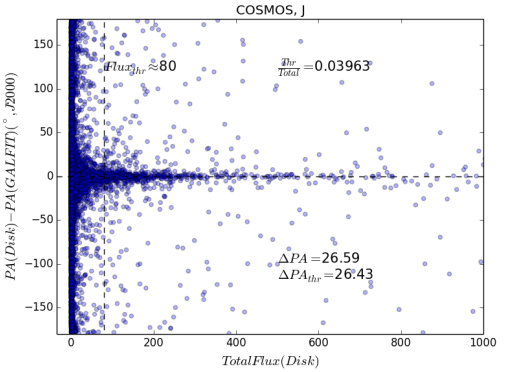
COSMOS, J
$Flux_{thr} \approx 80$
$\frac{Thr}{Total} = 0.03963$
$\Delta PA = 26.59$
$\Delta PA_{thr} = 26.43$
$PA(Disk) - PA(GALFIT)(^\circ, J2000)$
$TotalFlux(Disk)$

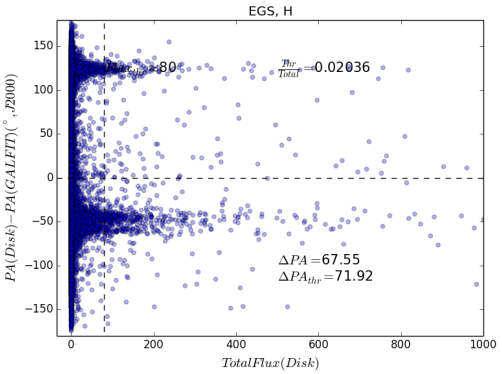
EGS, H
$Flux_{thr} \approx 80$
$\frac{Thr}{Total} = 0.02036$
$\Delta PA = 67.55$
$\Delta PA_{thr} = 71.92$
$PA(Disk) - PA(GALFIT)(^\circ, J2000)$
$TotalFlux(Disk)$

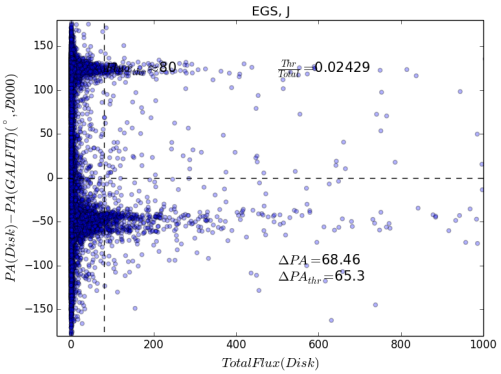
EGS, J
$Flux_{thr} \approx 80$
$\frac{Thr}{Total} = 0.02429$
$\Delta PA = 68.46$
$\Delta PA_{thr} = 65.3$
$PA(Disk) - PA(GALFIT)(^\circ, J2000)$
$TotalFlux(Disk)$

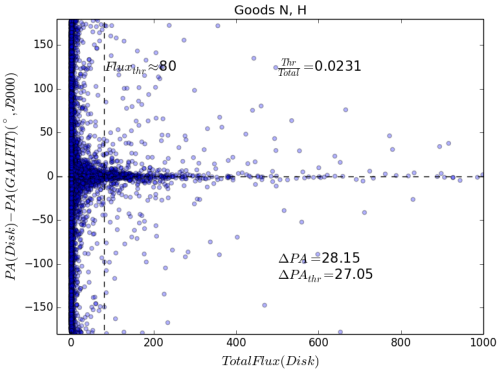
Goods N, H
$Flux_{thr} \approx 80$
$\frac{Thr}{Total} = 0.0231$
$\Delta PA = 28.15$
$\Delta PA_{thr} = 27.05$
$PA(Disk) - PA(GALFIT)(^\circ, J2000)$
$TotalFlux(Disk)$

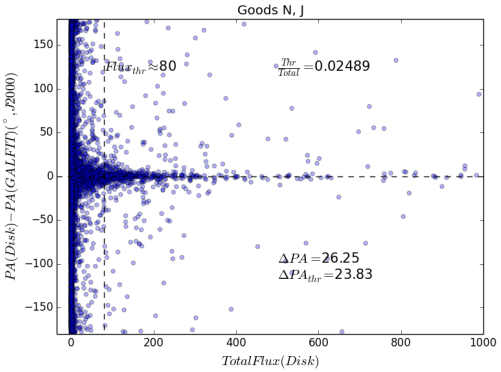
Goods N, J
$Flux_{thr} \approx 80$
$\frac{Thr}{Total} = 0.02489$
$\Delta PA = 26.25$
$\Delta PA_{thr} = 23.83$
$PA(Disk) - PA(GALFIT)(^\circ, J2000)$
$TotalFlux(Disk)$

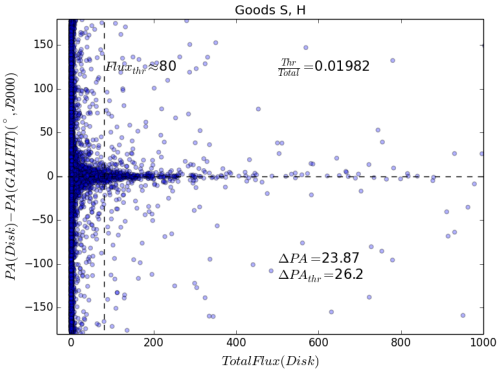
Goods S, H
$Flux_{thr} \approx 80$
$\frac{Thr}{Total} = 0.01982$
$\Delta PA = 23.87$
$\Delta PA_{thr} = 26.2$
$PA(Disk) - PA(GALFIT)(^\circ, J2000)$
$TotalFlux(Disk)$

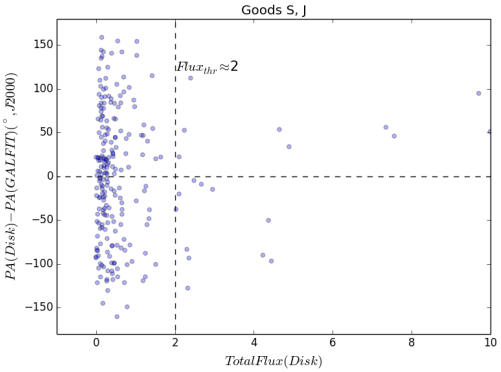
Goods S, J
$Flux_{thr} \approx 2$
$PA(Disk) - PA(GALFIT)(^\circ, J2000)$
$TotalFlux(Disk)$

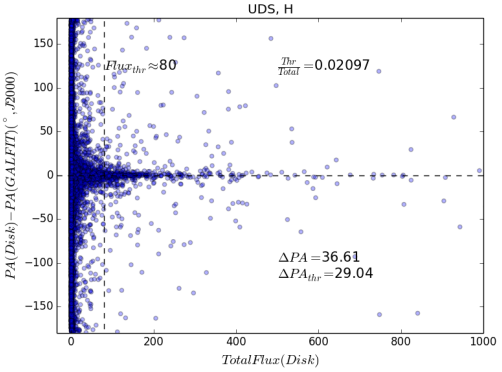
UDS, H
$Flux_{thr} \approx 80$
$\frac{Thr}{Total} = 0.02097$
$\Delta PA = 36.61$
$\Delta PA_{thr} = 29.04$
$PA(Disk) - PA(GALFIT)(^\circ, J2000)$
$TotalFlux(Disk)$

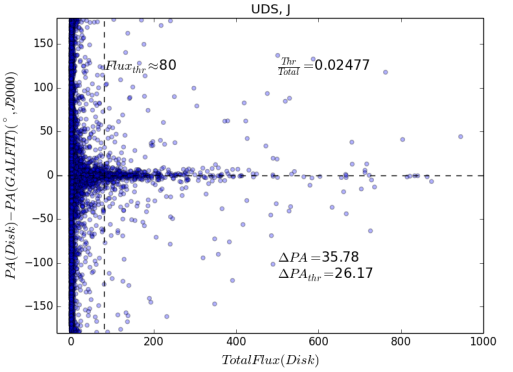
UDS, J
$Flux_{thr} \approx 80$
$\frac{Thr}{Total} = 0.02477$
$\Delta PA = 35.78$
$\Delta PA_{thr} = 26.17$
$PA(Disk) - PA(GALFIT)(^\circ, J2000)$
$TotalFlux(Disk)$

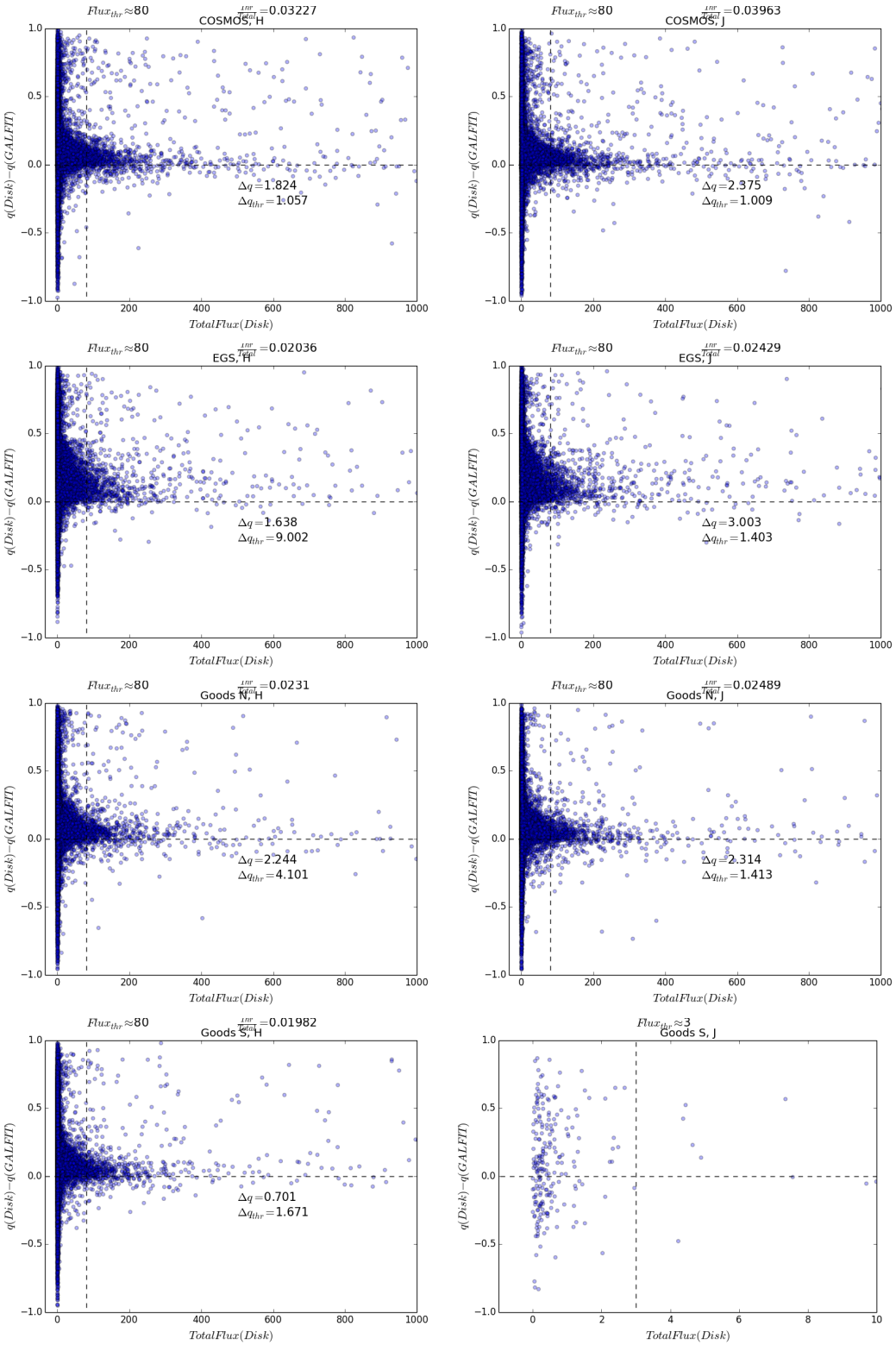
$Flux_{thr}\approx 80$
$\frac{Flux_{thr}}{Flux_{Total}}=0.03227$
COSMOS, H
$\Delta q=1.824$
$\Delta q_{thr}=1.057$
$Flux_{thr}\approx 80$
$\frac{Flux_{thr}}{Flux_{Total}}=0.03963$
COSMOS, J
$\Delta q=2.375$
$\Delta q_{thr}=1.009$
$Flux_{thr}\approx 80$
$\frac{Flux_{thr}}{Flux_{Total}}=0.02036$
EGS, H
$\Delta q=1.638$
$\Delta q_{thr}=9.002$
$Flux_{thr}\approx 80$
$\frac{Flux_{thr}}{Flux_{Total}}=0.02429$
EGS, J
$\Delta q=3.003$
$\Delta q_{thr}=1.403$
$Flux_{thr}\approx 80$
$\frac{Flux_{thr}}{Flux_{Total}}=0.0231$
Goods N, H
$\Delta q=2.244$
$\Delta q_{thr}=4.101$
$Flux_{thr}\approx 80$
$\frac{Flux_{thr}}{Flux_{Total}}=0.02489$
Goods N, J
$\Delta q=2.314$
$\Delta q_{thr}=1.413$
$Flux_{thr}\approx 80$
$\frac{Flux_{thr}}{Flux_{Total}}=0.01982$
Goods S, H
$\Delta q=0.701$
$\Delta q_{thr}=1.671$
$Flux_{thr}\approx 3$
Goods S, J
$q(Disk)-q(GALFIT)$
$TotalFlux(Disk)$

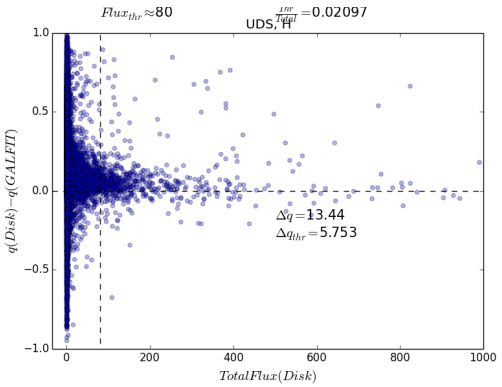
$Flux_{thr}\approx 80$
$\frac{Thr}{Total}=0.02097$
UDS, H
$\Delta q=13.44$
$\Delta q_{thr}=5.753$
$q(Disk)-q(GALFIT)$
$TotalFlux(Disk)$

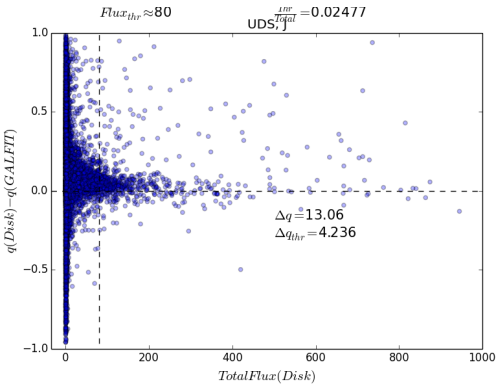
$Flux_{thr}\approx 80$
$\frac{Thr}{Total}=0.02477$
UDS, J
$\Delta q=13.06$
$\Delta q_{thr}=4.236$
$q(Disk)-q(GALFIT)$
$TotalFlux(Disk)$

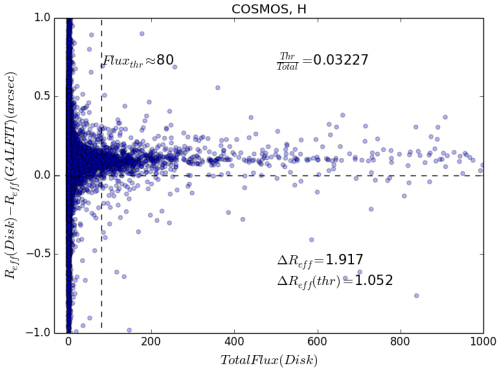
COSMOS, H
$Flux_{thr}\approx 80$
$\frac{Thr}{Total}=0.03227$
$\Delta R_{eff}=1.917$
$\Delta R_{eff}(thr)=1.052$
$R_{eff}(Disk)-R_{eff}(GALFIT)(arcsec)$
$TotalFlux(Disk)$

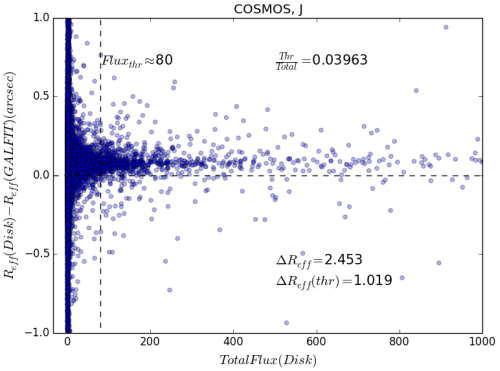
COSMOS, J
$Flux_{thr}\approx 80$
$\frac{Thr}{Total}=0.03963$
$\Delta R_{eff}=2.453$
$\Delta R_{eff}(thr)=1.019$
$R_{eff}(Disk)-R_{eff}(GALFIT)(arcsec)$
$TotalFlux(Disk)$

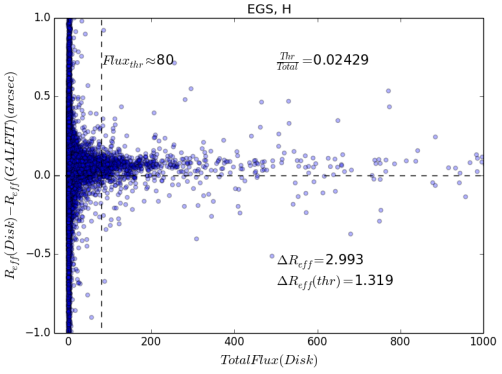
EGS, H
$Flux_{thr}\approx 80$
$\frac{Thr}{Total}=0.02429$
$\Delta R_{eff}=2.993$
$\Delta R_{eff}(thr)=1.319$
$R_{eff}(Disk)-R_{eff}(GALFIT)(arcsec)$
$TotalFlux(Disk)$

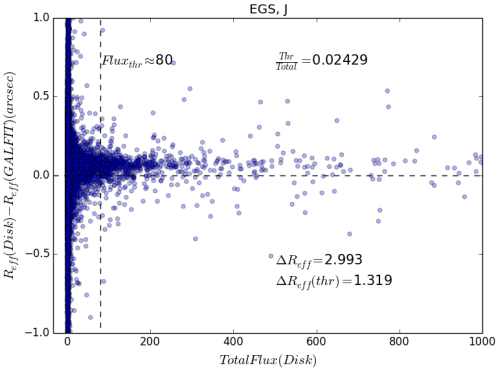
EGS, J
$Flux_{thr}\approx 80$
$\frac{Thr}{Total}=0.02429$
$\Delta R_{eff}=2.993$
$\Delta R_{eff}(thr)=1.319$
$R_{eff}(Disk)-R_{eff}(GALFIT)(arcsec)$
$TotalFlux(Disk)$

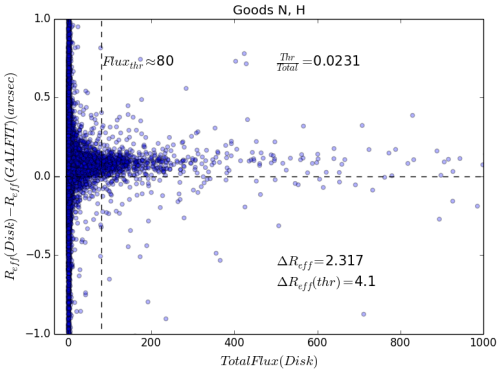
Goods N, H
$Flux_{thr}\approx 80$
$\frac{Thr}{Total}=0.0231$
$\Delta R_{eff}=2.317$
$\Delta R_{eff}(thr)=4.1$
$R_{eff}(Disk)-R_{eff}(GALFIT)(arcsec)$
$TotalFlux(Disk)$

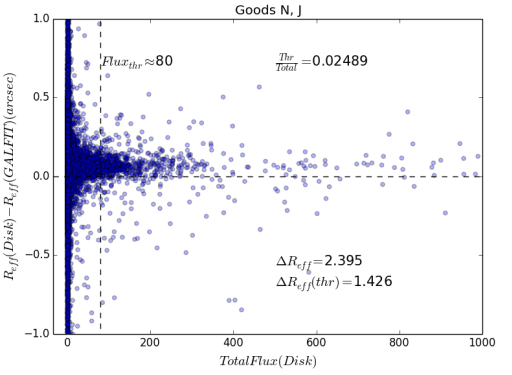
Goods N, J
$Flux_{thr}\approx 80$
$\frac{Thr}{Total}=0.02489$
$\Delta R_{eff}=2.395$
$\Delta R_{eff}(thr)=1.426$
$R_{eff}(Disk)-R_{eff}(GALFIT)(arcsec)$
$TotalFlux(Disk)$

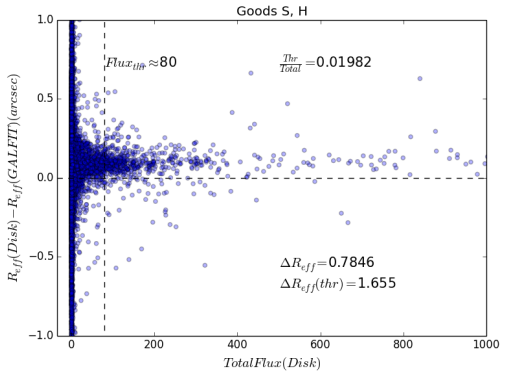
Goods S, H
$Flux_{thr}$≈80
$\frac{Thr}{Total}$=0.01982
ΔR_{eff}=0.7846
$\Delta R_{eff}(thr)$=1.655
$R_{eff}(Disk) - R_{eff}(GALFIT)(arcsec)$
$TotalFlux(Disk)$

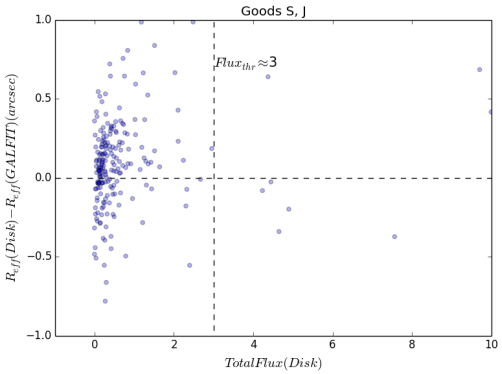
Goods S, J
$Flux_{thr}$≈3
$R_{eff}(Disk) - R_{eff}(GALFIT)(arcsec)$
$TotalFlux(Disk)$

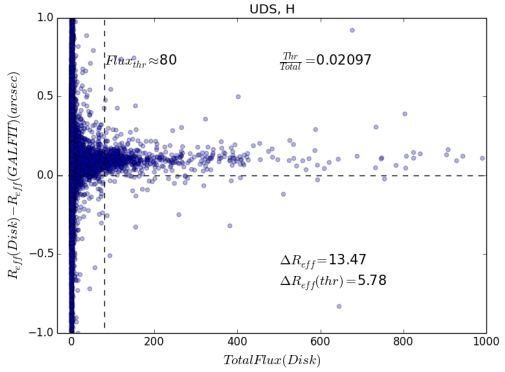
UDS, H
$Flux_{thr}$≈80
$\frac{Thr}{Total}$=0.02097
ΔR_{eff}=13.47
$\Delta R_{eff}(thr)$=5.78
$R_{eff}(Disk) - R_{eff}(GALFIT)(arcsec)$
$TotalFlux(Disk)$

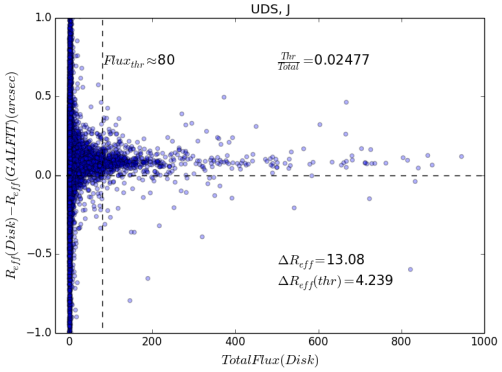
UDS, J
$Flux_{thr}$≈80
$\frac{Thr}{Total}$=0.02477
ΔR_{eff}=13.08
$\Delta R_{eff}(thr)$=4.239
$R_{eff}(Disk) - R_{eff}(GALFIT)(arcsec)$
$TotalFlux(Disk)$

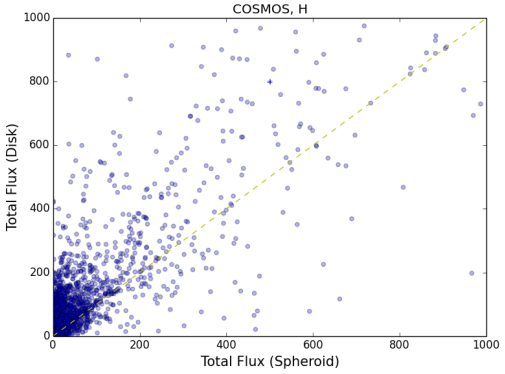
COSMOS, H
Total Flux (Disk)
Total Flux (Spheroid)

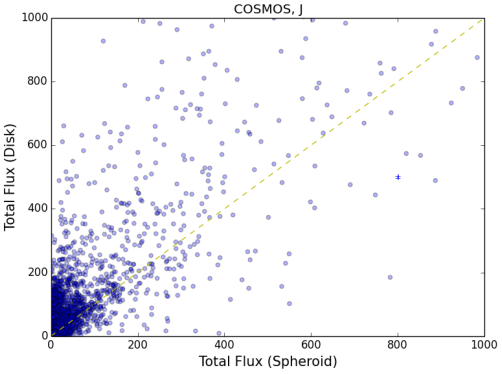
COSMOS, J
Total Flux (Disk)
Total Flux (Spheroid)

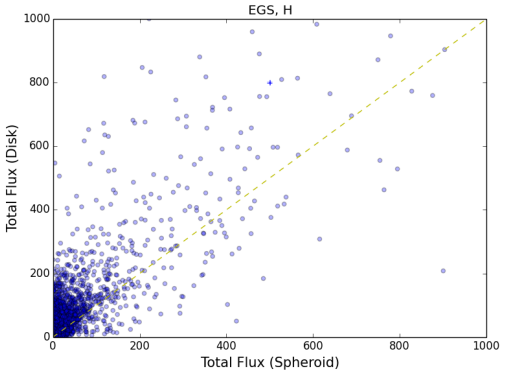
EGS, H
Total Flux (Disk)
Total Flux (Spheroid)

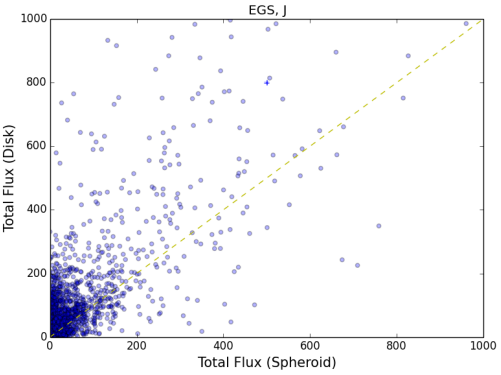
EGS, J
Total Flux (Disk)
Total Flux (Spheroid)

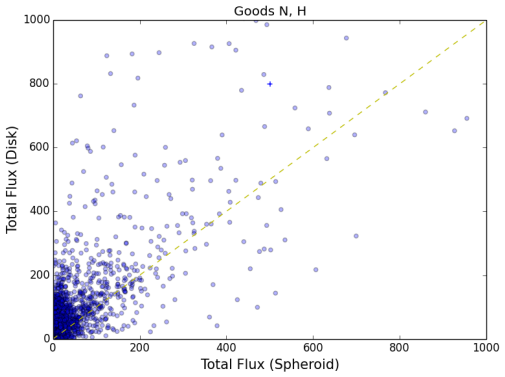
Goods N, H
Total Flux (Disk)
Total Flux (Spheroid)

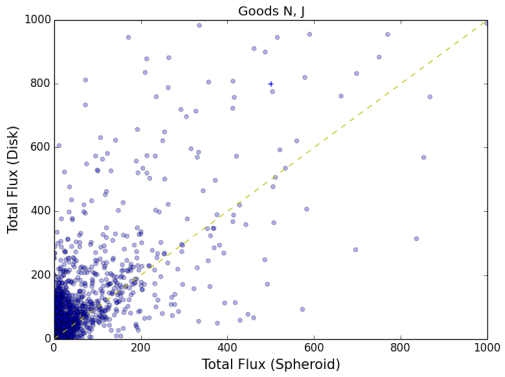
Goods N, J
Total Flux (Disk)
Total Flux (Spheroid)

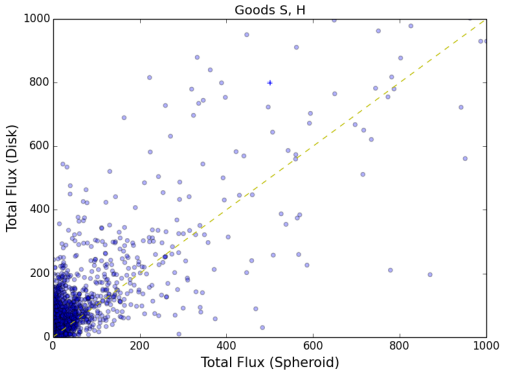
Goods S, H
Total Flux (Disk)
Total Flux (Spheroid)

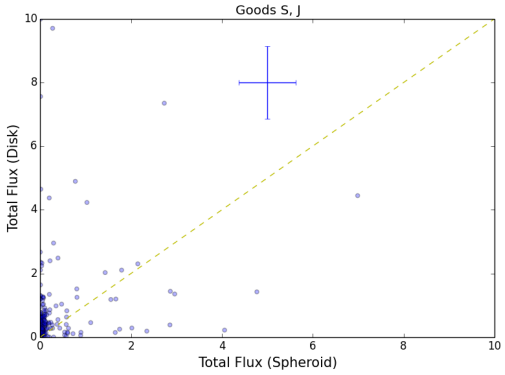
Goods S, J
Total Flux (Disk)
Total Flux (Spheroid)

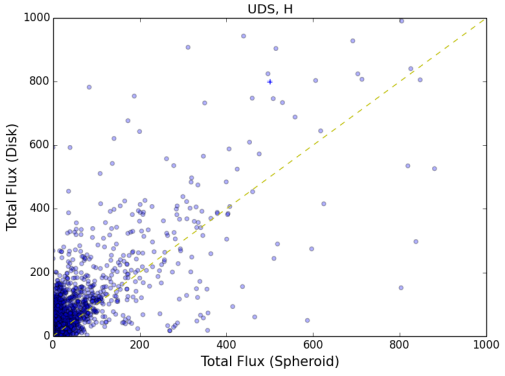
UDS, H
Total Flux (Disk)
Total Flux (Spheroid)

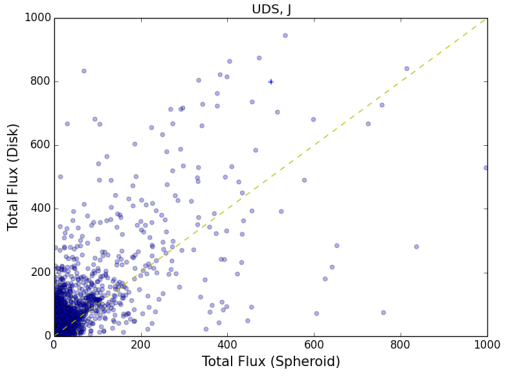
UDS, J
Total Flux (Disk)
Total Flux (Spheroid)

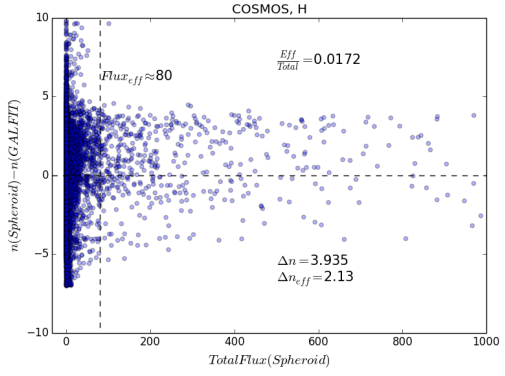
COSMOS, H
$\frac{Eff}{Total}$=0.0172
$Flux_{eff}\approx$80
Δn=3.935
Δn_{eff}=2.13
$n(Spheroid)-n(GALFIT)$
$TotalFlux(Spheroid)$

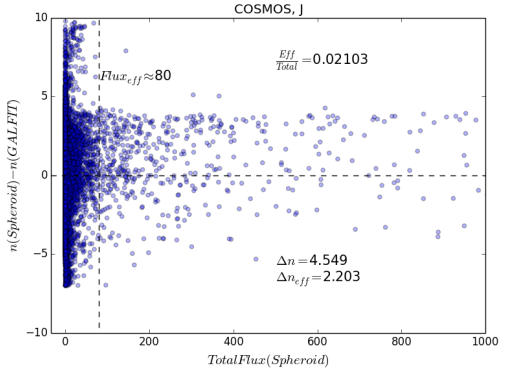
COSMOS, J
$\frac{Eff}{Total}$=0.02103
$Flux_{eff}\approx$80
Δn=4.549
Δn_{eff}=2.203
$n(Spheroid)-n(GALFIT)$
$TotalFlux(Spheroid)$

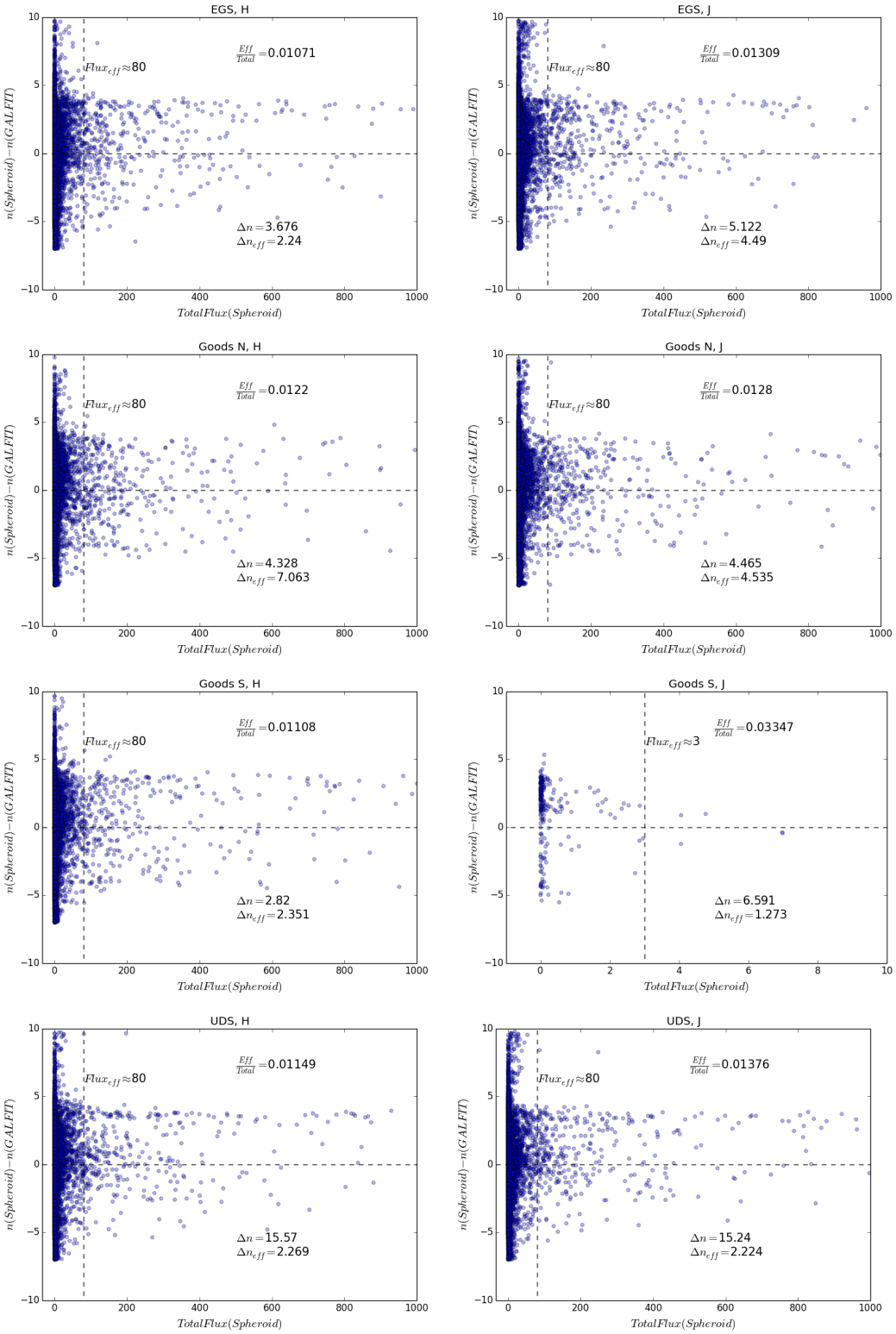
EGS, H
$\frac{Eff}{Total}$=0.01071
$Flux_{eff}\approx80$
Δn=3.676
Δn_{eff}=2.24
EGS, J
$\frac{Eff}{Total}$=0.01309
$Flux_{eff}\approx80$
Δn=5.122
Δn_{eff}=4.49
Goods N, H
$\frac{Eff}{Total}$=0.0122
$Flux_{eff}\approx80$
Δn=4.328
Δn_{eff}=7.063
Goods N, J
$\frac{Eff}{Total}$=0.0128
$Flux_{eff}\approx80$
Δn=4.465
Δn_{eff}=4.535
Goods S, H
$\frac{Eff}{Total}$=0.01108
$Flux_{eff}\approx80$
Δn=2.82
Δn_{eff}=2.351
Goods S, J
$\frac{Eff}{Total}$=0.03347
$Flux_{eff}\approx3$
Δn=6.591
Δn_{eff}=1.273
UDS, H
$\frac{Eff}{Total}$=0.01149
$Flux_{eff}\approx80$
Δn=15.57
Δn_{eff}=2.269
UDS, J
$\frac{Eff}{Total}$=0.01376
$Flux_{eff}\approx80$
Δn=15.24
Δn_{eff}=2.224
$n(Spheroid)-n(GALFIT)$
$TotalFlux(Spheroid)$

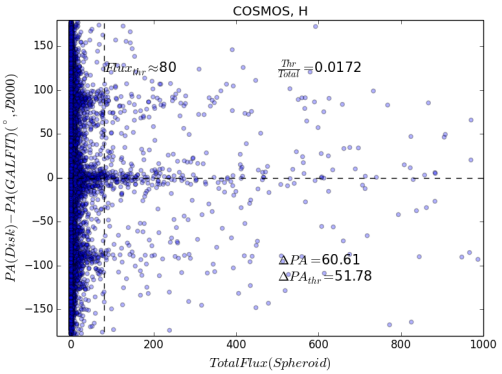
COSMOS, H
$Flux_{thr} \approx 80$
$\frac{Thr}{Total} = 0.0172$
$\Delta PA = 60.61$
$\Delta PA_{thr} = 51.78$
$PA(Disk) - PA(GALFIT)(^\circ, J2000)$
$TotalFlux(Spheroid)$

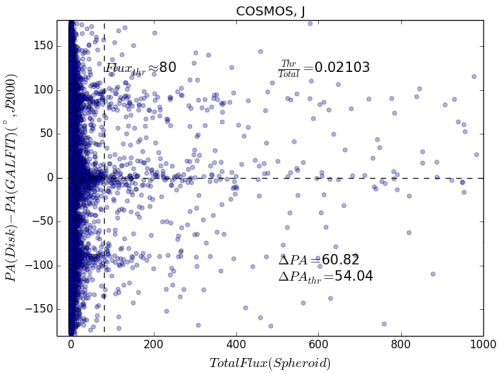
COSMOS, J
$Flux_{thr} \approx 80$
$\frac{Thr}{Total} = 0.02103$
$\Delta PA = 60.82$
$\Delta PA_{thr} = 54.04$
$PA(Disk) - PA(GALFIT)(^\circ, J2000)$
$TotalFlux(Spheroid)$

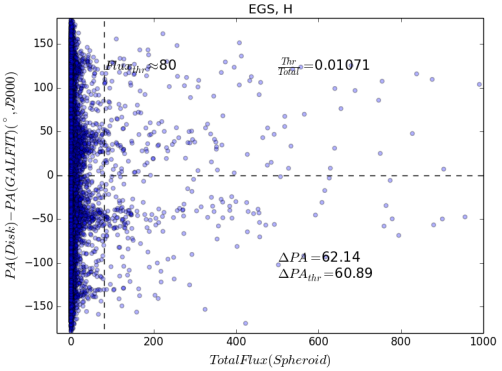
EGS, H
$Flux_{thr} \approx 80$
$\frac{Thr}{Total} = 0.01071$
$\Delta PA = 62.14$
$\Delta PA_{thr} = 60.89$
$PA(Disk) - PA(GALFIT)(^\circ, J2000)$
$TotalFlux(Spheroid)$

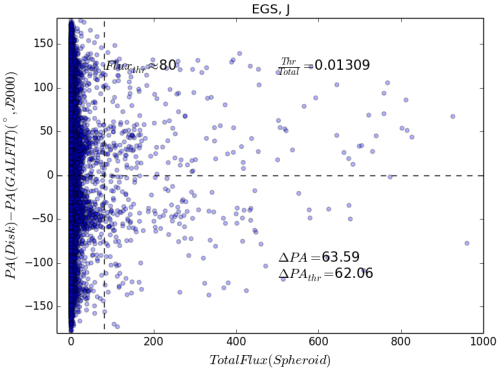
EGS, J
$Flux_{thr} \approx 80$
$\frac{Thr}{Total} = 0.01309$
$\Delta PA = 63.59$
$\Delta PA_{thr} = 62.06$
$PA(Disk) - PA(GALFIT)(^\circ, J2000)$
$TotalFlux(Spheroid)$

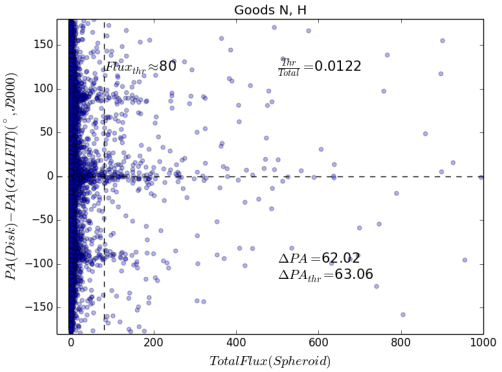
Goods N, H
$Flux_{thr} \approx 80$
$\frac{Thr}{Total} = 0.0122$
$\Delta PA = 62.02$
$\Delta PA_{thr} = 63.06$
$PA(Disk) - PA(GALFIT)(^\circ, J2000)$
$TotalFlux(Spheroid)$

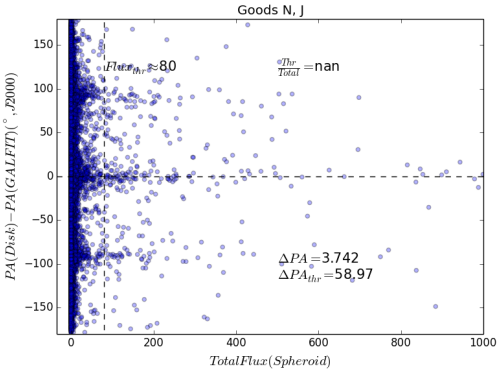
Goods N, J
$Flux_{thr} \approx 80$
$\frac{Thr}{Total} = nan$
$\Delta PA = 3.742$
$\Delta PA_{thr} = 58.97$
$PA(Disk) - PA(GALFIT)(^\circ, J2000)$
$TotalFlux(Spheroid)$

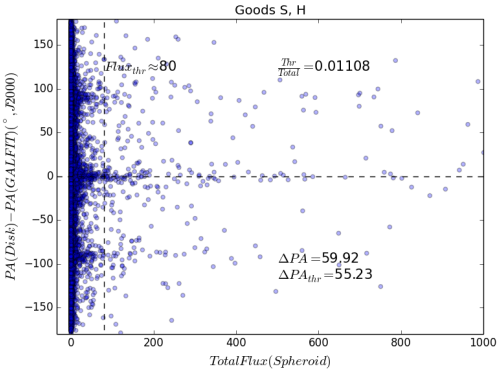
Goods S, H
$Flux_{thr} \approx 80$
$\frac{Thr}{Total} = 0.01108$
$\Delta PA = 59.92$
$\Delta PA_{thr} = 55.23$
$PA(Disk) - PA(GALFIT)(^\circ, J2000)$
$TotalFlux(Spheroid)$

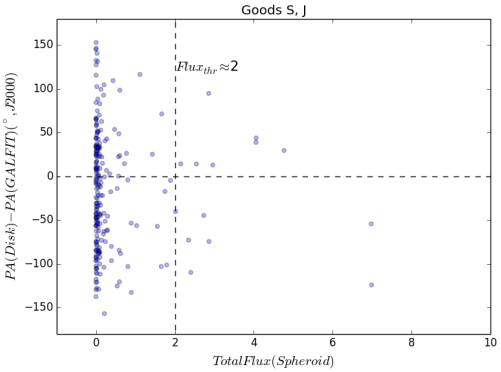
Goods S, J
$Flux_{thr} \approx 2$
$PA(Disk) - PA(GALFIT)(^\circ, J2000)$
$TotalFlux(Spheroid)$

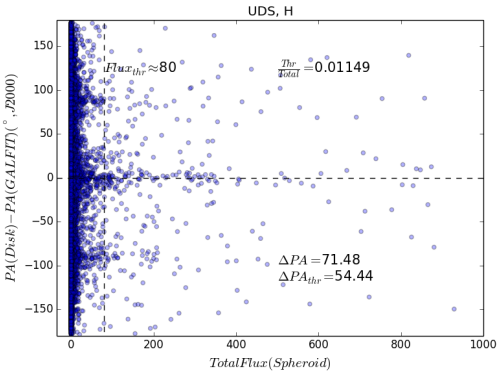
UDS, H
$Flux_{thr} \approx 80$
$\frac{Thr}{Total}$=0.01149
ΔPA=71.48
ΔPA_{thr}=54.44
$PA(Disk) - PA(GALFIT)(^\circ, J2000)$
$TotalFlux(Spheroid)$

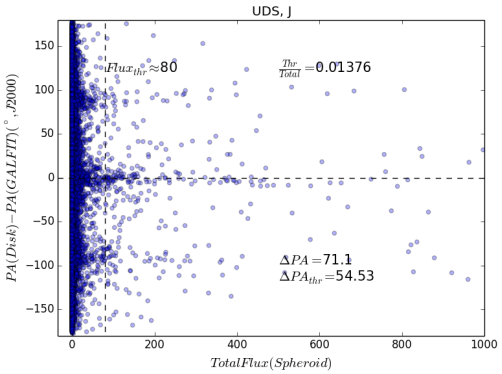
UDS, J
$Flux_{thr} \approx 80$
$\frac{Thr}{Total}$=0.01376
ΔPA=71.1
ΔPA_{thr}=54.53
$PA(Disk) - PA(GALFIT)(^\circ, J2000)$
$TotalFlux(Spheroid)$

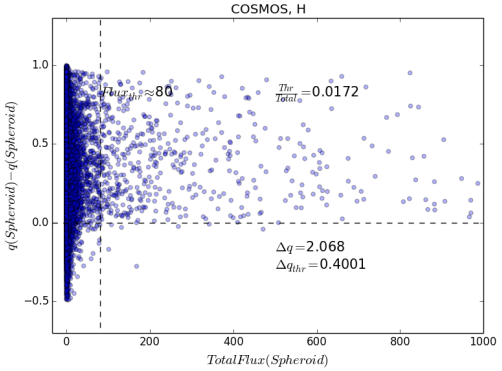
COSMOS, H
$Flux_{thr} \approx 80$
$\frac{Thr}{Total}$=0.0172
Δq=2.068
Δq_{thr}=0.4001
$q(Spheroid) - q(Spheroid)$
$TotalFlux(Spheroid)$

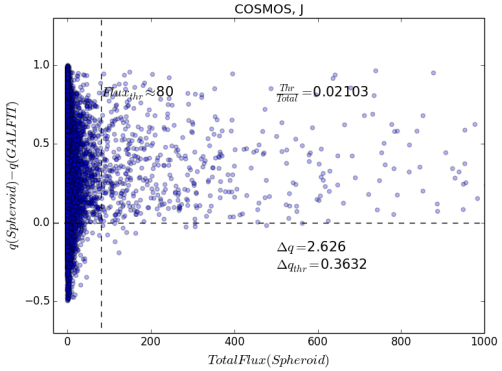
COSMOS, J
$Flux_{thr} \approx 80$
$\frac{Thr}{Total}$=0.02103
Δq=2.626
Δq_{thr}=0.3632
$q(Spheroid) - q(GALFIT)$
$TotalFlux(Spheroid)$

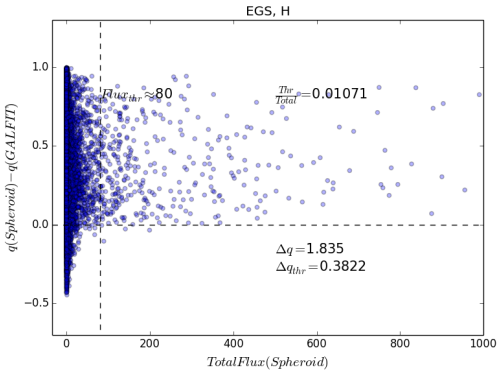
EGS, H
$Flux_{thr} \approx 80$
$\frac{Thr}{Total}$=0.01071
Δq=1.835
Δq_{thr}=0.3822
$q(Spheroid) - q(GALFIT)$
$TotalFlux(Spheroid)$

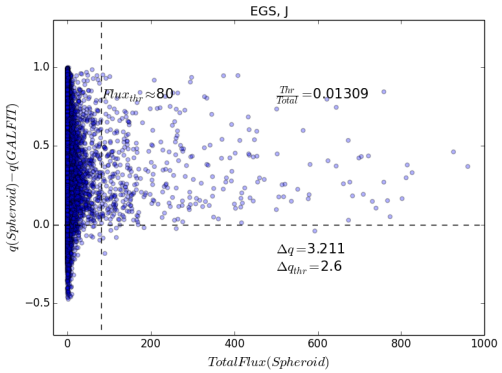
EGS, J
$Flux_{thr} \approx 80$
$\frac{Thr}{Total}$=0.01309
Δq=3.211
Δq_{thr}=2.6
$q(Spheroid) - q(GALFIT)$
$TotalFlux(Spheroid)$

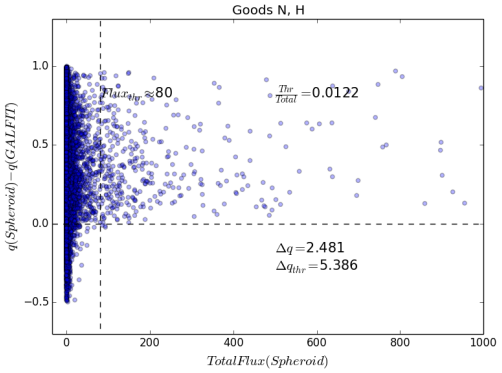
Goods N, H
$Flux_{thr} \approx 80$
$\frac{Thr}{Total}$=0.0122
Δq=2.481
Δq_{thr}=5.386
$q(Spheroid) - q(GALFIT)$
$TotalFlux(Spheroid)$

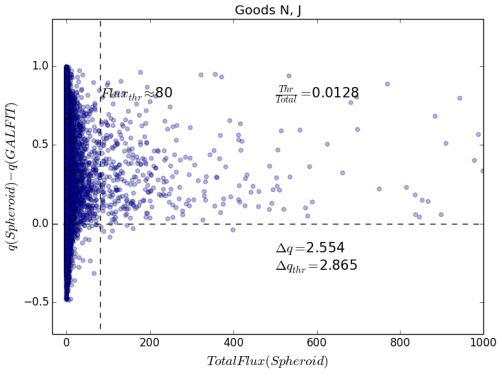
Goods N, J
$Flux_{thr} \approx 80$
$\frac{Thr}{Total}$=0.0128
Δq=2.554
Δq_{thr}=2.865
$q(Spheroid) - q(GALFIT)$
$TotalFlux(Spheroid)$

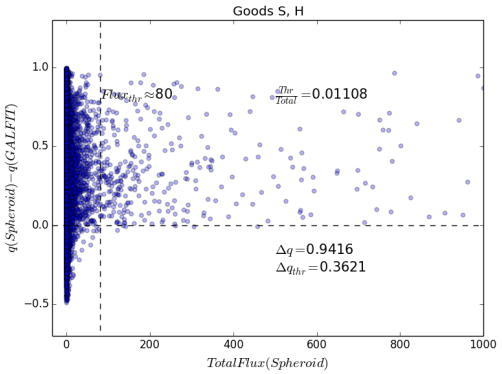
Goods S, H
$Flux_{thr} \approx 80$
$\frac{Thr}{Total} = 0.01108$
$\Delta q = 0.9416$
$\Delta q_{thr} = 0.3621$
$q(Spheroid) - q(GALFIT)$
$TotalFlux(Spheroid)$

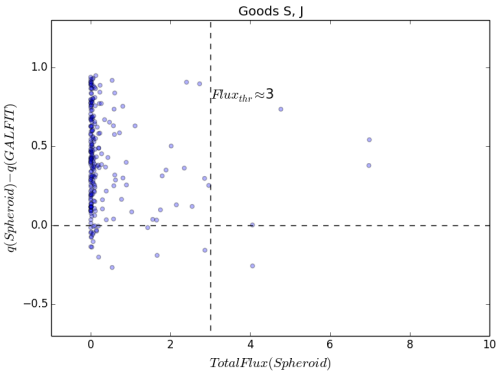
Goods S, J
$Flux_{thr} \approx 3$
$q(Spheroid) - q(GALFIT)$
$TotalFlux(Spheroid)$

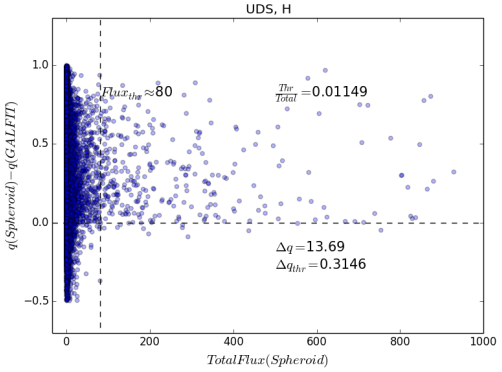
UDS, H
$Flux_{thr} \approx 80$
$\frac{Thr}{Total} = 0.01149$
$\Delta q = 13.69$
$\Delta q_{thr} = 0.3146$
$q(Spheroid) - q(GALFIT)$
$TotalFlux(Spheroid)$

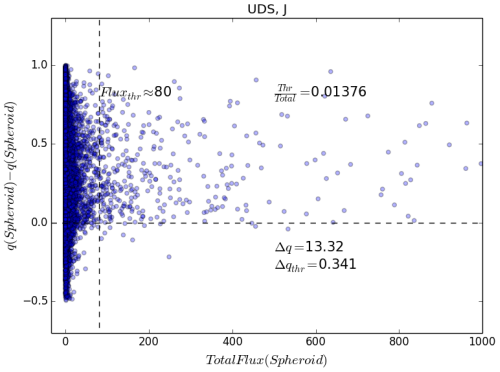
UDS, J
$Flux_{thr} \approx 80$
$\frac{Thr}{Total} = 0.01376$
$\Delta q = 13.32$
$\Delta q_{thr} = 0.341$
$q(Spheroid) - q(Spheroid)$
$TotalFlux(Spheroid)$

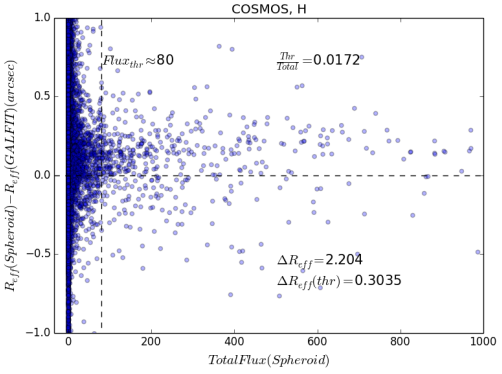
COSMOS, H
$Flux_{thr} \approx 80$
$\frac{Thr}{Total} = 0.0172$
$\Delta R_{eff} = 2.204$
$\Delta R_{eff}(thr) = 0.3035$
$R_{eff}(Spheroid) - R_{eff}(GALFIT)(arcsec)$
$TotalFlux(Spheroid)$

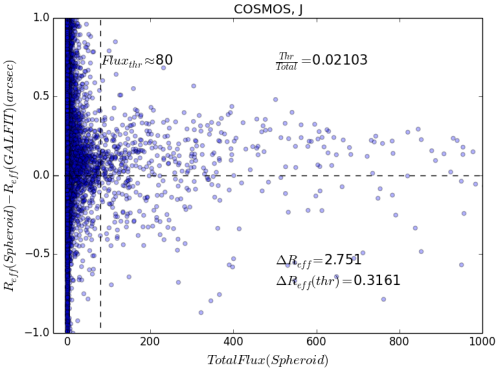
COSMOS, J
$Flux_{thr} \approx 80$
$\frac{Thr}{Total} = 0.02103$
$\Delta R_{eff} = 2.751$
$\Delta R_{eff}(thr) = 0.3161$
$R_{eff}(Spheroid) - R_{eff}(GALFIT)(arcsec)$
$TotalFlux(Spheroid)$

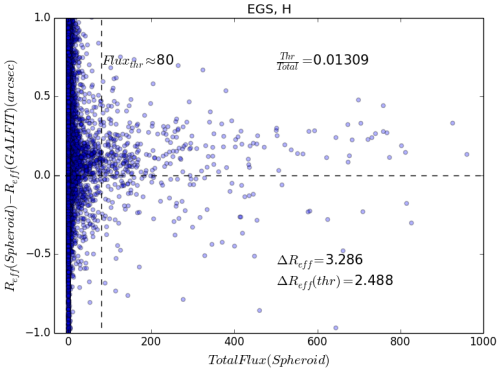
EGS, H
$Flux_{thr} \approx 80$
$\frac{Thr}{Total} = 0.01309$
$\Delta R_{eff} = 3.286$
$\Delta R_{eff}(thr) = 2.488$
$R_{eff}(Spheroid) - R_{eff}(GALFIT)(arcsec)$
$TotalFlux(Spheroid)$

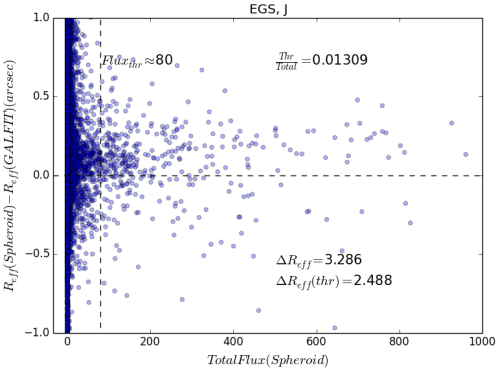
EGS, J
$Flux_{thr} \approx 80$
$\frac{Thr}{Total} = 0.01309$
$\Delta R_{eff} = 3.286$
$\Delta R_{eff}(thr) = 2.488$
$R_{eff}(Spheroid) - R_{eff}(GALFIT)(arcsec)$
$TotalFlux(Spheroid)$

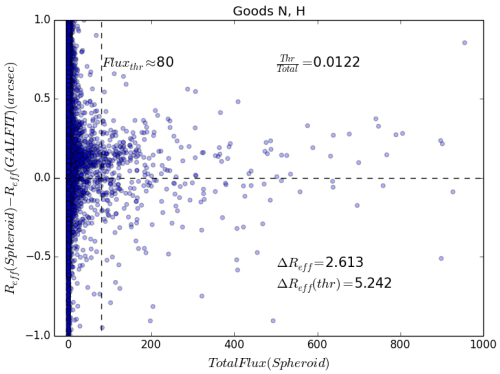
Goods N, H
$Flux_{thr}\approx 80$
$\frac{Thr}{Total}=0.0122$
$\Delta R_{eff}=2.613$
$\Delta R_{eff}(thr)=5.242$
$R_{eff}(Spheroid)-R_{eff}(GALFIT)(arcsec)$
$TotalFlux(Spheroid)$

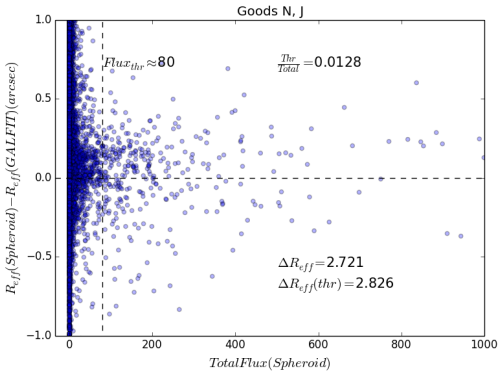
Goods N, J
$Flux_{thr}\approx 80$
$\frac{Thr}{Total}=0.0128$
$\Delta R_{eff}=2.721$
$\Delta R_{eff}(thr)=2.826$
$R_{eff}(Spheroid)-R_{eff}(GALFIT)(arcsec)$
$TotalFlux(Spheroid)$

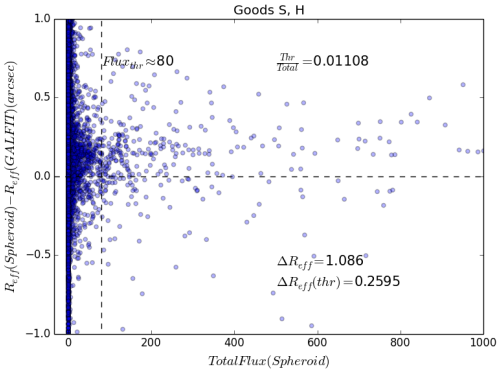
Goods S, H
$Flux_{thr}\approx 80$
$\frac{Thr}{Total}=0.01108$
$\Delta R_{eff}=1.086$
$\Delta R_{eff}(thr)=0.2595$
$R_{eff}(Spheroid)-R_{eff}(GALFIT)(arcsec)$
$TotalFlux(Spheroid)$

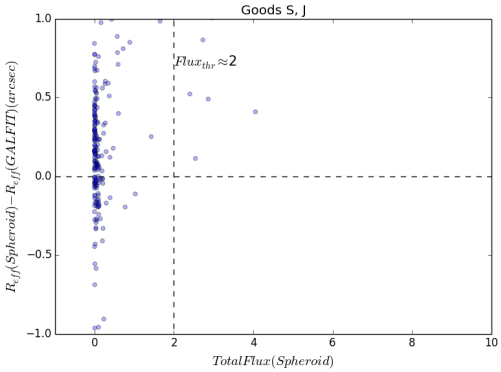
Goods S, J
$Flux_{thr}\approx 2$
$R_{eff}(Spheroid)-R_{eff}(GALFIT)(arcsec)$
$TotalFlux(Spheroid)$

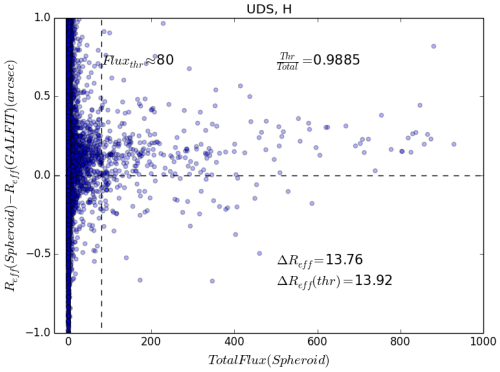
UDS, H
$Flux_{thr}\approx 80$
$\frac{Thr}{Total}=0.9885$
$\Delta R_{eff}=13.76$
$\Delta R_{eff}(thr)=13.92$
$R_{eff}(Spheroid)-R_{eff}(GALFIT)(arcsec)$
$TotalFlux(Spheroid)$

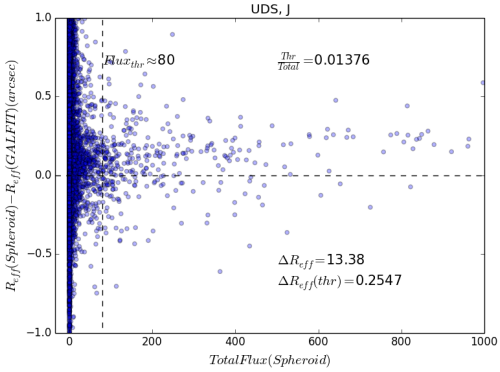
UDS, J
$Flux_{thr}\approx 80$
$\frac{Thr}{Total}=0.01376$
$\Delta R_{eff}=13.38$
$\Delta R_{eff}(thr)=0.2547$
$R_{eff}(Spheroid)-R_{eff}(GALFIT)(arcsec)$
$TotalFlux(Spheroid)$

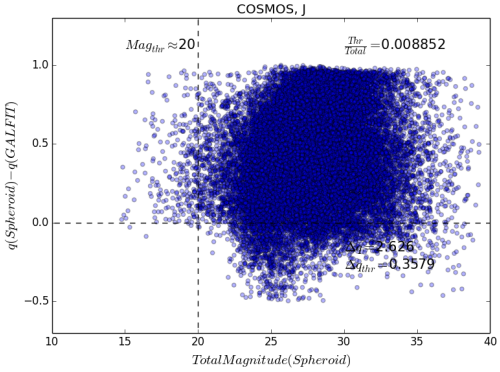
COSMOS, J
$Mag_{thr}\approx 20$
$\frac{Thr}{Total}=0.008852$
$\Delta_{eff}=2.626$
$\Delta_{q_{thr}}=0.3579$
$q(Spheroid)-q(GALFIT)$
$TotalMagnitude(Spheroid)$

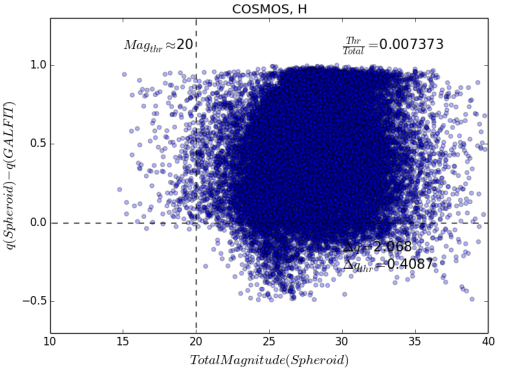
COSMOS, H
$Mag_{thr}\approx 20$
$\frac{Thr}{Total}=0.007373$
$\Delta_{eff}=2.068$
$\Delta_{q_{thr}}=0.4087$
$q(Spheroid)-q(GALFIT)$
$TotalMagnitude(Spheroid)$

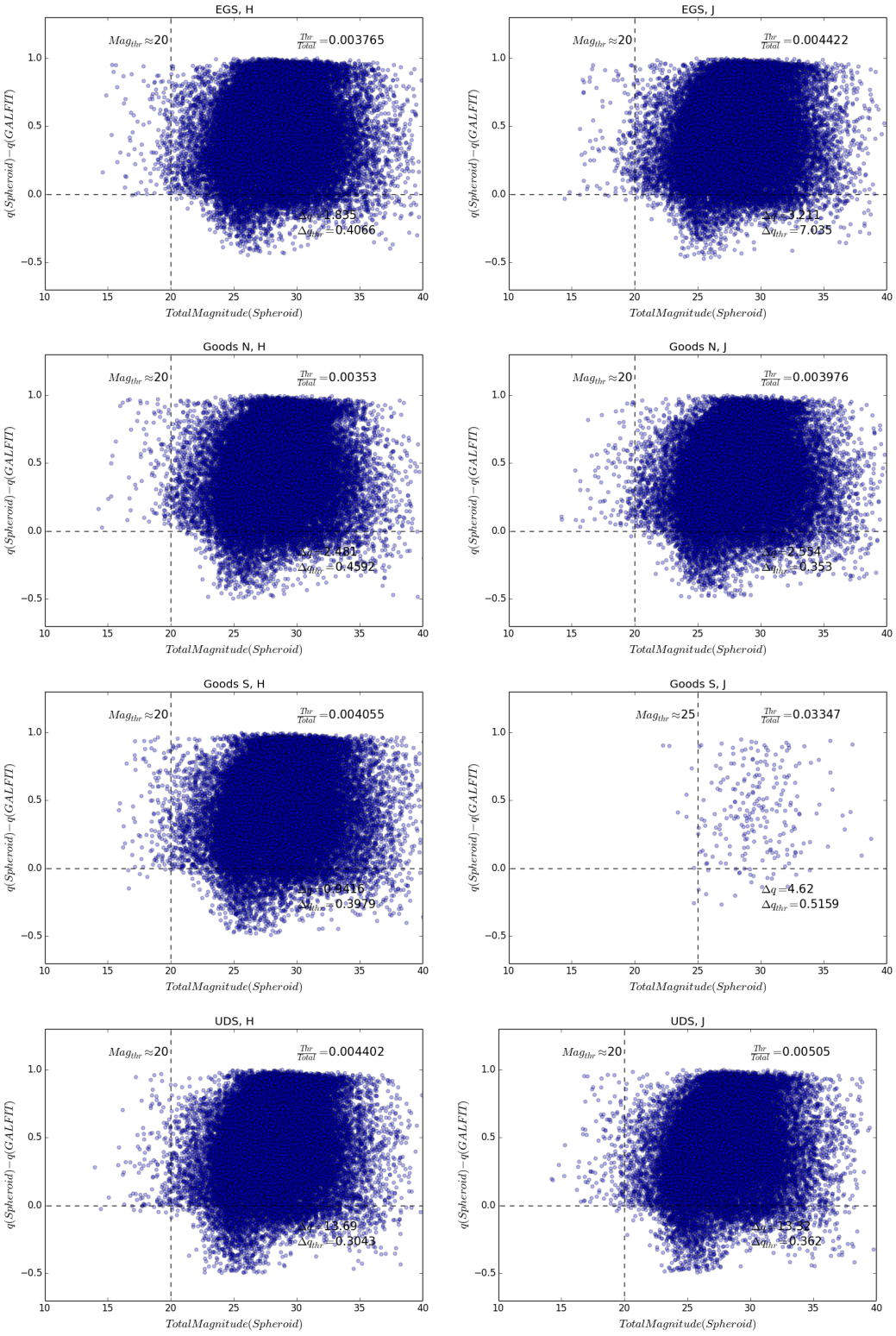
EGS, H
$Mag_{thr} \approx 20$
$\frac{Thr}{Total} = 0.003765$
$\Delta q = 1.835$
$\Delta q_{thr} = 0.4066$
EGS, J
$Mag_{thr} \approx 20$
$\frac{Thr}{Total} = 0.004422$
$\Delta q = 7.211$
$\Delta q_{thr} = 7.035$
Goods N, H
$Mag_{thr} \approx 20$
$\frac{Thr}{Total} = 0.00353$
$\Delta q = 2.481$
$\Delta q_{thr} = 0.4592$
Goods N, J
$Mag_{thr} \approx 20$
$\frac{Thr}{Total} = 0.003976$
$\Delta q = 2.554$
$\Delta q_{thr} = 0.353$
Goods S, H
$Mag_{thr} \approx 20$
$\frac{Thr}{Total} = 0.004055$
$\Delta q = 0.9416$
$\Delta q_{thr} = 0.3979$
Goods S, J
$Mag_{thr} \approx 25$
$\frac{Thr}{Total} = 0.03347$
$\Delta q = 4.62$
$\Delta q_{thr} = 0.5159$
UDS, H
$Mag_{thr} \approx 20$
$\frac{Thr}{Total} = 0.004402$
$\Delta q = 13.69$
$\Delta q_{thr} = 0.3043$
UDS, J
$Mag_{thr} \approx 20$
$\frac{Thr}{Total} = 0.00505$
$\Delta q = 13.32$
$\Delta q_{thr} = 0.362$
$q(Spheroid) - q(GALFIT)$
$TotalMagnitude(Spheroid)$

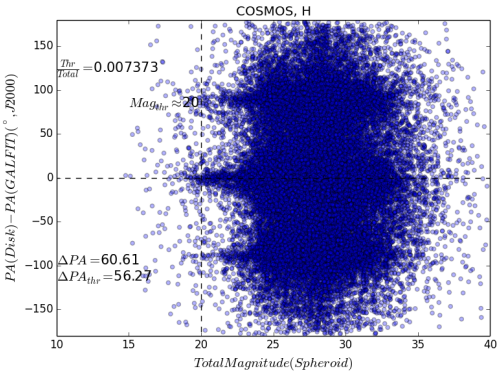
COSMOS, H
$\frac{Thr}{Total}$ =0.007373
$Mag_{thr} \approx 20$
ΔPA =60.61
ΔPA_{thr} =56.27
$PA(Disk) - PA(GALFIT)(^\circ, J2000)$
$TotalMagnitude(Spheroid)$

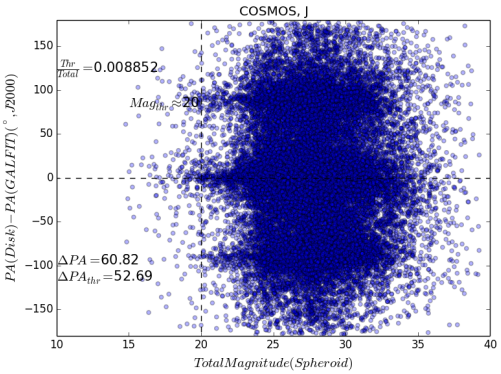
COSMOS, J
$\frac{Thr}{Total}$ =0.008852
$Mag_{thr} \approx 20$
ΔPA =60.82
ΔPA_{thr} =52.69
$PA(Disk) - PA(GALFIT)(^\circ, J2000)$
$TotalMagnitude(Spheroid)$

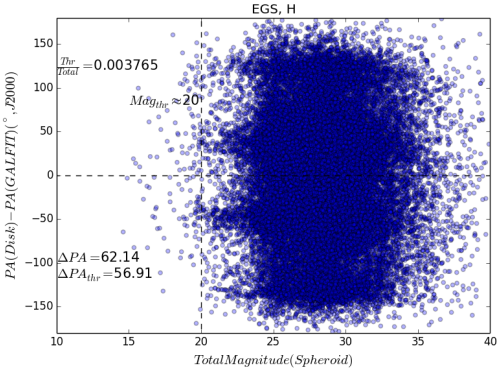
EGS, H
$\frac{Thr}{Total}$ =0.003765
$Mag_{thr} \approx 20$
ΔPA =62.14
ΔPA_{thr} =56.91
$PA(Disk) - PA(GALFIT)(^\circ, J2000)$
$TotalMagnitude(Spheroid)$

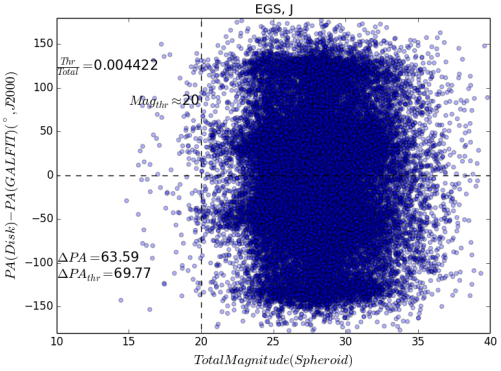
EGS, J
$\frac{Thr}{Total}$ =0.004422
$Mag_{thr} \approx 20$
ΔPA =63.59
ΔPA_{thr} =69.77
$PA(Disk) - PA(GALFIT)(^\circ, J2000)$
$TotalMagnitude(Spheroid)$

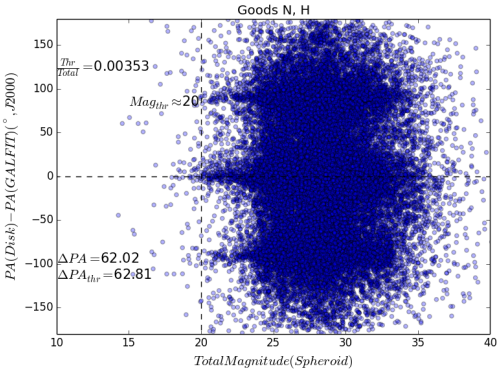
Goods N, H
$\frac{Thr}{Total}$ =0.00353
$Mag_{thr} \approx 20$
ΔPA =62.02
ΔPA_{thr} =62.81
$PA(Disk) - PA(GALFIT)(^\circ, J2000)$
$TotalMagnitude(Spheroid)$

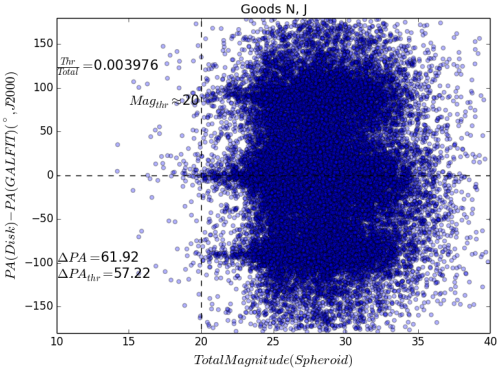
Goods N, J
$\frac{Thr}{Total}$ =0.003976
$Mag_{thr} \approx 20$
ΔPA =61.92
ΔPA_{thr} =57.22
$PA(Disk) - PA(GALFIT)(^\circ, J2000)$
$TotalMagnitude(Spheroid)$

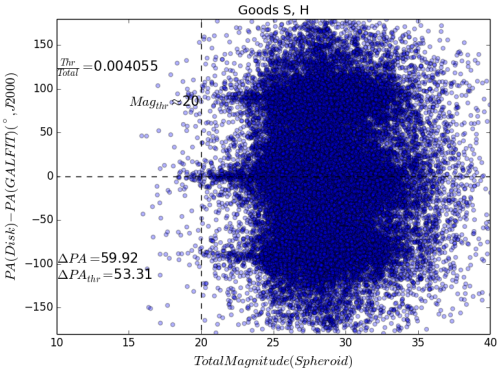
Goods S, H
$\frac{Thr}{Total}$ =0.004055
$Mag_{thr} \approx 20$
ΔPA =59.92
ΔPA_{thr} =53.31
$PA(Disk) - PA(GALFIT)(^\circ, J2000)$
$TotalMagnitude(Spheroid)$

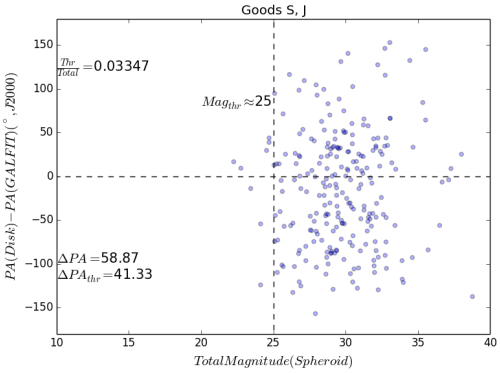
Goods S, J
$\frac{Thr}{Total}$ =0.03347
$Mag_{thr} \approx 25$
ΔPA =58.87
ΔPA_{thr} =41.33
$PA(Disk) - PA(GALFIT)(^\circ, J2000)$
$TotalMagnitude(Spheroid)$

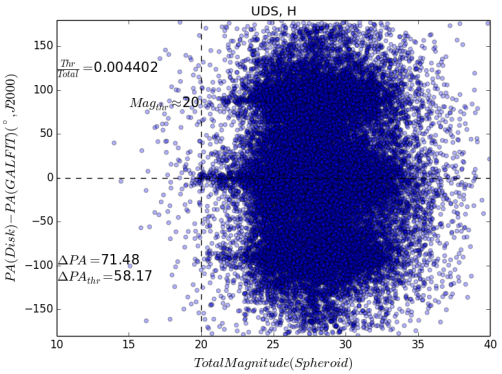
UDS, H
$\frac{Thr}{Total}$ =0.004402
$Mag_{thr} \approx 20$
ΔPA =71.48
ΔPA_{thr} =58.17
$PA(Disk) - PA(GALFIT)(^\circ, J2000)$
$TotalMagnitude(Spheroid)$

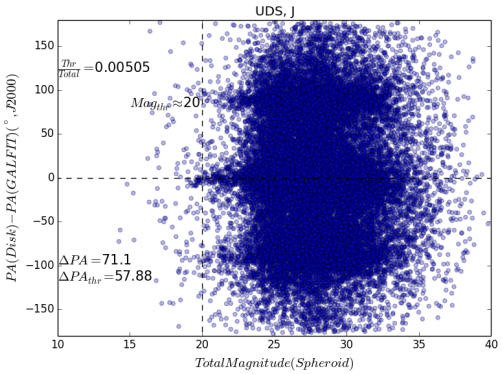
UDS, J
$\frac{Thr}{Total}$ =0.00505
$Mag_{thr} \approx 20$
ΔPA =71.1
ΔPA_{thr} =57.88
$PA(Disk) - PA(GALFIT)(^\circ, J2000)$
$TotalMagnitude(Spheroid)$

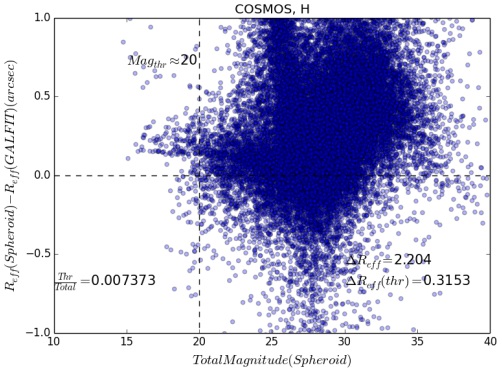
COSMOS, H
$Mag_{thr} \approx 20$
$\frac{Thr}{Total}$ =0.007373
ΔR_{eff} =2.204
$\Delta R_{eff}(thr)$ =0.3153
$R_{eff}(Spheroid) - R_{eff}(GALFIT)(arcsec)$
$TotalMagnitude(Spheroid)$

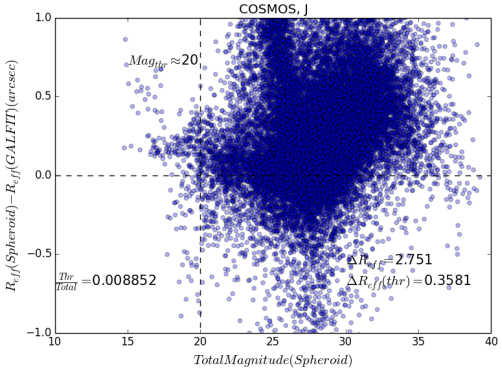
COSMOS, J
$Mag_{thr} \approx 20$
$\frac{Thr}{Total}$ =0.008852
ΔR_{eff} =2.751
$\Delta R_{eff}(thr)$ =0.3581
$R_{eff}(Spheroid) - R_{eff}(GALFIT)(arcsec)$
$TotalMagnitude(Spheroid)$

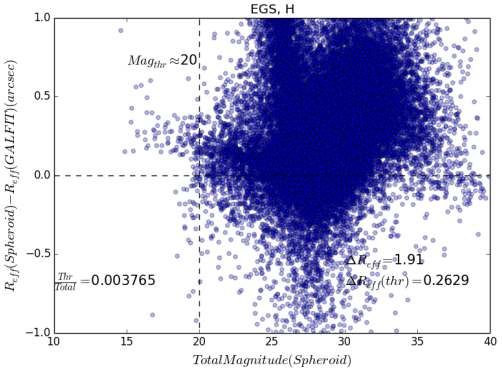
EGS, H
$Mag_{thr} \approx 20$
$\frac{Thr}{Total}$ =0.003765
ΔR_{eff} =1.91
$\Delta R_{eff}(thr)$ =0.2629
$R_{eff}(Spheroid) - R_{eff}(GALFIT)(arcsec)$
$TotalMagnitude(Spheroid)$

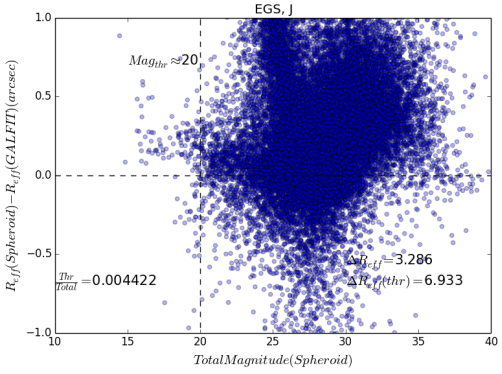
EGS, J
$Mag_{thr} \approx 20$
$\frac{Thr}{Total}$ =0.004422
ΔR_{eff} =3.286
$\Delta R_{eff}(thr)$ =6.933
$R_{eff}(Spheroid) - R_{eff}(GALFIT)(arcsec)$
$TotalMagnitude(Spheroid)$

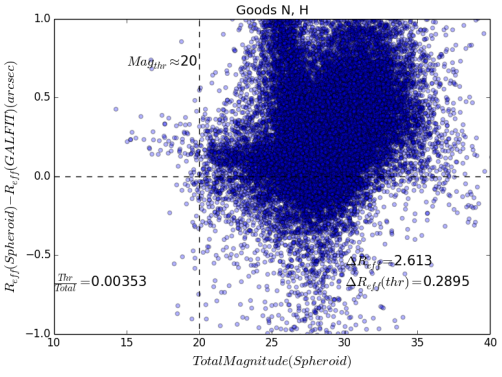
Goods N, H
$Mag_{thr} \approx 20$
$\frac{Thr}{Total}$ =0.00353
ΔR_{eff} =2.613
$\Delta R_{eff}(thr)$ =0.2895
$R_{eff}(Spheroid) - R_{eff}(GALFIT)(arcsec)$
$TotalMagnitude(Spheroid)$

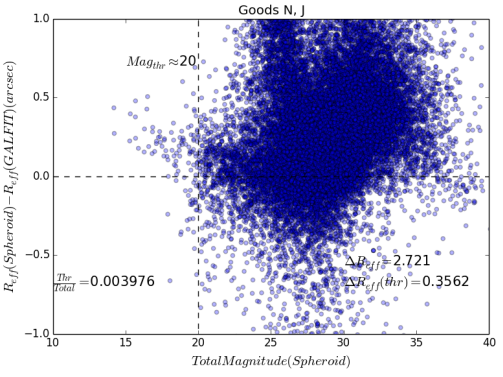
Goods N, J
$Mag_{thr} \approx 20$
$\frac{Thr}{Total}$ =0.003976
ΔR_{eff} =2.721
$\Delta R_{eff}(thr)$ =0.3562
$R_{eff}(Spheroid) - R_{eff}(GALFIT)(arcsec)$
$TotalMagnitude(Spheroid)$

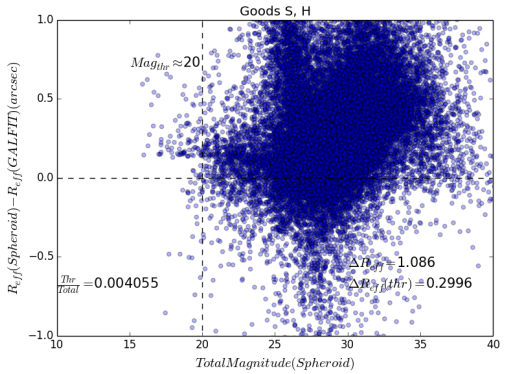
Goods S, H
$Mag_{thr} \approx 20$
ΔR_{eff}= 1.086
$\Delta R_{eff}(thr)$ =0.2996
$\frac{Thr}{Total}$ =0.004055
$R_{eff}(Spheroid) - R_{eff}(GALFIT)(arcsec)$
$TotalMagnitude(Spheroid)$

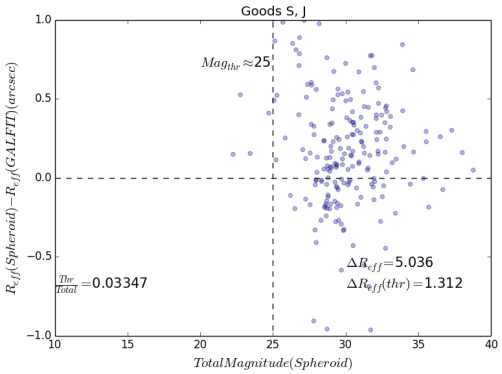
Goods S, J
$Mag_{thr} \approx 25$
ΔR_{eff}=5.036
$\Delta R_{eff}(thr)$ =1.312
$\frac{Thr}{Total}$ =0.03347
$R_{eff}(Spheroid) - R_{eff}(GALFIT)(arcsec)$
$TotalMagnitude(Spheroid)$

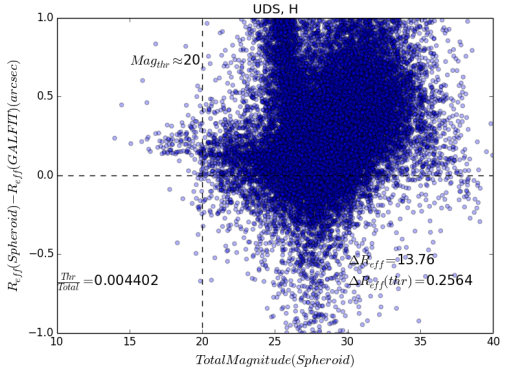
UDS, H
$Mag_{thr} \approx 20$
ΔR_{eff}= 13.76
$\Delta R_{eff}(thr)$ =0.2564
$\frac{Thr}{Total}$ =0.004402
$R_{eff}(Spheroid) - R_{eff}(GALFIT)(arcsec)$
$TotalMagnitude(Spheroid)$

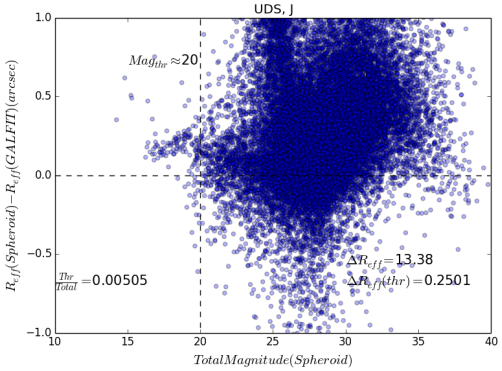
UDS, J
$Mag_{thr} \approx 20$
ΔR_{eff}=13.38
$\Delta R_{eff}(thr)$ =0.2501
$\frac{Thr}{Total}$ =0.00505
$R_{eff}(Spheroid) - R_{eff}(GALFIT)(arcsec)$
$TotalMagnitude(Spheroid)$

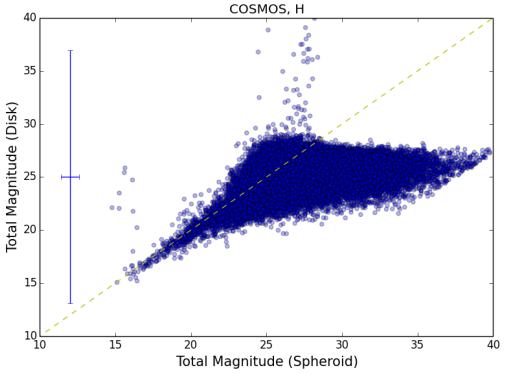
COSMOS, H
Total Magnitude (Disk)
Total Magnitude (Spheroid)

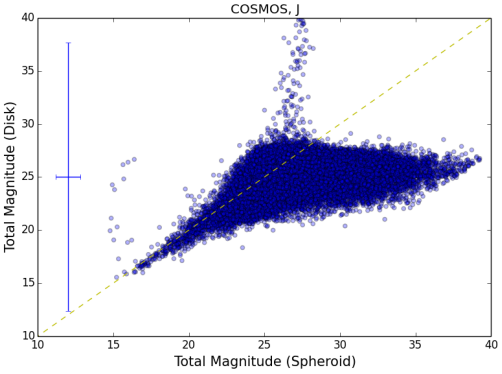
COSMOS, J
Total Magnitude (Disk)
Total Magnitude (Spheroid)

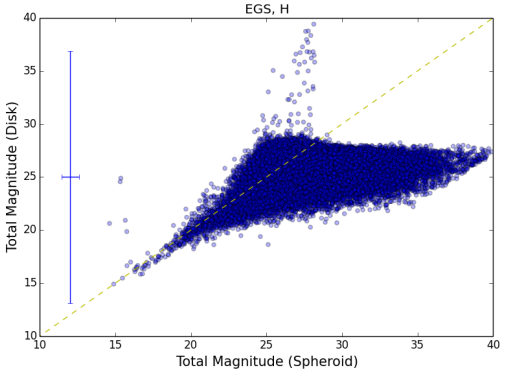
EGS, H
Total Magnitude (Disk)
Total Magnitude (Spheroid)

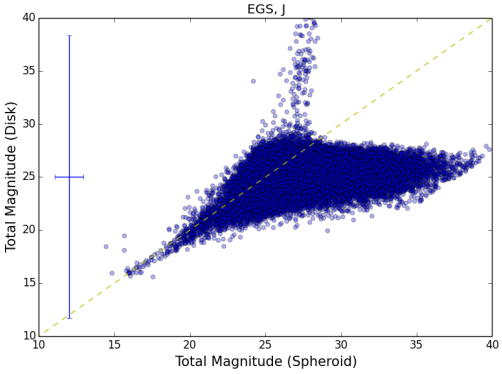
EGS, J
Total Magnitude (Disk)
Total Magnitude (Spheroid)

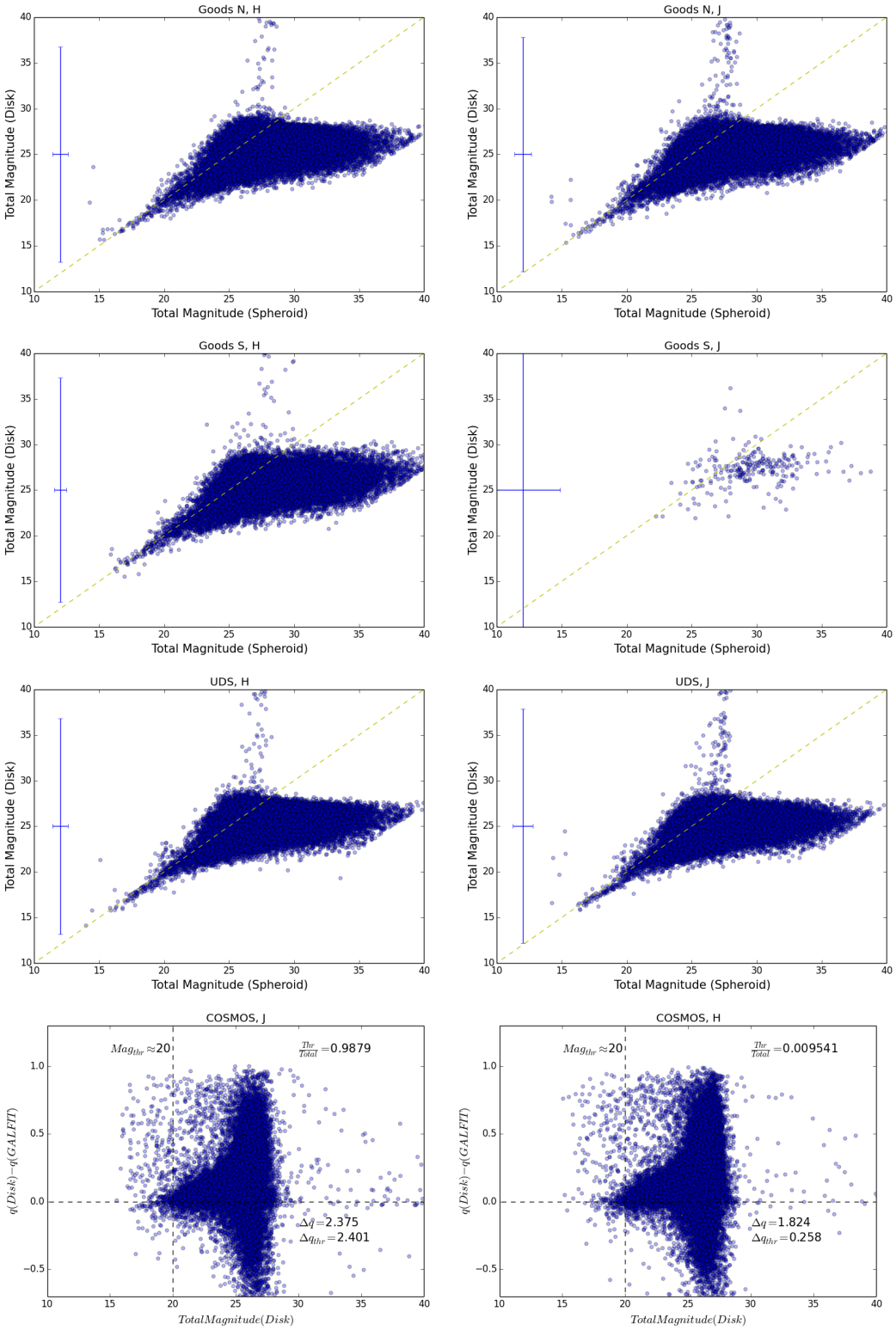
Goods N, H
Goods N, J
Goods S, H
Goods S, J
UDS, H
UDS, J
Total Magnitude (Disk)
Total Magnitude (Spheroid)
COSMOS, J
COSMOS, H
$Mag_{thr} \approx 20$
$\frac{Thr}{Total}$ =0.9879
$\frac{Thr}{Total}$ =0.009541
Δq=2.375
Δq_{thr}=2.401
Δq=1.824
Δq_{thr}=0.258
$q(Disk)-q(GALFIT)$
$TotalMagnitude(Disk)$

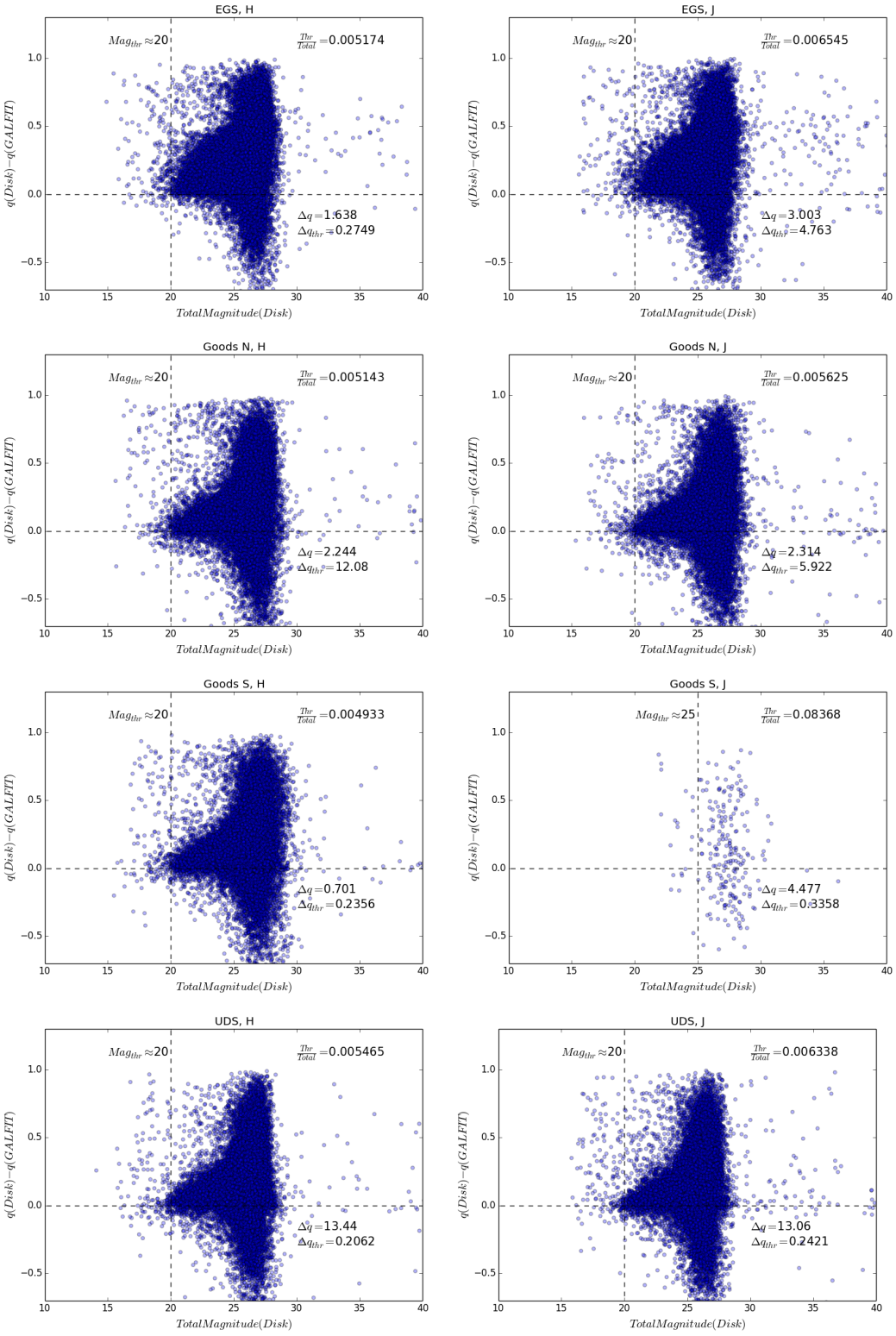
EGS, H
$Mag_{thr} \approx 20$
$\frac{Thr}{Total}$ =0.005174
Δq =1.638
Δq_{thr} =0.2749
EGS, J
$Mag_{thr} \approx 20$
$\frac{Thr}{Total}$ =0.006545
Δq =3.003
Δq_{thr} =4.763
Goods N, H
$Mag_{thr} \approx 20$
$\frac{Thr}{Total}$ =0.005143
Δq =2.244
Δq_{thr} =12.08
Goods N, J
$Mag_{thr} \approx 20$
$\frac{Thr}{Total}$ =0.005625
Δq =2.314
Δq_{thr} =5.922
Goods S, H
$Mag_{thr} \approx 20$
$\frac{Thr}{Total}$ =0.004933
Δq =0.701
Δq_{thr} =0.2356
Goods S, J
$Mag_{thr} \approx 25$
$\frac{Thr}{Total}$ =0.08368
Δq =4.477
Δq_{thr} =0.3358
UDS, H
$Mag_{thr} \approx 20$
$\frac{Thr}{Total}$ =0.005465
Δq =13.44
Δq_{thr} =0.2062
UDS, J
$Mag_{thr} \approx 20$
$\frac{Thr}{Total}$ =0.006338
Δq =13.06
Δq_{thr} =0.2421
$q(Disk) - q(GALFIT)$
$TotalMagnitude(Disk)$

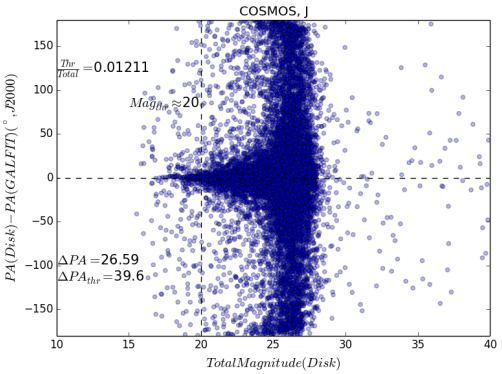
COSMOS, J
$\frac{Thr}{Total}$ =0.01211
$Mag_{thr} \approx 20$
ΔPA =26.59
ΔPA_{thr} =39.6
$PA(Disk) - PA(GALFIT)(^\circ, J2000)$
$TotalMagnitude(Disk)$

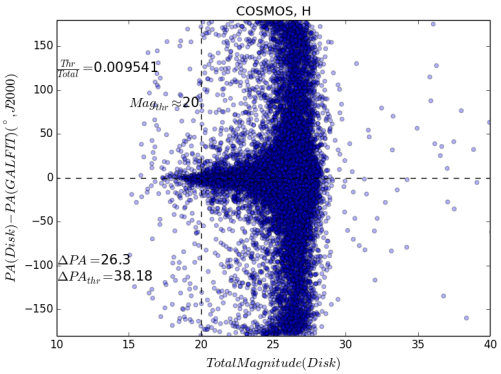
COSMOS, H
$\frac{Thr}{Total}$ =0.009541
$Mag_{thr} \approx 20$
ΔPA =26.3
ΔPA_{thr} =38.18
$PA(Disk) - PA(GALFIT)(^\circ, J2000)$
$TotalMagnitude(Disk)$

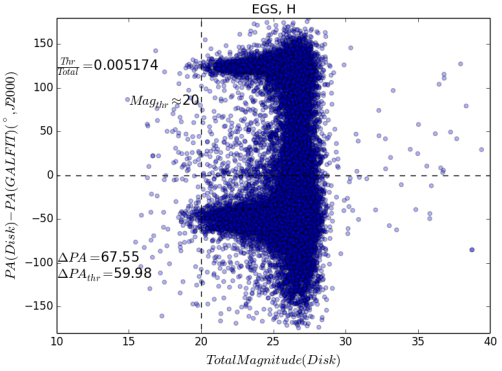
EGS, H
$\frac{Thr}{Total}$ =0.005174
$Mag_{thr} \approx 20$
ΔPA =67.55
ΔPA_{thr} =59.98
$PA(Disk) - PA(GALFIT)(^\circ, J2000)$
$TotalMagnitude(Disk)$

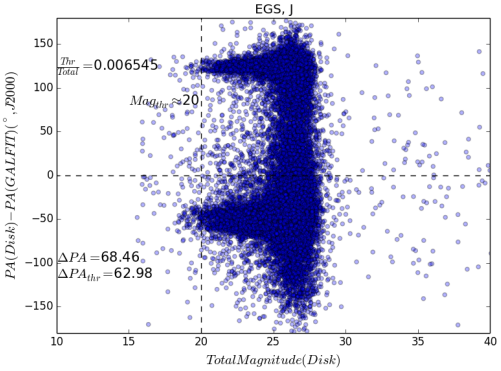
EGS, J
$\frac{Thr}{Total}$ =0.006545
$Mag_{thr} \approx 20$
ΔPA =68.46
ΔPA_{thr} =62.98
$PA(Disk) - PA(GALFIT)(^\circ, J2000)$
$TotalMagnitude(Disk)$

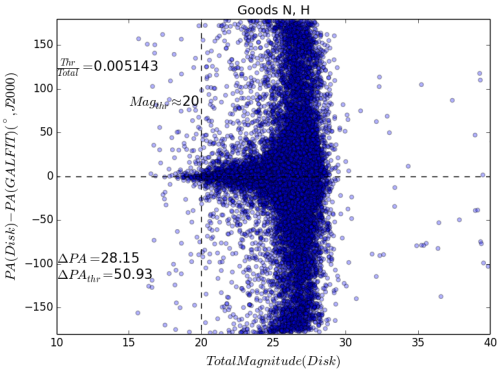
Goods N, H
$\frac{Thr}{Total}$ =0.005143
$Mag_{thr} \approx 20$
ΔPA =28.15
ΔPA_{thr} =50.93
$PA(Disk) - PA(GALFIT)(^\circ, J2000)$
$TotalMagnitude(Disk)$

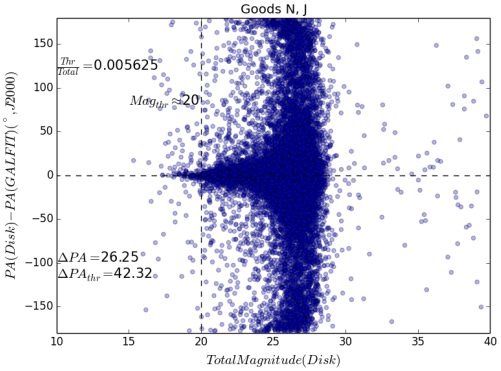
Goods N, J
$\frac{Thr}{Total}$ =0.005625
$Mag_{thr} \approx 20$
ΔPA =26.25
ΔPA_{thr} =42.32
$PA(Disk) - PA(GALFIT)(^\circ, J2000)$
$TotalMagnitude(Disk)$

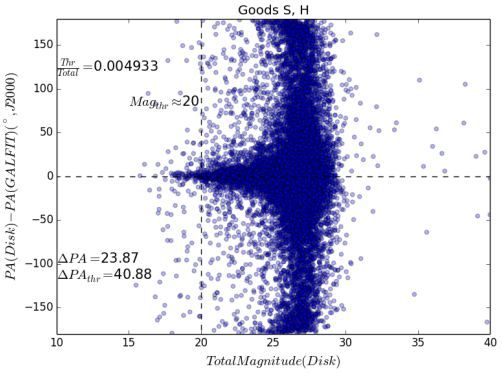
Goods S, H
$\frac{Thr}{Total}$ =0.004933
$Mag_{thr} \approx 20$
ΔPA =23.87
ΔPA_{thr} =40.88
$PA(Disk) - PA(GALFIT)(^\circ, J2000)$
$TotalMagnitude(Disk)$

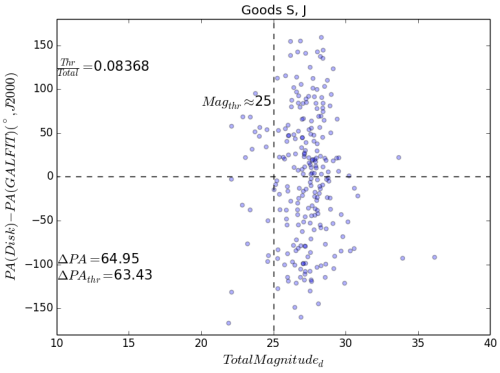
Goods S, J
$\frac{Thr}{Total}$ =0.08368
$Mag_{thr} \approx 25$
ΔPA =64.95
ΔPA_{thr} =63.43
$PA(Disk) - PA(GALFIT)(^\circ, J2000)$
$TotalMagnitude_d$

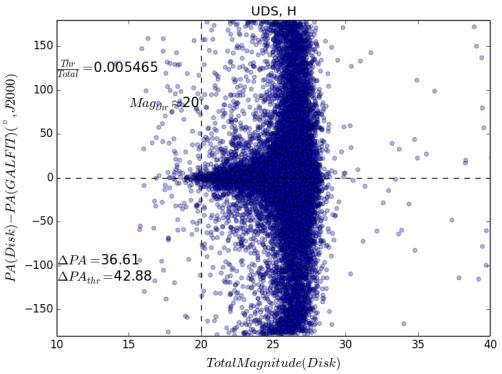
UDS, H
$\frac{Thr}{Total}$=0.005465
$Mag_{thr} \approx 20$
ΔPA=36.61
ΔPA_{thr}=42.88
$PA(Disk) - PA(GALFIT)(^\circ, J2000)$
$TotalMagnitude(Disk)$

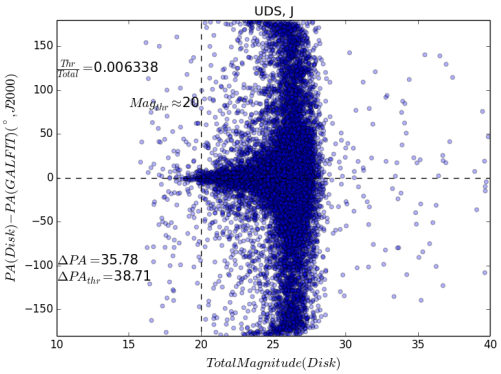
UDS, J
$\frac{Thr}{Total}$=0.006338
$Mag_{thr} \approx 20$
ΔPA=35.78
ΔPA_{thr}=38.71
$PA(Disk) - PA(GALFIT)(^\circ, J2000)$
$TotalMagnitude(Disk)$

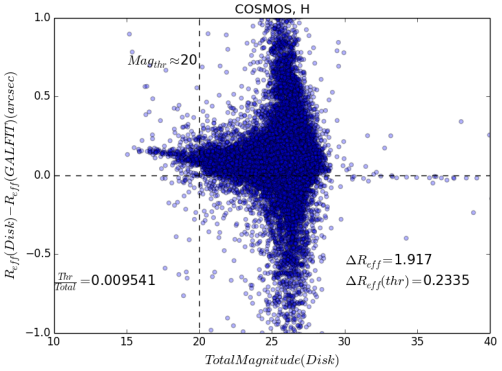
COSMOS, H
$Mag_{thr} \approx 20$
$\frac{Thr}{Total}$=0.009541
ΔR_{eff}=1.917
$\Delta R_{eff}(thr)$=0.2335
$R_{eff}(Disk) - R_{eff}(GALFIT)(arcsec)$
$TotalMagnitude(Disk)$

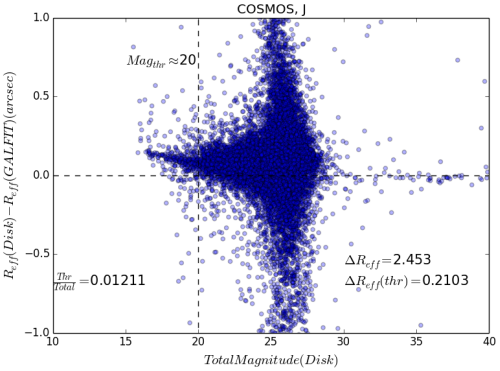
COSMOS, J
$Mag_{thr} \approx 20$
$\frac{Thr}{Total}$=0.01211
ΔR_{eff}=2.453
$\Delta R_{eff}(thr)$=0.2103
$R_{eff}(Disk) - R_{eff}(GALFIT)(arcsec)$
$TotalMagnitude(Disk)$

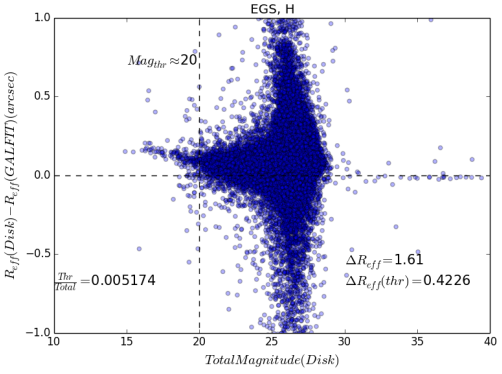
EGS, H
$Mag_{thr} \approx 20$
$\frac{Thr}{Total}$=0.005174
ΔR_{eff}=1.61
$\Delta R_{eff}(thr)$=0.4226
$R_{eff}(Disk) - R_{eff}(GALFIT)(arcsec)$
$TotalMagnitude(Disk)$

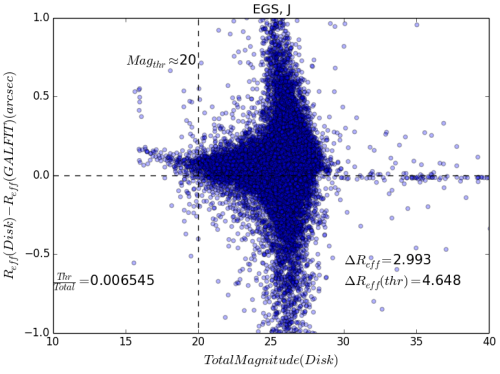
EGS, J
$Mag_{thr} \approx 20$
$\frac{Thr}{Total}$=0.006545
ΔR_{eff}=2.993
$\Delta R_{eff}(thr)$=4.648
$R_{eff}(Disk) - R_{eff}(GALFIT)(arcsec)$
$TotalMagnitude(Disk)$

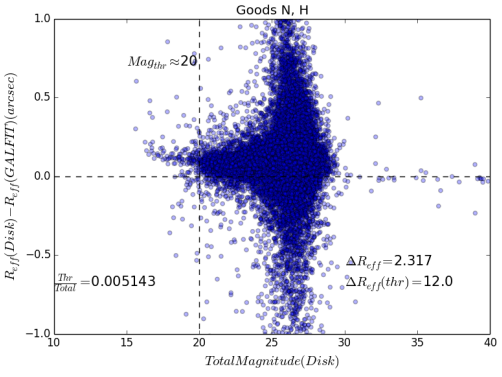
Goods N, H
$Mag_{thr} \approx 20$
$\frac{Thr}{Total}$=0.005143
ΔR_{eff}=2.317
$\Delta R_{eff}(thr)$=12.0
$R_{eff}(Disk) - R_{eff}(GALFIT)(arcsec)$
$TotalMagnitude(Disk)$

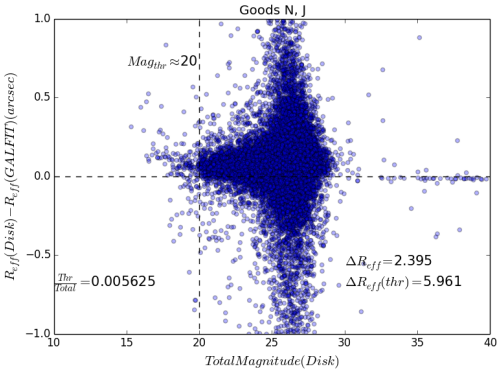
Goods N, J
$Mag_{thr} \approx 20$
$\frac{Thr}{Total}$=0.005625
ΔR_{eff}=2.395
$\Delta R_{eff}(thr)$=5.961
$R_{eff}(Disk) - R_{eff}(GALFIT)(arcsec)$
$TotalMagnitude(Disk)$

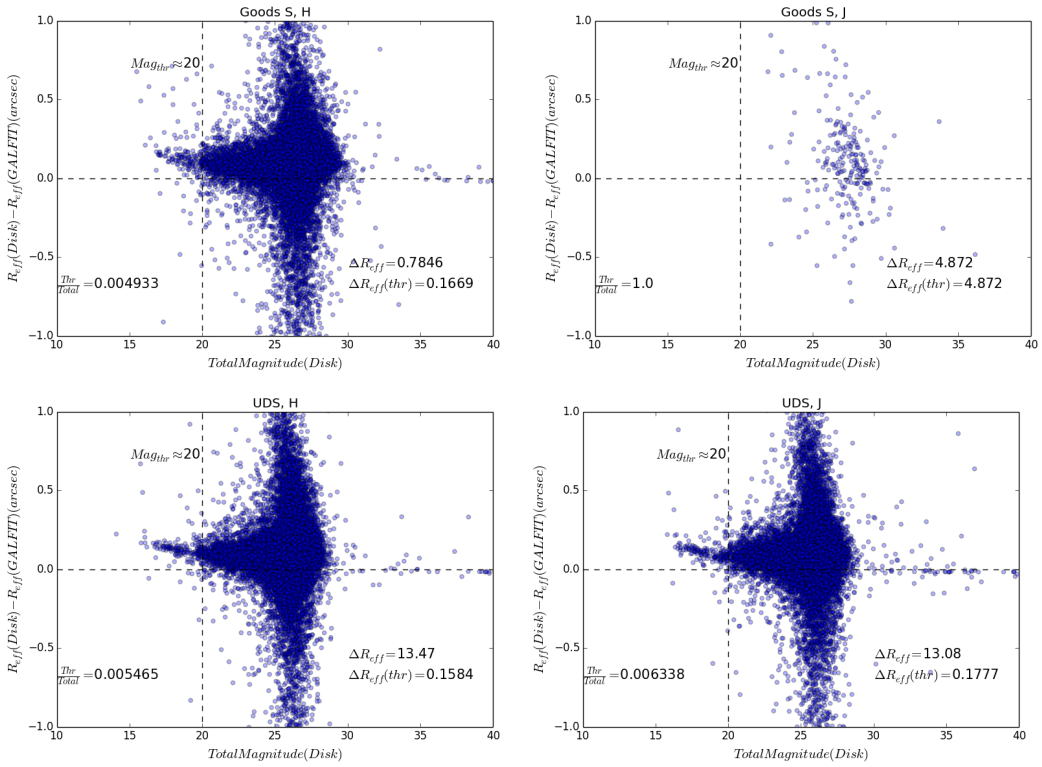
Goods S, H
$Mag_{thr} \approx 20$
$\frac{Thr}{Total}$=0.004933
ΔR_{eff}=0.7846
$\Delta R_{eff}(thr)$=0.1669
$R_{eff}(Disk) - R_{eff}(GALFIT)(arcsec)$
$TotalMagnitude(Disk)$
Goods S, J
$Mag_{thr} \approx 20$
$\frac{Thr}{Total}$=1.0
ΔR_{eff}=4.872
$\Delta R_{eff}(thr)$=4.872
$R_{eff}(Disk) - R_{eff}(GALFIT)(arcsec)$
$TotalMagnitude(Disk)$
UDS, H
$Mag_{thr} \approx 20$
$\frac{Thr}{Total}$=0.005465
ΔR_{eff}=13.47
$\Delta R_{eff}(thr)$=0.1584
$R_{eff}(Disk) - R_{eff}(GALFIT)(arcsec)$
$TotalMagnitude(Disk)$
UDS, J
$Mag_{thr} \approx 20$
$\frac{Thr}{Total}$=0.006338
ΔR_{eff}=13.08
$\Delta R_{eff}(thr)$=0.1777
$R_{eff}(Disk) - R_{eff}(GALFIT)(arcsec)$
$TotalMagnitude(Disk)$

6.2 Part B: Scale-Invariant Morphology Graphs

Part B: The graphs presented here are all associated with the scale-invariant morphological research performed. Each graph mainly deals with comparisons between two values og the given: Gini (G), asymmetry (A), photometric redshift ($z_{photo} = z$), effective, or half-light, radius ($R_{eff} = R_{50}$), and IRAC color from *Spitzer* ($[3.6] - [4.5]$). Some graphs have unique characteristics, which will be accompanied with a caption to describe the unique characteristic.

References

[Bertin and Arnouts, 1996] Bertin, E. and Arnouts, S. (1996). SExtractor: Software for source extraction. , 117:393–404.

[Bouwens et al., 2004] Bouwens, R. J., Illingworth, G. D., Blakeslee, J. P., Broadhurst, T. J., and Franx, M. (2004). Galaxy Size Evolution at High Redshift and Surface Brightness Selection Effects: Constraints from the Hubble Ultra Deep Field. , 611:L1–L4.

[Bouwens et al., 2006] Bouwens, R. J., Illingworth, G. D., Blakeslee, J. P., and Franx, M. (2006). Galaxies at z ˜ 6: The UV Luminosity Function and Luminosity Density from 506 HUDF, HUDF Parallel ACS Field, and GOODS i-Dropouts. , 653:53–85.

[Bouwens et al., 2011a] Bouwens, R. J., Illingworth, G. D., Labbe, I., Oesch, P. A., Trenti, M., Carollo, C. M., van Dokkum, P. G., Franx, M., Stiavelli, M., González, V., Magee, D., and Bradley, L. (2011a). A candidate redshift z˜10 galaxy and rapid changes in that population at an age of 500Myr. , 469:504–507.

[Bouwens et al., 2011b] Bouwens, R. J., Illingworth, G. D., Oesch, P. A., Labbé, I., Trenti, M., van Dokkum, P., Franx, M., Stiavelli, M., Carollo, C. M., Magee, D., and Gonzalez, V. (2011b). Ultraviolet Luminosity Functions from 132 z ˜ 7 and z ˜ 8 Lyman-break Galaxies in the Ultra-deep HUDF09 and Wide-area Early Release Science WFC3/IR Observations. , 737:90.

[Bouwens et al., 2015] Bouwens, R. J., Illingworth, G. D., Oesch, P. A., Trenti, M., Labbé, I., Bradley, L., Carollo, M., van Dokkum, P. G., Gonzalez, V.,

Holwerda, B., Franx, M., Spitler, L., Smit, R., and Magee, D. (2015). UV Luminosity Functions at Redshifts z

4 to z

10: 10,000 Galaxies from HST Legacy Fields. , 803:34.

[Bouwens et al., 2013] Bouwens, R. J., Oesch, P. A., Illingworth, G. D., Labbé, I., van Dokkum, P. G., Brammer, G., Magee, D., Spitler, L. R., Franx, M., Smit, R., Trenti, M., Gonzalez, V., and Carollo, C. M. (2013). Photometric Constraints on the Redshift of z ˜ 10 Candidate UDFj-39546284 from Deeper WFC3/IR+ACS+IRAC Observations over the HUDF. , 765:L16.

[Bowler et al., 2018] Bowler, R. A. A., Bourne, N., Dunlop, J. S., McLure, R. M., and McLeod, D. J. (2018). Obscured star-formation in bright z ˜ 7 Lyman-break galaxies. *ArXiv e-prints*.

[Bowler et al., 2017] Bowler, R. A. A., Dunlop, J. S., McLure, R. J., and McLeod, D. J. (2017). Unveiling the nature of bright z 7 galaxies with the Hubble Space Telescope. , 466:3612–3635.

[Calvi et al., 2016] Calvi, V., Trenti, M., Stiavelli, M., Oesch, P., Bradley, L. D., Schmidt, K. B., Coe, D., Brammer, G., Bernard, S., Bouwens, R. J., Carrasco, D., Carollo, C. M., Holwerda, B. W., MacKenty, J. W., Mason, C. A., Shull, J. M., and Treu, T. (2016). Bright Galaxies at Hubbles Redshift Detection Frontier: Preliminary Results and Design from the Redshift z ˜ 9-10 BoRG Pure-Parallel HST Survey. , 817:120.

[Coe et al., 2013] Coe, D., Zitrin, A., Carrasco, M., Shu, X., Zheng, W., Postman, M., Bradley, L., Koekemoer, A., Bouwens, R., Broadhurst, T., Monna, A., Host, O., Moustakas, L. A., Ford, H., Moustakas, J., van der Wel, A.,

Donahue, M., Rodney, S. A., Benítez, N., Jouvel, S., Seitz, S., Kelson, D. D., and Rosati, P. (2013). CLASH: Three Strongly Lensed Images of a Candidate z 11 Galaxy. , 762:32.

[Conselice, 2003] Conselice, C. J. (2003). The Relationship between Stellar Light Distributions of Galaxies and Their Formation Histories. , 147:1–28.

[Curtis-Lake et al., 2016] Curtis-Lake, E., McLure, R. J., Dunlop, J. S., Rogers, A. B., Targett, T., Dekel, A., Ellis, R. S., Faber, S. M., Ferguson, H. C., Grogin, N. A., Kocevski, D. D., Koekemoer, A. M., Lai, K., Mármol-Queraltó, E., and Robertson, B. E. (2016). Non-parametric analysis of the rest-frame UV sizes and morphological disturbance amongst L_* galaxies at 4 z 8. , 457:440–464.

[Dressel, 2012] Dressel, L. (2012). *Wide Field Camera 3 Instrument Handbook for Cycle 21 v. 5.0*.

[Ellis et al., 2013] Ellis, R. S., McLure, R. J., Dunlop, J. S., Robertson, B. E., Ono, Y., Schenker, M. A., Koekemoer, A., Bowler, R. A. A., Ouchi, M., Rogers, A. B., Curtis-Lake, E., Schneider, E., Charlot, S., Stark, D. P., Furlanetto, S. R., and Cirasuolo, M. (2013). The Abundance of Star-forming Galaxies in the Redshift Range 8.5-12: New Results from the 2012 Hubble Ultra Deep Field Campaign. , 763:L7.

[Elmegreen, 1998] Elmegreen, D. M. (1998). *Galaxies and galactic structure*. Prentice Hall.

[Fall and Efstathiou, 1980] Fall, S. M. and Efstathiou, G. (1980). Formation and rotation of disc galaxies with haloes. , 193:189–206.

[Ferguson et al., 2004] Ferguson, H. C., Dickinson, M., Giavalisco, M., Kretchmer, C., Ravindranath, S., Idzi, R., Taylor, E., Conselice, C. J., Fall, S. M., Gardner, J. P., Livio, M., Madau, P., Moustakas, L. A., Papovich, C. M., Somerville, R. S., Spinrad, H., and Stern, D. (2004). The Size Evolution of High-Redshift Galaxies. , 600:L107–L110.

[Florian et al., 2015a] Florian, M. K., Gladders, M. D., Li, N., and Sharon, K. (2015a). The Gini Coefficient as a Tool for Image Family Idenitification in Strong Lensing Systems with Multiple Images. *ArXiv e-prints*.

[Florian et al., 2015b] Florian, M. K., Li, N., and Gladders, M. D. (2015b). The Gini Coefficient as a Morphological Measurement of Strongly Lensed Galaxies in the Image Plane. *ArXiv e-prints*.

[Grogin et al., 2011] Grogin, N. A., Kocevski, D. D., Faber, S. M., Ferguson, H. C., Koekemoer, A. M., Riess, A. G., Acquaviva, V., Alexander, D. M., Almaini, O., Ashby, M. L. N., Barden, M., Bell, E. F., Bournaud, F., Brown, T. M., Caputi, K. I., Casertano, S., Cassata, P., Castellano, M., Challis, P., Chary, R.-R., Cheung, E., Cirasuolo, M., Conselice, C. J., Roshan Cooray, A., Croton, D. J., Daddi, E., Dahlen, T., Davé, R., de Mello, D. F., Dekel, A., Dickinson, M., Dolch, T., Donley, J. L., Dunlop, J. S., Dutton, A. A., Elbaz, D., Fazio, G. G., Filippenko, A. V., Finkelstein, S. L., Fontana, A., Gardner, J. P., Garnavich, P. M., Gawiser, E., Giavalisco, M., Grazian, A., Guo, Y., Hathi, N. P., Häussler, B., Hopkins, P. F., Huang, J.-S., Huang, K.-H., Jha, S. W., Kartaltepe, J. S., Kirshner, R. P., Koo, D. C., Lai, K., Lee, K.-S., Li, W., Lotz, J. M., Lucas, R. A., Madau, P., McCarthy, P. J., McGrath, E. J., McIntosh, D. H., McLure, R. J., Mobasher, B., Moustakas, L. A., Mozena, M., Nandra, K., Newman, J. A., Niemi, S.-M., Noeske,

K. G., Papovich, C. J., Pentericci, L., Pope, A., Primack, J. R., Rajan, A., Ravindranath, S., Reddy, N. A., Renzini, A., Rix, H.-W., Robaina, A. R., Rodney, S. A., Rosario, D. J., Rosati, P., Salimbeni, S., Scarlata, C., Siana, B., Simard, L., Smidt, J., Somerville, R. S., Spinrad, H., Straughn, A. N., Strolger, L.-G., Telford, O., Teplitz, H. I., Trump, J. R., van der Wel, A., Villforth, C., Wechsler, R. H., Weiner, B. J., Wiklind, T., Wild, V., Wilson, G., Wuyts, S., Yan, H.-J., and Yun, M. S. (2011). CANDELS: The Cosmic Assembly Near-infrared Deep Extragalactic Legacy Survey. , 197:35.

[Hathi et al., 2008] Hathi, N. P., Jansen, R. A., Windhorst, R. A., Cohen, S. H., Keel, W. C., Corbin, M. R., and Ryan, Jr., R. E. (2008). Surface Brightness Profiles of Composite Images of Compact Galaxies at z 4-6 in the Hubble Ultra Deep Field. , 135:156–166.

[Holwerda et al., 2018] Holwerda, B. W., Bridge, J. S., Ryan, R., Kenworthy, M. A., Pirzkal, N., Andersen, M., Wilkins, S., Smit, R., Bernard, S. R., Meshkat, T., Steele, R., and Bouwens, R. C. (2018). Substellar and low-mass dwarf identification with near-infrared imaging space observatories. *ArXiv e-prints*.

[Holwerda et al., 2014a] Holwerda, B. W., Muñoz-Mateos, J.-C., Comerón, S., Meidt, S., Sheth, K., Laine, S., Hinz, J. L., Regan, M. W., Gil de Paz, A., Menéndez-Delmestre, K., Seibert, M., Kim, T., Mizusawa, T., Laurikainen, E., Salo, H., Laine, J., Gadotti, D. A., Zaritsky, D., Erroz-Ferrer, S., Ho, L. C., Knapen, J. H., Athanassoula, E., Bosma, A., and Pirzkal, N. (2014a). Morphological Parameters of a Spitzer Survey of Stellar Structure in Galaxies. , 781:12.

[Holwerda et al., 2014b] Holwerda, B. W., Trenti, M., Clarkson, W., Sahu, K., Bradley, L., Stiavelli, M., Pirzkal, N., De Marchi, G., Andersen, M., Bouwens, R., and Ryan, R. (2014b). Milky Way Red Dwarfs in the BoRG Survey; Galactic Scale-height and the Distribution of Dwarf Stars in WFC3 Imaging. , 788:77.

[Hunter, 2007] Hunter, J. D. (2007). Matplotlib: A 2d graphics environment. *Computing In Science & Engineering*, 9(3):90–95.

[Jones et al., 01] Jones, E., Oliphant, T., Peterson, P., et al. (2001–). SciPy: Open source scientific tools for Python. [Online; accessed ¡today¿].

[Koekemoer et al., 2011] Koekemoer, A. M., Faber, S. M., Ferguson, H. C., Grogin, N. A., Kocevski, D. D., Koo, D. C., Lai, K., Lotz, J. M., Lucas, R. A., McGrath, E. J., Ogaz, S., Rajan, A., Riess, A. G., Rodney, S. A., Strolger, L., Casertano, S., Castellano, M., Dahlen, T., Dickinson, M., Dolch, T., Fontana, A., Giavalisco, M., Grazian, A., Guo, Y., Hathi, N. P., Huang, K.-H., van der Wel, A., Yan, H.-J., Acquaviva, V., Alexander, D. M., Almaini, O., Ashby, M. L. N., Barden, M., Bell, E. F., Bournaud, F., Brown, T. M., Caputi, K. I., Cassata, P., Challis, P. J., Chary, R.-R., Cheung, E., Cirasuolo, M., Conselice, C. J., Roshan Cooray, A., Croton, D. J., Daddi, E., Davé, R., de Mello, D. F., de Ravel, L., Dekel, A., Donley, J. L., Dunlop, J. S., Dutton, A. A., Elbaz, D., Fazio, G. G., Filippenko, A. V., Finkelstein, S. L., Frazer, C., Gardner, J. P., Garnavich, P. M., Gawiser, E., Gruetzbauch, R., Hartley, W. G., Häussler, B., Herrington, J., Hopkins, P. F., Huang, J.-S., Jha, S. W., Johnson, A., Kartaltepe, J. S., Khostovan, A. A., Kirshner, R. P., Lani, C., Lee, K.-S., Li, W., Madau, P., McCarthy, P. J., McIntosh, D. H., McLure, R. J., McPartland, C., Mobasher, B., Mor-

eira, H., Mortlock, A., Moustakas, L. A., Mozena, M., Nandra, K., Newman, J. A., Nielsen, J. L., Niemi, S., Noeske, K. G., Papovich, C. J., Pentericci, L., Pope, A., Primack, J. R., Ravindranath, S., Reddy, N. A., Renzini, A., Rix, H.-W., Robaina, A. R., Rosario, D. J., Rosati, P., Salimbeni, S., Scarlata, C., Siana, B., Simard, L., Smidt, J., Snyder, D., Somerville, R. S., Spinrad, H., Straughn, A. N., Telford, O., Teplitz, H. I., Trump, J. R., Vargas, C., Villforth, C., Wagner, C. R., Wandro, P., Wechsler, R. H., Weiner, B. J., Wiklind, T., Wild, V., Wilson, G., Wuyts, S., and Yun, M. S. (2011). CANDELS: The Cosmic Assembly Near-infrared Deep Extragalactic Legacy Survey—The Hubble Space Telescope Observations, Imaging Data Products, and Mosaics. *The Astrophysical Journal Supplement Series*, 197:36.

[Lisker, 2008] Lisker, T. (2008). Is the Gini Coefficient a Stable Measure of Galaxy Structure? , 179:319–325.

[Lotz et al., 2010] Lotz, J. M., Jonsson, P., Cox, T. J., and Primack, J. R. (2010). The effect of mass ratio on the morphology and time-scales of disc galaxy mergers. , 404:575–589.

[Lotz et al., 2004] Lotz, J. M., Primack, J., and Madau, P. (2004). A New Nonparametric Approach to Galaxy Morphological Classification. , 128:163–182.

[Lourakis et al., 2004] Lourakis, M. I. A., Lourakis, M. I. A., Argyros, A. A., and Argyros, A. A. (2004). The design and implementation of a generic sparse bundle adjustment software package based on the levenberg-marquardt algorithm. Technical report.

[Mo et al., 1998] Mo, H. J., Mao, S., and White, S. D. M. (1998). The formation of galactic discs. , 295:319–336.

[Oesch et al., 2010] Oesch, P. A., Bouwens, R. J., Illingworth, G. D., Carollo, C. M., Franx, M., Labbé, I., Magee, D., Stiavelli, M., Trenti, M., and van Dokkum, P. G. (2010). z ˜ 7 Galaxies in the HUDF: First Epoch WFC3/IR Results. , 709:L16–L20.

[Oesch et al., 2013] Oesch, P. A., Bouwens, R. J., Illingworth, G. D., Labbé, I., Franx, M., van Dokkum, P. G., Trenti, M., Stiavelli, M., Gonzalez, V., and Magee, D. (2013). Probing the Dawn of Galaxies at z ˜ 9-12: New Constraints from HUDF12/XDF and CANDELS data. , 773:75.

[Oesch et al., 2014] Oesch, P. A., Bouwens, R. J., Illingworth, G. D., Labbé, I., Smit, R., Franx, M., van Dokkum, P. G., Momcheva, I., Ashby, M. L. N., Fazio, G. G., Huang, J.-S., Willner, S. P., Gonzalez, V., Magee, D., Trenti, M., Brammer, G. B., Skelton, R. E., and Spitler, L. R. (2014). The Most Luminous z ˜ 9-10 Galaxy Candidates Yet Found: The Luminosity Function, Cosmic Star-formation Rate, and the First Mass Density Estimate at 500Myr. , 786:108.

[Oesch et al., 2015] Oesch, P. A., van Dokkum, P. G., Illingworth, G. D., Bouwens, R. J., Momcheva, I., Holden, B., Roberts-Borsani, G. W., Smit, R., Franx, M., Labbé, I., González, V., and Magee, D. (2015). A Spectroscopic Redshift Measurement for a Luminous Lyman Break Galaxy at z = 7.730 Using Keck/MOSFIRE. , 804:L30.

[Ono et al., 2013] Ono, Y., Ouchi, M., Curtis-Lake, E., Schenker, M. A., Ellis, R. S., McLure, R. J., Dunlop, J. S., Robertson, B. E., Koekemoer, A. M., Bowler, R. A. A., Rogers, A. B., Schneider, E., Charlot, S., Stark, D. P., Shimasaku, K., Furlanetto, S. R., and Cirasuolo, M. (2013). Evolution of

the Sizes of Galaxies over 7 z 12 Revealed by the 2012 Hubble Ultra Deep Field Campaign. , 777:155.

[Roberts-Borsani et al., 2016a] Roberts-Borsani, G. W., Bouwens, R. J., Oesch, P. A., Labbe, I., Smit, R., Illingworth, G. D., van Dokkum, P., Holden, B., Gonzalez, V., Stefanon, M., Holwerda, B., and Wilkins, S. (2016a). z 7 Galaxies with Red Spitzer/IRAC [3.6]-[4.5] Colors in the Full CANDELS Data Set: The Brightest-Known Galaxies at z ˜ 7-9 and a Probable Spectroscopic Confirmation at z = 7.48. , 823:143.

[Roberts-Borsani et al., 2016b] Roberts-Borsani, G. W., Bouwens, R. J., Oesch, P. A., Labbe, I., Smit, R., Illingworth, G. D., van Dokkum, P., Holden, B., Gonzalez, V., Stefanon, M., Holwerda, B., and Wilkins, S. (2016b). Z 7 galaxies with red spitzer/irac [3.6]-[4.5] colors in the full candels data set: the brightest-known galaxies at z $\tilde{7}$-9 and a probable spectroscopic confirmation at z=7.48. , 823:143.

[Ryan et al., 2011] Ryan, R. E., Thorman, P. A., Yan, H., Fan, X., Yan, L., Mechtley, M. R., Hathi, N. P., Cohen, S. H., Windhorst, R. A., McCarthy, P. J., and Wittman, D. M. (2011). Hubble Space Telescope Observations of Field Ultracool Dwarfs at High Galactic Latitude. , 739:83.

[Ryan et al., 2017] Ryan, Jr., R. E., Thorman, P. A., Schmidt, S. J., Cohen, S. H., Hathi, N. P., Holwerda, B. W., Lunine, J. I., Pirzkal, N., Windhorst, R. A., and Young, E. (2017). The Effect of Atmospheric Cooling on Vertical Velocity Dispersion and Density Distribution of Brown Dwarfs. , 847:53.

[Ryden and Peterson, 2011] Ryden, B. and Peterson, B. M. (2011). *Foundations of astrophysics*. Addison-Wesley, 10 edition.

[Sandage, 2005] Sandage, A. (2005). The Classification of Galaxies: Early History and Ongoing Developments. , 43:581–624.

[Sérsic, 1968] Sérsic, J. L. (1968). *Atlas de Galaxias Australes*.

[Shibuya et al., 2015] Shibuya, T., Ouchi, M., and Harikane, Y. (2015). Morphologies of $\sim 190,000 Galaxies at z = 010 Revealed with HST Legacy Data. I. Size Evolution.$, 219 : 15.

[Shibuya et al., 2018] Shibuya, T., Ouchi, M., Harikane, Y., and Nakajima, K. (2018). Morphologies of ˜190,000 Galaxies at z=0-10 Revealed with HST Legacy Data. III. Continuum Profile and Size Evolution of Lya Emitters. *ArXiv e-prints*.

[Stark et al., 2017] Stark, D. P., Ellis, R. S., Charlot, S., Chevallard, J., Tang, M., Belli, S., Zitrin, A., Mainali, R., Gutkin, J., Vidal-García, A., Bouwens, R., and Oesch, P. (2017). Lyα and C III] emission in z = 7-9 Galaxies: accelerated reionization around luminous star-forming systems? , 464:469–479.

[The Astropy Collaboration et al., 2018] The Astropy Collaboration, Price-Whelan, A. M., Sipőcz, B. M., Günther, H. M., Lim, P. L., Crawford, S. M., Conseil, S., Shupe, D. L., Craig, M. W., Dencheva, N., Ginsburg, A., VanderPlas, J. T., Bradley, L. D., Pérez-Suárez, D., de Val-Borro, M., Aldcroft, T. L., Cruz, K. L., Robitaille, T. P., Tollerud, E. J., Ardelean, C., Babej, T., Bachetti, M., Bakanov, A. V., Bamford, S. P., Barentsen, G., Barmby, P., Baumbach, A., Berry, K. L., Biscani, F., Boquien, M., Bostroem, K. A., Bouma, L. G., Brammer, G. B., Bray, E. M., Breytenbach, H., Buddelmeijer, H., Burke, D. J., Calderone, G., Cano Rodríguez,

J. L., Cara, M., Cardoso, J. V. M., Cheedella, S., Copin, Y., Crichton, D., DÁvella, D., Deil, C., Depagne, É., Dietrich, J. P., Donath, A., Droettboom, M., Earl, N., Erben, T., Fabbro, S., Ferreira, L. A., Finethy, T., Fox, R. T., Garrison, L. H., Gibbons, S. L. J., Goldstein, D. A., Gommers, R., Greco, J. P., Greenfield, P., Groener, A. M., Grollier, F., Hagen, A., Hirst, P., Homeier, D., Horton, A. J., Hosseinzadeh, G., Hu, L., Hunkeler, J. S., Ivezić, Ž., Jain, A., Jenness, T., Kanarek, G., Kendrew, S., Kern, N. S., Kerzendorf, W. E., Khvalko, A., King, J., Kirkby, D., Kulkarni, A. M., Kumar, A., Lee, A., Lenz, D., Littlefair, S. P., Ma, Z., Macleod, D. M., Mastropietro, M., McCully, C., Montagnac, S., Morris, B. M., Mueller, M., Mumford, S. J., Muna, D., Murphy, N. A., Nelson, S., Nguyen, G. H., Ninan, J. P., Nöthe, M., Ogaz, S., Oh, S., Parejko, J. K., Parley, N., Pascual, S., Patil, R., Patil, A. A., Plunkett, A. L., Prochaska, J. X., Rastogi, T., Reddy Janga, V., Sabater, J., Sakurikar, P., Seifert, M., Sherbert, L. E., Sherwood-Taylor, H., Shih, A. Y., Sick, J., Silbiger, M. T., Singanamalla, S., Singer, L. P., Sladen, P. H., Sooley, K. A., Sornarajah, S., Streicher, O., Teuben, P., Thomas, S. W., Tremblay, G. R., Turner, J. E. H., Terrón, V., van Kerkwijk, M. H., de la Vega, A., Watkins, L. L., Weaver, B. A., Whitmore, J. B., Woillez, J., and Zabalza, V. (2018). The Astropy Project: Building an inclusive, open-science project and status of the v2.0 core package. *ArXiv e-prints*.

[Trenti et al., 2011] Trenti, M., Bradley, L. D., Stiavelli, M., Oesch, P., Treu, T., Bouwens, R. J., Shull, J. M., MacKenty, J. W., Carollo, C. M., and Illingworth, G. D. (2011). The Brightest of Reionizing Galaxies Survey: Design and Preliminary Results. , 727:L39.

[van der Wel et al., 2014] van der Wel, A., Franx, M., van Dokkum, P. G., Skelton, R. E., Momcheva, I. G., Whitaker, K. E., Brammer, G. B., Bell, E. F., Rix, H.-W., Wuyts, S., Ferguson, H. C., Holden, B. P., Barro, G., Koekemoer, A. M., Chang, Y.-Y., McGrath, E. J., Häussler, B., Dekel, A., Behroozi, P., Fumagalli, M., Leja, J., Lundgren, B. F., Maseda, M. V., Nelson, E. J., Wake, D. A., Patel, S. G., Labbé, I., Faber, S. M., Grogin, N. A., and Kocevski, D. D. (2014). 3D-HST+CANDELS: The Evolution of the Galaxy Size-Mass Distribution since z = 3. , 788:28.

[van Vledder et al., 2016] van Vledder, I., van der Vlugt, D., Holwerda, B. W., Kenworthy, M. A., Bouwens, R. J., and Trenti, M. (2016). The Size and Shape of the Milky Way Disk and Halo from M-type Brown Dwarfs in the BoRG Survey. .

[Williams et al., 2018] Williams, C. C., Curtis-Lake, E., Hainline, K. N., Chevallard, J., Robertson, B. E., Charlot, S., Endsley, R., Stark, D. P., Willmer, C. N. A., Alberts, S., Amorin, R., Arribas, S., Baum, S., Bunker, A., Carniani, S., Crandall, S., Egami, E., Eisenstein, D. J., Ferruit, P., Husemann, B., Maseda, M. V., Maiolino, R., Rawle, T. D., Rieke, M., Smit, R., Tacchella, S., and Willott, C. J. (2018). The JWST Extragalactic Mock Catalog: Modeling Galaxy Populations from the UV through the Near-IR over 13 Billion Years of Cosmic History. *The Astrophysical Journal Supplement Series*, 236:33.

[Zheng et al., 2012] Zheng, W., Postman, M., Zitrin, A., Moustakas, J., Shu, X., Jouvel, S., Høst, O., Molino, A., Bradley, L., Coe, D., Moustakas, L. A., Carrasco, M., Ford, H., Benítez, N., Lauer, T. R., Seitz, S., Bouwens, R., Koekemoer, A., Medezinski, E., Bartelmann, M., Broadhurst, T., Donahue,

M., Grillo, C., Infante, L., Jha, S. W., Kelson, D. D., Lahav, O., Lemze, D., Melchior, P., Meneghetti, M., Merten, J., Nonino, M., Ogaz, S., Rosati, P., Umetsu, K., and van der Wel, A. (2012). A magnified young galaxy from about 500 million years after the Big Bang. , 489:406–408.

[Zitrin et al., 2015] Zitrin, A., Labbé, I., Belli, S., Bouwens, R., Ellis, R. S., Roberts-Borsani, G., Stark, D. P., Oesch, P. A., and Smit, R. (2015). Lymanα Emission from a Luminous z = 8.68 Galaxy: Implications for Galaxies as Tracers of Cosmic Reionization. , 810:L12.

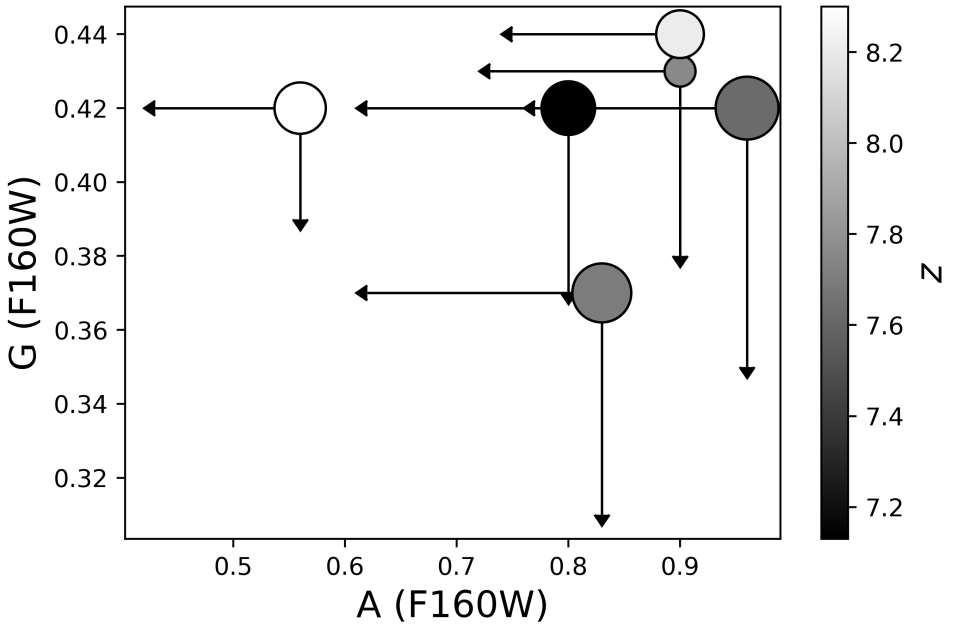

Figure 15 The size of the points correlate with IRAC color. It is a qualitative display of larger points being more "blue" in their composition. This is only of The "Super-8" from Bridge, et al. in prep.

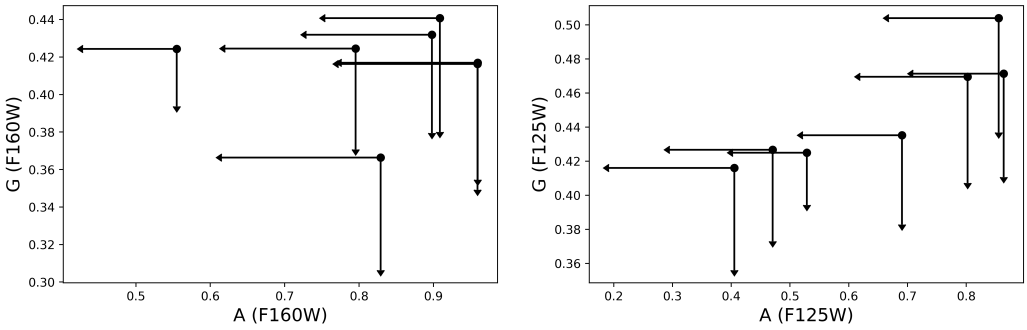

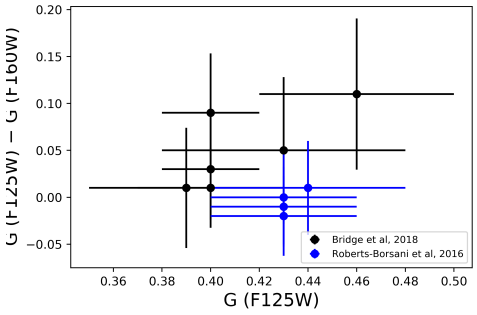
G (F125W) − G (F160W)
G (F125W)
Bridge et al, 2018
Roberts-Borsani et al, 2016

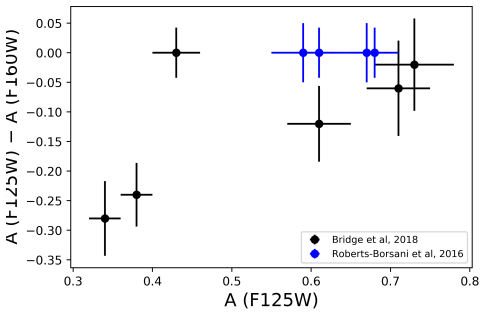
A (F125W) − A (F160W)
A (F125W)
Bridge et al, 2018
Roberts-Borsani et al, 2016

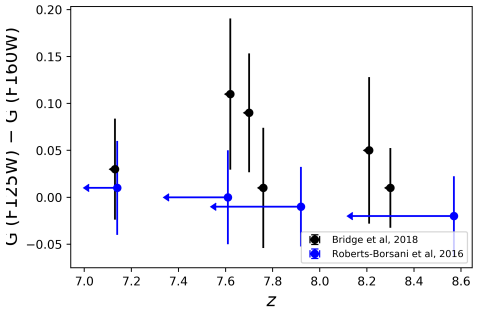
G (F125W) − G (F160W)
z
Bridge et al, 2018
Roberts-Borsani et al, 2016

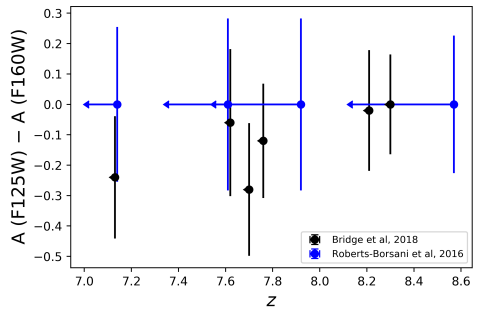
A (F125W) − A (F160W)
z
Bridge et al, 2018
Roberts-Borsani et al, 2016

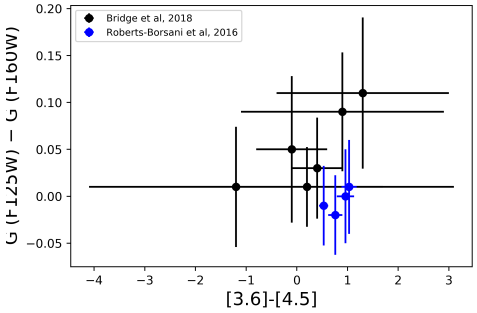
G (F125W) − G (F160W)
[3.6]-[4.5]
Bridge et al, 2018
Roberts-Borsani et al, 2016

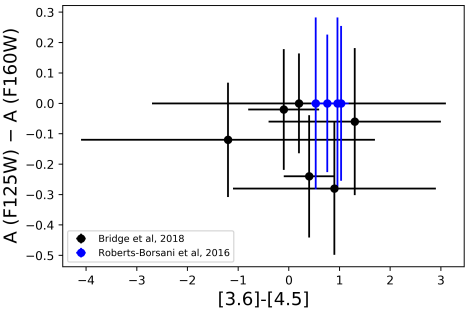
A (F125W) − A (F160W)
[3.6]-[4.5]
Bridge et al, 2018
Roberts-Borsani et al, 2016